Water-in-oil microemulsions as soft-templates to mediate nanoparticle interfacial assembly into hybrid nanostructures

---

Doctoral Thesis
in fulfilment of the requirements for the academic degree
“doctor rerum naturalium”
(Dr. rer. nat.)

in the scientific discipline
“Colloid Chemistry”

submitted to the
Faculty of Science of the University of Potsdam

Rebeca Fortes Martín
Born in Salamanca, Spain

Potsdam-Golm, December 2022

Supervisor/ Betreuer: Prof. Joachim Koetz*
Evaluators / Gutachter(inne)n: Prof. Michael Gradzielski§, Prof. Yan Lu*,
Prof. Ilko Bald*, Prof. Helmut Schlaad*
** Universität Potsdam, Institut für Chemie*
§ Technische Universität Berlin, Institut für Chemie

Published online on the
Publication Server of the University of Potsdam:
https://doi.org/10.25932/publishup-57180
https://nbn-resolving.org/urn:nbn:de:kobv:517-opus4-571801

Abstract

Hybrid nanomaterials offer the combination of individual properties of different types of nanoparticles. Some strategies for the development of new nanostructures in larger scale rely on the self-assembly of nanoparticles as a bottom-up approach. The use of templates provides ordered assemblies in defined patterns. In a typical soft-template, nanoparticles and other surface-active agents are incorporated into non-miscible liquids. The resulting self-organized dispersions will mediate nanoparticle interactions to control the subsequent self-assembly. Especially interactions between nanoparticles of very different dispersibility and functionality can be directed at a liquid-liquid interface.

In this project, water-in-oil microemulsions were formulated from quasi-ternary mixtures with Aerosol-OT as surfactant. Oleyl-capped superparamagnetic iron oxide and/or silver nanoparticles were incorporated in the continuous organic phase, while polyethyleneimine-stabilized gold nanoparticles were confined in the dispersed water droplets. Each type of nanoparticle can modulate the surfactant film and the inter-droplet interactions in diverse ways, and their combination causes synergistic effects. Interfacial assemblies of nanoparticles resulted after phase-separation. On one hand, from a biphasic Winsor type II system at low surfactant concentration, drop-casting of the upper phase afforded thin films of ordered nanoparticles in filament-like networks. Detailed characterization proved that this templated assembly over a surface is based on the controlled clustering of nanoparticles and the elongation of the microemulsion droplets. This process offers versatility to use different nanoparticle compositions by keeping the surface functionalization, in different solvents and over different surfaces. On the other hand, a magnetic heterocoagulate was formed at higher surfactant concentration, whose phase-transfer from oleic acid to water was possible with another auxiliary surfactant in ethanol-water mixture. When the original components were initially mixed under heating, defined oil-in-water, magnetic-responsive nanostructures were obtained, consisting on water-dispersible nanoparticle domains embedded by a matrix-shell of oil-dispersible nanoparticles.

Herein, two different approaches were demonstrated to form diverse hybrid nanostructures from reverse microemulsions as self-organized dispersions of the same components. This shows that microemulsions are versatile soft-templates not only for the synthesis of nanoparticles, but also for their self-assembly, which suggest new approaches towards the production of new sophisticated nanomaterials in larger scale.

/ Zusammenfassung

Hybride Nanomaterialen ermöglichen die Kombination von individuellen Eigenschaften jeder Art von Nanopartikeln. Einige Strategien für die Herstellung neuer großskaliger Nanostrukturen beruhen auf der Selbstassemblierung von Nanopartikeln über einen Bottom-up-Ansatz. Die Nutzung von Templatstrukturen ermöglicht Anordnungen in definierten Mustern. In einem typischen Soft-Templat werden Nanopartikel und andere oberflächenaktive Wirkstoffe in nicht-mischbare Flüssigkeiten eingebracht. Die resultierenden selbst-organisierten Dispersionen beeinflussen die Nanopartikel Interaktionen und kontrollieren die nachfolgende Selbstassemblierung. Insbesondere Interaktionen zwischen Nanopartikeln mit sehr unterschiedlicher Dispergierbarkeit und Funktionalität können Interaktionen an einer Flüssig-Flüssig Grenzfläche gerichtet werden.

In diesem Forschungsprojekt wurden Wasser-in-Öl Mikroemulsionen aus quasi-ternären Mischungen mit Aerosol-OT als Tensid hergestellt. Oleyl-beschichtete superparamagnetische Eisenoxid und/oder Silber Nanopartikel wurden in der kontinuierlichen Ölphase eingebracht, während die Polyethyleneimin-stabilisierten Gold Nanopartikel in feinverteilte Wassertröpfchen inkorporiert wurden. Jede Sorte von Nanopartikeln kann den Tensidfilm und die Tröpfchen-Interaktionen auf verschiedene Weise beeinflussen, und seine Kombination führt dabei zu synergetischen Effekten. Die Anordnung von Nanopartikeln an der Grenzfläche basiert auf der Phasentrennung. Auf der einen Seite, bildeten sich aus einem zweiphasigen Winsor II System mit niedrigen Tensid Konzentrationen durch Evaporation der oberen Phase dünne Schichten aus geordneten Nanopartikeln in Form von Filament-Netzen aus. Eine detaillierte Charakterisierung zeigte, dass die Filament-artige Strukturierung auf ein kontrolliertes Nanopartikeln-Clustering und auf die Ausdehnung der Mikroemulsions-Tröpfchen zurückzuführen ist. Dieser Prozess eröffnet flexible Einsatzmöglichkeiten für unterschiedliche Nanopartikel Kompositionen, indem die Oberflächenfunktionalisierung in unterschiedlichen Lösungsmitteln erhalten bleibt, und auch für verschiedenen Lösungsmitteln und über verschiedene Flächen. Auf der anderen Seite wurde ein magnetisches Heterokoagulat in höheren Tensid Konzentration hergestellt, dessen Phasentransfer von Ölsäure in Wasser mit einem anderen zusätzlichen Tensid in einer Ethanol-Wasser Mischung ermöglicht wurde. In Abhängigkeit von der Ausgangstemperatur der initialen Komponenten konnten definierte magnetisch-stimulierbare Öl-in-Wasser Nanostrukturen erhaltet werden. Dabei gelang es Wasser-dispergierbare Nanopartikelkompartimente in eine Matrix-Hülle aus Öl-dispergierbaren Nanopartikeln einzubetten. In dieser Arbeit wurden zwei verschiedene Wege aufgezeigt, um hybride Nanostrukturen aus inversen Mikroemulsionen selbst-organisiert herzustellen. Dies belegt, dass Mikroemulsions-Template nicht nur für die Nanopartikel Synthese geeignet sind, sondern auch für die Herstellung filamentartiger, selbstorganisierter Systeme. Es eröffnen sich hiermit neue Zugänge für die selbstorganisierte Strukturierung von Nanopartikeln auf der Mikrometerskala.

<<Caminante, son tus huellas
el camino y nada más;
Caminante, no hay camino,
se hace camino al andar.
Al andar se hace el camino,
y al volver la vista atrás
se ve la senda que nunca
se ha de volver a pisar.
Caminante, no hay camino
sino estelas en la mar.

(Antonio Machado) >>

(Walker, your footprints
are the only road, nothing else.
Walker, there is no road,
the road is made as you walk.
As you walk, the road is made,
and when you look back
you see the path
that you will never pass again.
Walker, there is no road;
only water wakes on the sea.)

/
(Wanderer, deine Spuren sind
der Weg und nichts sonst;
Wanderer, es gibt keinen Weg,
der Weg entsteht beim Gehen.
Beim Gehen entsteht der Weg
und beim zurückschauen
sieht man den Pfad, den man nie mehr
betreten wird.
Wanderer, es gibt keinen Weg,
nur Spuren auf dem Meer.)

Acknowledgements

Research is what comes out while one is busy planning other experiments, and so is in which research fields one ends involved and which outcomes are ultimately brought out.

I feel very grateful to Prof. J. Koetz for the opportunity to work in the group of Colloid Chemistry at the University of Potsdam. Especially for the possibility of making this research work with relative independence, the freedom for making some decisions, the supportive advice and the constructive discussions.
Thank you to Prof. H. Schlaad for the complementary supervision of the project, and to Prof. M. Gradzielski and Prof. Y. Lu for accepting the revision of this PhD Thesis. I also feel grateful to Prof. I. Bald for his support during the last months.
The collaborations regarding the characterization and interpretation of the nanoparticle assemblies are also gratefully acknowledged. I would like to thank Prof. A.F. Thünemann for the interpretation of the SAXS data, as well as Dr. J. Radnik and J.M. Stockmann for the XPS characterization. Many thanks to Dr. K. Tapio for the AFM characterization.

I am indebted to the Colloid Chemistry group of the University of Potsdam. I thank Dr. C. Prietzel for the HRTEM characterization and related discussions. The contribution of Sibylle Rüstig and Dr. B. Tiersch concerning characterization by Electron Microscopy must be recognized as well. A lot of gratitude includes the support of Daniela Höpfner with any kind of administration issue. I also thank to Dr. S. Kosmella, Björn Gamroth, Dr. R. R. Raju, Dr. F. Liebig and Ricky Hennig for their support and advice regarding conceptualization, characterization and many aspects of the lab work. There have been so many nice experiences, lab supervisions, lunch meals, coffee sessions and for sure fruitful discussions.

A particular mention must be for the institutional and non-institutional ways of access to the scientific literature sources.

I would like to give personal thanks to Basti, my parents and rest of family. Without their support, I certainly could have not reached that far.

And especially I would like to give an acknowledgement to all the people who along the way had offered their help and given me important lessons about research, science and life.

Index

1. Introduction to colloidal stabilization, microemulsions and nanoparticles

1.1 Stabilization of colloidal dispersions

Colloids involve materials in solid, liquid or gas phase with sizes in between the nanoscale and the microscale range. These components of very small dimensions can be dispersed in a continuous fluid phase or incorporated in solid or porous structures. Colloidal dispersions can include, for instance, nanoparticles and microparticles as solid entities, polymers and micelles as supramolecular and self-associated systems, and emulsions and microemulsions as liquid-in-liquid compartmentalized dispersions.

The interactions among themselves and with the surrounding medium will determine their stabilization, namely electrostatic, steric or electrosteric (**Figure 1.1**). [1,2] Destabilization phenomena involve changes in the mixture state after equilibration time, ultimately leading to heterogeneous systems. For instance, phase-separation can be caused by droplet coalescence, or fusion into larger droplet sizes, or by creaming as a combination of droplets onto an upper-phase. Aggregation can be caused by coagulation or flocculation, attributed to suppression of surface charges or to van der Waals attractive forces overcoming repulsive interactions. Ostwald ripening consists on an uncontrolled particle growth due to the molecular diffusion tendency of large particles to become larger and small particles to become smaller. Sedimentation occurs when larger aggregates deposit on the bottom of the liquid dispersion. [2,3]

For particle dispersions, the Derjaguin-Landau-Verwey-Overbeek (DLVO) theory considers stabilization as a balance between attractive and repulsive interactions. The repulsion energy, associated to Coulomb interactions between double-layers of surrounding ions, decreases exponentially upon inter-particle distance. The combination with the van der Waals attraction energy upon inter-particle distance creates a characteristic curve depending on the type of particle stabilization. These combined energy-distance curves determine the electrostatic stabilization, presenting two minima in the potential energy which are separated by an energy barrier (**Figure 1.1-a**). [1–4] The height of the energy barrier will determine whether the system is kinetically stable against coagulation. Thus, if the energy barrier is high enough, shorter inter-particle distances to reach the first minimum will be avoided, and the particle will be electrostatically stable with the potential energy in the second minimum. [1,2,4] The combination of electrostatic and steric repulsions against van der Waals attractions will constitute the electrosteric stabilization (**Figure 1.1-b**). [1,5]

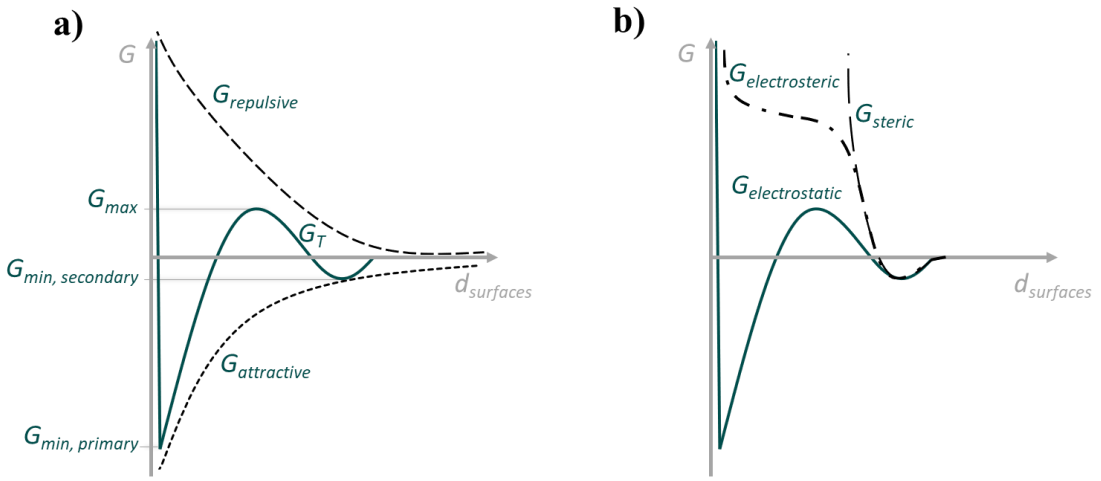

Figure 1.1. Potential energy upon inter-particle distance for colloidal stabilization: a) electrostatic stabilization as combination of van der Waals attraction and electrostatic repulsion; b) electrosteric stabilization as a combination of electrostatic and steric stabilizations. [1–3]

The control of interactions in liquid dispersions can lead to organized associates and controlled assemblies. Self-Assembly of colloidal structures can be interpreted as a controlled or restricted aggregation, in which the attractive interactions can be controlled or directed, sometimes reversibly.

1.2 Microemulsion properties and applications

Microemulsions can be defined either as thermodynamically-stable, self-organized liquid droplets under 100 nm size with appearance of optically clear, isotropic dispersions, or can be also considered as swollen micelles. [6–8] While emulsions and microemulsions are both liquid dispersions of two immiscible liquids, emulsions are not thermodynamically stable and have larger droplet sizes. Nanoemulsions are another type of liquid dispersions with droplet sizes below 500 nm and more polydisperse, which are kinetically stable but not thermodynamically stable. [8,9]

Surface-active agents and association in liquid dispersions

Classical emulsifiers are generally surface-active agents based on amphiphilic molecules, in addition to more complex macromolecular structures like polyelectrolytes, amphiphilic polymers or combinations of them.[2,10] Moreover, enhanced stabilization by particles adsorbed at the liquid-liquid interface produce Pickering emulsions and colloidosomes. [11–15] An amphiphilic molecule is composed of at least a hydrophilic head group and a hydrophobic tail, so that self-organized systems will be formed in a liquid dispersion according to the affinity or repulsion between the hydrophilic and hydrophobic domains. These compounds are also

considered surface-active agents or surfactants as they can reduce significantly the surface tension of a liquid interface by distributing in an organized, closed packed structure along the interface. When the number of surfactant molecules is above the critical micelle concentration, they tend to form micelles inside the liquid phase. The aggregation number is considered to be the average amount of surfactant monomers forming a micelle and can be calculated from the determination of the respective micellar weights. Therefore, surfactants at concentrations above the critical micelle concentration are commonly used to produce and stabilize microemulsion droplets of dispersed liquid phases, which are compartmentalized from another continuous phase by their micellar, packed structure. [16,17]

There are multiple types of surfactants whose internal structure will conditionate the formation of different types of micelles or microemulsions. According to their polar head group, surfactants and can be charged or uncharged. Charged surfactants can be classified as cationic like cetyltrimethylammonium bromide (CTAB) and benzyldimethylhexadecylammonium chloride (BDAC), anionic like sodium dodecyl sulphate (SDS), Aerosol-OT (AOT) and phospholipids, or amphoteric -zwitterionic- like sulfobetaines (SB). On the other hand, some representative non-ionic surfactants can be polysorbates like Tween 80, Brij 35, Span, Igepal, Pluronics, etc. Generally, non-ionic surfactants are considered less toxic, while cationic surfactants are reported to be more toxic than anionic surfactants. Regarding the non-polar part of a surfactant, the molecular structure can be single- or double-tailed. The hydrocarbon tails can be additionally linear or branched. Moreover, double-tails can form more complex structures like gemini and bola surfactants.[2,17,18] Combination of different surfactants and/or co-surfactant additives is especially relevant to enhance stability with non-ionic surfactants, in biocompatible microemulsions or in pharmaceutical formulations. [2,8,19] The critical packing parameter (*cpp*) of a given surfactant can be defined as the packing ratio of the hydrophobic volume (V_0) in relation to its head-group area (a_0) and tail length (l_c). [2,20] The value of this parameter will provide an estimation about the type of surfactant, based on the morphology of the resulting liquid dispersions, according to different numerical ranges (**Figure 1.2**). [2,16,17,20,21]

The hydrophilic-lipophilic balance (*HLB*) represents a set of numerical values assigned to a given surfactant or emulsifier to provide an insight about their hydrophilicity or lipophilicity. [2,22] This numerical system was initially made using different ethoxylate surfactants and ranges from 1 to 30, so that the higher the *HLB* value, the more the hydrophilic character. Thus, surfactants in the lower range (*HLB* <7) will have higher tendency to form reverse emulsions or microemulsions. For a mixture of surfactants or emulsifiers, the resulting *HLB* is determined according to their ratio. [2,22] Nevertheless, this term is not considering many important factors such as temperature, type of oil solvent, and salinity. Therefore, it would be more convenient to replace it by a more developed interpretation such as the hydrophilic-lipophilic deviation. [8,23,24]

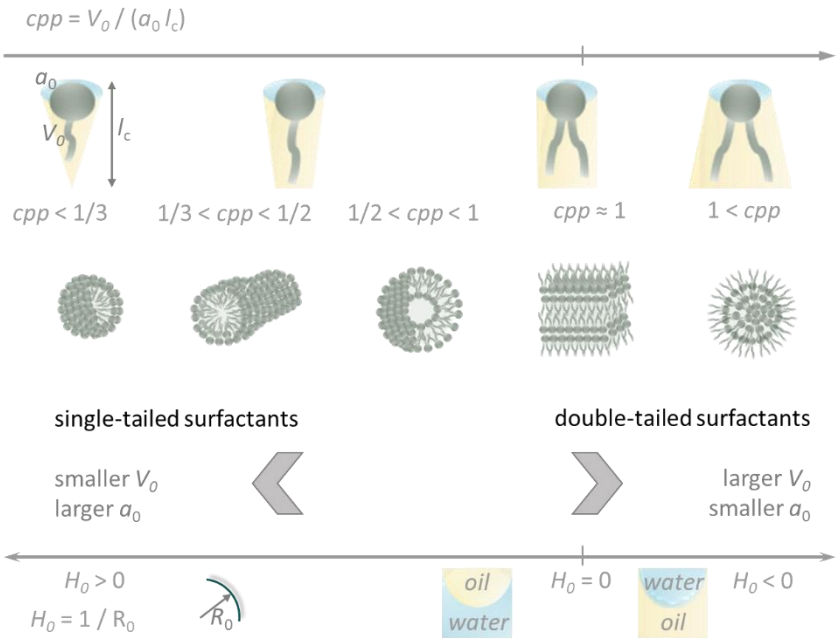

Figure 1.2. Classification of surfactants according to numerical parameters and the resulting morphology of their self-organized systems. [2,17,21]

Microemulsion parameters and phase properties

For the formulation of microemulsions, ternary mixtures with defined compositions of surfactant, oil and aqueous components are needed to form the adequate optically-clear dispersions. Oil-in-water (o/w) microemulsions will constitute an isotropic normal phase (L_1), being water in predominant presence as the continuous phase. On the other hand, reverse, water-in-oil (w/o) microemulsions would constitute an isotropic L_2 phase, being water as the dispersed phase. [2,21] Isotropic L_2 phases are more favoured by double-tailed surfactants (**Figure 1.2**). Sometimes, bicontinuous phases are formed, in which both the water or oil phase are predominant. [2,21,25] Ternary phase diagrams can offer an insight about the different phase regions for every composition point, given by mass ratio (*m.r.*) or by molar fractions (**Figure 1.3**). [26] For a reverse (w/o) microemulsion, the respective isotropic L_2 phase region is normally localized near to the oil and surfactant corners, while phase separation will be identified at low surfactant concentrations. Transitions to viscous regions or liquid crystalline phases are near to the surfactant corner. [8,17,21,27,28] In some cases, reverse microemulsions are swollen with other polar organic solvents rather than water, considered as non-aqueous reverse microemulsions. [8,19,24,29]

The water content of a given microemulsion mixture can be given generally in terms of the molar ratio of water in respect to surfactant, or as aqueous content in weight percentage (aq. wt.% = m_{aq} / (m_{oil} + $m_{surfactant}$ + m_{aq}) · 100) of the respective to the contents in the ternary mixture. Sometimes the content of the dispersed phase is also interpreted as a volume

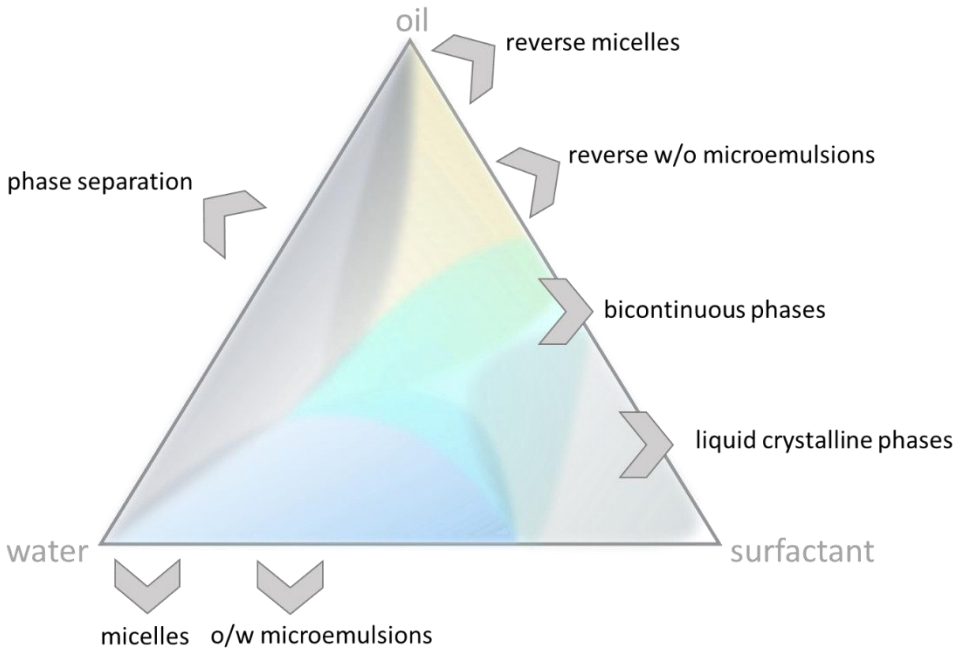

Figure 1.3. Representation of a ternary phase diagram, with approximate phase regions of different structural organization (considering a flexible surfactant film). The extension of the respective phase regions depends on the type of surfactant and solvent components, and on the presence of other additives in the liquid phases.

fraction of the droplets. [8,28] Addition of water to the microemulsion mixture generally causes swelling of microemulsion droplets and enhancement of the droplet interactions to induce structural changes till reaching the water solubilizing capacity, causing then phase separation.[17,24,27] Additionally, lower oil-to-surfactant mass ratio ($\omega = m_{oil} / m_{surfactant}$) will generally enhance the solubilization capacity and the viscosity by means of higher interactions and packing of droplets, which will lead to bicontinuous structures and liquid crystals upon water content. [27]

Variation of temperature on microemulsions can lead to stabilization or phase separation, whose limit is defined as upper or lower phase-transition temperatures for a given composition, sometimes referred as cloud points and haze points, respectively. A different parameter is the Krafft temperature, which states the capacity of a surfactant to dissolve in an aqueous phase and form micellar dispersions. The temperature-dependency of the solubilization capacity can be determined by binary phase diagrams of concentration and temperature. [2,21,28,30,31] While the lower phase-transition temperature is related to the curvature and rigidity of the surfactant film, the upper transition temperature is related to the droplet interactions. [17,28,30,32]

The spontaneous curvature of the surfactant film (H_0) can be defined as the inverse of the maximum droplet radius to incorporate a dispersed liquid phase under thermodynamically-stable conditions. [21,24,33] The interfacial curvature of microemulsions can determine both their morphology and swelling propensity. [8,17,21] Thus, a smaller size of the microemulsions at their maximum water solubilization capacity implies a more pronounced spontaneous

curvature, being the curvature a limiting factor of the water incorporation capacity of reverse microemulsions.[33,34] While the surfactant curvature in o/w microemulsions tends to be bended towards the water phase ($H_0 > 0$), reverse w/o microemulsions will have the curvature directed to the oil phase ($H_0 < 0$). When this curvature is supressed ($H_0 = 0$), the microemulsion phase will be bicontinuous, so that there is no distinction between continuous and dispersed liquid phases, usually visualized as a sponge-like structure. [8,17,21,24,25] Bicontinuous microemulsions can be sometimes, for certain surfactants, shown in ternary diagrams as a channel connecting the isotropic L_2 and L_1 phase regions. Generally, the tendency of the interfacial surfactant film to change its curvature is related to its flexibility or stability, and depends mainly on the type of surfactant, the temperature and the influence of other additives. [8,17,21,24] Thus, both the critical packing parameter and H_0 provide an insight about the resulting shape and properties of the liquid dispersion (**Figure 1.2**).

The droplet-droplet interactions are also related to the flexibility of the surfactant film, which is conditioned by the surfactant packing and the repulsion between the surfactant head groups. [8,17] For reverse microemulsions, inter-droplet attractions and repulsions are conditioned by the dynamic equilibria of surfactant inter-exchange and the inter-digitation with the solvent molecules in the continuous oil phase. Collisions between water droplets of a reverse microemulsion usually lead to their temporary fusion, according to the flexibility of the surfactant film. Consequently, the interchange of their aqueous inner content creates a limited transport of electric charges, allowing certain electric conductivity along the isotropic phase. [35,36] The enhanced conductivity of w/o microemulsions through their droplet-droplet interactions is known as percolation, and can be generally induced by increasing temperature or water content. Thus, the percolation threshold represents the limit in which percolation appears as a sudden increase in the conductivity, either by a minimum required temperature or by a minimum content or water. These percolation thresholds, for a given surfactant concentration, can be modulated by the type of oil content and by the presence of additives. [19,27,35] Thus, a more flexible surfactant film will enhance percolation and a more rigid surfactant film will hinder it. [8,27,28] The flexibility of the surfactant film will also increase with the appearance of bulk water for swollen microemulsions, further facilitating percolation phenomena. [30]

A classification of different types of Winsor Phases should be considered to categorize the isotropic phases and the phase-separating mixtures. (**Figure 1.4**). For the case of reverse microemulsions, an isotropic L_2 mixture is considered as a Winsor type IV phase. This isotropic dispersion will undergo phase separation at water contents above its incorporation capacity. The excess of water will initially appear as a lower phase below the L_2 phase, known as Winsor type II. At higher water contents, a middle-phase appears between the upper and lower phase (Winsor type III), till becoming the upper phase above a lower L_1 phase (Winsor type I). [16,19,24,37,38]

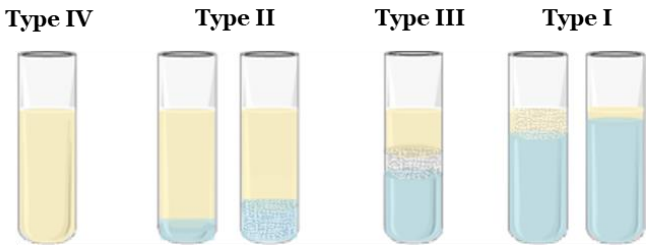

Figure 1.4. Classification of Winsor phases for reverse microemulsion systems.

Liquid crystals can be attributed to ordered assemblies of close-packed micellar structures, which behave as highly viscous fluids. The main liquid crystalline phases are classified according to their structural organizations: hexagonal for elongated micellar structures in hexagonal packing; cubic for regular packings of smaller associates of spherical, prolate or bicontinuous forms, and lamellar for planar alternating layers. [2,16] They can be generally favoured with double-tailed surfactants in higher concentrations, from dispersions of either one or of two solvents, and being isotropic or as separated mesophases. On one hand, in aqueous mixtures at increasing surfactant concentration, structural transitions can range from micellar dispersion to concentrated cubic, hexagonal, lamellar, and reverse hexagonal organizations. [8,21,37,39–41] On the other hand, the formation of liquid crystalline phases from the swelling of L_2 phases with water will occur as structural rearrangements of increasing ordering, which can contain continuous and dispersed liquid phases. [21,42]

Modulation of AOT reverse microemulsions

Aerosol-OT (AOT), referred to bis(2-ethyl-1-hexyl) sulfosuccinate as sodium salt, is one of the most used surfactants to form reverse microemulsions. Although it does not require a co-surfactant to stabilize reverse microemulsions, the incorporation of other amphiphilic compounds can be used as reference to study their co-surfactant effects. Its hydrophobic moiety consists on a double tail which favours the surfactant curvature to bend towards the oil phase and facilitates the incorporation water in continuous oil-phase dispersions. [8,17,21,43] An enhanced incorporation of water is also attributed to the steric effect of the branched hydrophobic tails. [8,42,44] The solubility of AOT in water is quite low, tending to form liquid crystalline phases. [21,27,37,41,42,45,46]

The water incorporation capacity of reverse microemulsions can be limited either by the curvature effect for more rigid surfactant films, or by droplet-droplet interactions for more labile surfactant films. Noteworthy, the phase separation can be interpreted according to the aspect of the separated phases: when an aqueous turbid phase is separated from an optically clear phase, the curvature effect is the limiting factor of the water incorporation; when both resulting phases are optically clear, the attractive inter-droplet interactions are the limiting

factor of the water solubilization. [34] Furthermore, at phase-separated systems, increasing the excess of water, incorporated to the bottom phase, can also decrease the concentration of AOT in the upper w/o phase, [42] so that other phase transitions should occur in the phase-separated Winsor types I-III.

The swelling, interactions and phase transitions of microemulsions from w/o droplets to bicontinuous phases upon water content are related to the flexibility of the surfactant film, and can be influenced by the microemulsions components, by external conditions and by the influence of additives.

Effect of AOT concentration

The water solubilization capacity and the droplet-droplet interactions of reverse microemulsions will generally increase with higher AOT contents, till forming viscous dispersions. Near the maximum incorporation capacity of water and above a certain AOT concentration, formation of bicontinuous and liquid crystalline phases can also occur. [42,45,46]

Effect of temperature

The increase of temperature will generally increase the swelling capacity and the droplet-droplet interactions of reverse microemulsions. [30,43,47,48] An optimal temperature can also reduce the viscosity and the interfacial tension, to provide smaller and more labile microemulsions, or to favour the transition to bicontinuous and lyotropic phases. However, higher temperatures will increase polydispersity and coalescence till phase separation occurs at the upper phase-transition temperature. [28,31,32,37,42,45,47,49–51] The temperature range of phase-stabilization between the upper and lower transition boundaries becomes narrower at higher water content. [28,30,32,44,51,52] On the contrary, the water incorporation capacity is invariant upon temperature when the AOT contains divalent or bulky counter-ions. [49,50,52]

Effect of pressure

Increasing the pressure of AOT reverse microemulsions can reduce the temperature range for stabilization. On the contrary, an applied pressure is necessary to stabilize reverse microemulsions in oil solvents of shorter hydrocarbon chain length and for supercritical conditions, by providing enough solvation of the surfactant tails to control the droplet interactions. [28,32,53] In any case, an increase of pressure in microemulsions should not affect the droplet sizes, as the surfactant should be mostly at the water-oil interface. [53]

Composition of the continuous oil phase

The components of the oil phase have an influence on the phase properties of reverse microemulsions, based on the affinity between the hydrocarbon chains of the surfactant tails and the oil solvent. For the case of the 2-ethyl-hexyl chains of AOT, an optimal affinity should be for solvents of up to seven hydrocarbon units. Shorter, cyclic, branched and polar hydrocarbon chains will limit the water incorporation capacity by higher curvature of microemulsions, while longer hydrocarbon chains will limit the incorporation of water by excessive droplet-droplet interactions. [17,27,28,34,42,44,47,54] The swelling behaviour and the droplet interactions can be also affected by the interpenetration and polarity of the solvents in the continuous oil phase. [35,48,54,55]

Other possible solvents in the oil phase include middle-chain alcohols, amines and carboxylic acids, which can act as co-surfactants. For instance, hydroxyl derivatives of longer hydrocarbon chains would tend to be more located at the water-oil interface, thus increasing the interfacial area and contributing to decrease the droplet size. [8,31] By combining aliphatic solvents with alcohols of slightly shorter chain length, the water incorporation capacity will increase upon concentration of the alkanol, as free space is released and reduce the stress between the surfactant tails. [17,34] The inter-droplet attractions can be also controlled by hydroxyl and amine derivatives, by stabilization of the surfactant film. [54]

Type of AOT counter-ion

The sulfonate head group of AOT might contain other cations instead of Na^+, constituting other M^{+n}-$(AOT)_n$ species, and also ionic-liquid-based surfactants. The electrostatic interactions will affect the conformation and stability of the surfactant film, similarly to the charge-screening effect of salts. For instance, the water solubilization capacity is lowered for K^+, Mg^{2+}, and Al^{3+} as counter-ions, induced by a chelation effect or their hydration radius. Other transition metal ions like Co^{2+}, Ni^{2+} Cu^{2+} and Zn^{2+} and alkyl ammonium derivatives can induce droplet elongation to form cylindrical microemulsions, which is attributed to the reduction of the surfactant curvature either by charge-screening, reducing the head-groups repulsion, or by different flexibility. [18,44,49,50,52] The use of AOT with IL derivatives as counter-ion can facilitate the incorporation of ILs in reverse microemulsions, [56–58] if then the incorporation of water is rather restricted [59]. The temperature-based stability of AOT microemulsions with some divalent and ammonium-derivative counter-ions is negligible, which can be related to the temperature-independent poor solubility of these ions. [49,50,52]

Composition of the dispersed polar phase

The dispersed phase of reverse microemulsions can be composed of other non-aqueous polar solvents like dimethylformamide, dimethylacetamide, formamide, propylene glycol, ethylene

glycol, etc. Similar phase behaviour can be obtained as in water-in-oil microemulsions, if then the stability, morphology and droplet interactions can be affected, depending on the type of polar solvent. [8,29] On the other hand, the properties and stability of AOT microemulsions containing non-aqueous solvents will be less affected by the temperature or the presence of salts. [29,60] Ionic liquids are usually referred to salt compounds which are melted at room temperature and have higher stability. Some ionic liquids which can be incorporated in reverse microemulsions include alkyl imidazolium derivatives. Ionic liquids dispersed in AOT reverse microemulsions affect drastically their phase properties. [8,29,56–58]

Other components of the dispersed polar phase confined in reverse microemulsions include aqueous solutions with incorporated additives. Water-soluble or water-dispersible additives can range from charged species to polar molecules, and from short-chain, small molecules to macromolecules.

Alcohols of shorter hydrocarbon chain lengths should be more located in the dispersed water phase, increasing the droplet sizes. [31] The location of amines and amine-derivatives in the water pool should be favoured by shorter chain and by lower pK_a, so that more acidic compounds would behave more as electrolytes. [61] The incorporation of non-ionic surfactants can also improve the water incorporation capacity and hinder the droplet-droplet interactions, up to an optimal concentration and chain length. On the other hand, additives like ethylene glycol which are not restricted to the dispersed phase could improve the flexibility of the surfactant film, and thus enhanced the swelling capacity and the droplet-droplet interactions. [61]

The addition of electrolytes on AOT microemulsions hinders droplet interactions and the water incorporation capacity. [19,27,34,36,37,42,47,48,54,61] Higher concentration of ions will reduce the repulsions between surfactant head groups due to their charge-screening effect, increasing the curvature and rigidity of the surfactant film. This effect is higher for salt derivatives than for their acid or basic analogues. [27,61]

The incorporation of organic compounds of more complexity can affect the microemulsion properties and interactions in variable ways, depending on their molecular structure and functional groups. [19,27,30,36] Larger additives like macromolecules, polymers and protein complexes would affect the water volume and properties of AOT microemulsions, according to their distribution along the liquid phases: when the solute is located at the oil phase the water pool volume will not be affected; when they are engulfed without dissolving inside the water droplets the volume can be increased, and when they are adsorbed at the interface the resulting complex will contribute to reduce its volume. [1,17,51] Other additives can also contribute to the formation of cross-linked channels. Sometimes, the shape of microemulsions can be modified upon addition of polymers. [62]

Polyelectrolyte-surfactant complexes in microemulsions

When water-soluble polymers contain functional groups that can be dissociated in water, they are considered polyelectrolytes, providing a net charge from the dissociated ions. Polyelectrolytes are generally classified according to their charge as polycations, polyanions or polyampholytes, and their net charge can be pH-dependent. Their structure can be also linear or branched, and can involve amphiphilicity. Due to their relative high surface charge density, polyelectrolytes can condensate with substances of opposite charge, forming polyelectrolyte complexes. When polyelectrolytes interact with surfactants of opposite charge, the cooperative assembly into polyelectrolyte-surfactant complexes will be mediated mainly by electrostatic attractions of defined sites, while hydrophobic interactions just play a secondary role. The conformation and stabilization of these complexes with neutralized charge are provided by the polymer structure and conformation in a given liquid phase. Some resulting structures include the formation of self-organized dispersions, cross-linked gels and crystalline materials. [1]

The interactions of polyelectrolytes or surfactants with other components in a dispersion can be predicted by adequate Molecular Dynamics simulations (**Figure 1.5**), [63,64] in addition to their adsorption on surfaces. [65] The incorporation of polyelectrolytes in microemulsions will also influence their phase behaviour, water incorporation capacity, and droplet interactions, based on their interactions with the surfactant film. The distribution of the polyelectrolytes can be inside the water droplets or at the water-oil interface. Several factors can be involved, including the molar mass, the functional groups of the monomers and external factors such as pH and temperature, etc. [1,24,62,66–73]

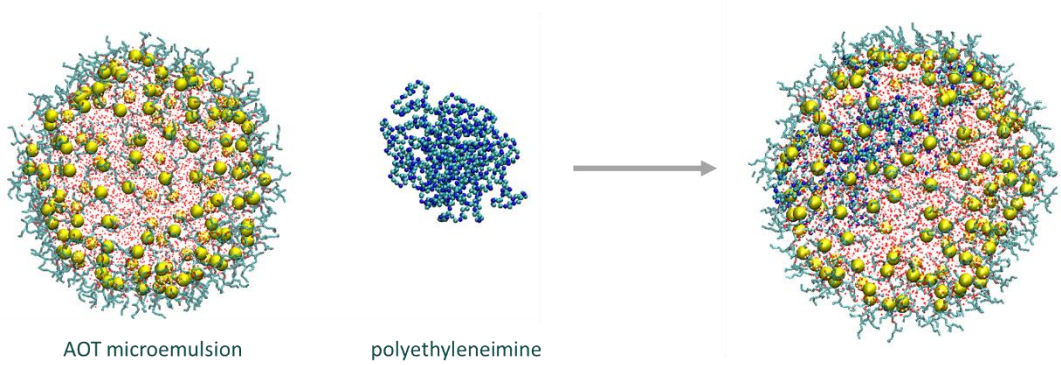

Figure 1.5. Snapshots of Molecular Dynamics Simulations from the combination of water-swollen AOT micelles with polyethyleneimine, at the beginning (left) and at the end (right) of the simulation run, provided by A. H. Poghosyan et al.

Polyelectrolytes can be used as reducing and stabilizing agents for nanoparticle synthesis, in water solution or in reverse microemulsions (see **Section 1.4**). Advantages of polyelectrolyte-modified microemulsions on nanoparticle synthesis include electrosteric stabilization and template effects on the shape and growth. For instance, the stabilization of the surfactant film contributes to a better control of the particle growth process. The electrosteric stabilization is

based on their adsorption at the nanoparticle surface and should prevent aggregation problems during their redispersion. [1]

Applications of reverse microemulsions

The dispersibility, compartmentalization and concentration of additives in an isotropic mixture of thermodynamically-stable microemulsions with low surface tension can offer numerous advantages as stabilizing and coating agents for the pharmaceutical, cosmetic, cleaning and coating technology industry. [2,8,19,21,24] AOT, due to its relatively low irritability and the possibility to stabilize mixtures without alcohols, has been used for the formulation of cosmetic and pharmaceutical products and aerosols. [24,27,37]

Biocompatible reverse microemulsions have been widely studied in the last decades for the delivery of drugs or bioactive substances. [8,24,74–79] With appropriate surfactants and solvents, microemulsions can be also applied in food-grade formulations. [8,19,77,80]

The use of reverse microemulsions as an optically clear liquid phase which can incorporate hydrophilic and hydrophobic compounds enables the study, and sometimes optimization, of chemical reactions. The recovery of the product or catalyst is an additional advantage. The mediation with micro-domains of large active surface can modulate the reactivity, according to the interactions with surfactant and solvents, the volume and polarity of the dispersed phase, ionic strength, viscosity, etc. [8,19,21,24,27,37] The use of catalytic reactions also includes enzymatic reactions. The enhancement of the catalytic activity by incorporation into microemulsions can be based on the amount and properties the confined water, namely pH, concentration, hydration degree, substrate mobility, etc. [19,21,27,28,37,75,79,81–83] The use of oxidoreductases in microemulsions can be further used for biosensing applications. Moreover, water-in-oil microemulsions can afford to study enzyme activities at lower temperatures for slower reactions without freezing the dispersed water, known as cryo-enzymology. [27]

Another possible use of microemulsions is for separation methods in cleaning and extraction processes, based on selective solidification or collection of one of the liquid phases. Similarly, applied pressure onto reverse microemulsions with short-chained hydrocarbon solvents as the continuous phase can selectively and reversibly solidify the aqueous phase, which contains some substance to separate. [28] Regarding liquid-liquid extraction, the partition of proteins between the L_2 phase and the water phase can be manipulated by tuning the pH or the ionic strength, or mediated with polymerization for immobilization. [8,19,27] Other interesting applications based on separation and dispersion processes include the removal of contaminants. [8,24,79,84] Reverse microemulsions can also stabilize water droplets in fuels to lower the heat released during combustion, and consequently reduce emission of NO_x and CO. [8,21]

Reverse microemulsions have been extensively investigated as micro-reactors for the templated synthesis of nanoparticles and polymer materials (see **Section 1.4**). The nanoparticles formed under confinement conditions can involve not only metallic or inorganic compositions, but also hybrid, polymeric and bioorganic nanostructures. [8,19,21,24,27,28,85,86] While formation of inorganic nanoparticles usually involves a confined reduction or co-precipitation, polymeric nanoparticles can be made by microemulsion polymerization, or by cross-linking, with the possibility of encapsulation of other substances. Their sizes and shapes will be also dependent on the microemulsion properties such as water swelling and droplet-droplet interactions. [27,86–88] Templated polymerization in microemulsions can also provide porous materials. Furthermore, by selective gelation of the microemulsion phase containing gelatine or phenolic derivatives, other dispersed substances can be entrapped in the inter-connected structure. For instance, active organo-gels of enzymes with remaining catalytic properties can be prepared. [27,37]

1.3 Nanoparticle properties, synthesis and applications

When the reduction in size of a particle is approaching atomic dimensions, quantization effects will take place and the high surface to volume ratio will alter the physical properties. Thus, the properties of a nanomaterial will differ from those of the bulk material. For instance, the quasi-continuous collective energy bands or structural domains will transform to discrete energy levels or lattices, involving changes in opto-electronic and magnetic properties. The melting temperature can also decrease. A higher active surface, in which more atoms would be at the surface, is of interest for catalytic, biomedical and sensing applications.

Magnetic nanoparticles

Magnetism is a physical property attributed to attractive and repulsive forces among magnetic dipoles of spinning charged, subatomic particles. Every substance contains magnetic dipoles under the influence of a magnetic field, if then not all exhibit the same behaviour in presence or absence of external magnetic forces. Thus, the composition of magnetic materials should consist of magnetic dipoles which respond to an applied magnetic field. While substances with diamagnetism and paramagnetism consist of domains which do not show a uniform magnetic response in absence of an external magnetic field, permanent magnets (ferromagnetism, ferrimagnetism, antiferromagnetism) concern domains of variable magnetic moments which can create by themselves a magnetic field. [89,90]

The magnetic properties for a given compound can be characterized by magnetization curves upon the force of an external magnetic field in both directions (**Figure 1.6**). Generally, the applied magnetic force in a given direction can increase and/or reduce the magnetization of a magnetic material. Magnetization increment is possible till the saturation magnetization (M_s), in which all their magnetic moments of the material are aligned at a certain saturation field (H_s). Permanent magnets will show some remnant magnetization (M_r) at a neutral external force. Coercivity is the magnitude of applied magnetic field (H_c) required for zero magnetization from the state of magnetic saturation at M_s. Thus, the overall magnetization behaviour of a permanent magnet at different external fields is known as the hysteresis loop. Hard magnetic materials have broad hysteresis loops of high coercive force (H_c) while soft magnetic materials have narrow hysteresis loops and low H_c (**Figure 1.6-a**). Above the Curie temperature, ferromagnetic materials (with permanent magnetism) will become paramagnetic (non-permanent magnets) due to collapsed magnetic domains. For these cases, the magnetization of the material will be proportional to the applied field according to their magnetic susceptibility. Decreasing the size of a permanent magnet will also reduce the number of magnetic domains but will increase the coercivity. Consequently, superparamagnetism is a variant of small, non-permanent magnets consisting on a single magnetic domain where the magnetic saturation can be reached due to its enhanced susceptibility at a certain field H_s. (**Figure 1.6-b,c**). [89–92] The classification of magnetic materials is also based on structural differences relative to their magnetic domains: for instance, according to parallel or antiparallel (oppositely-oriented) inner sub-lattices of magnetic momenta, to equivalent or non-equivalent sub-lattice magnetizations, and to the presence of magnetic anisotropy in the crystalline structure. [89,90,93]

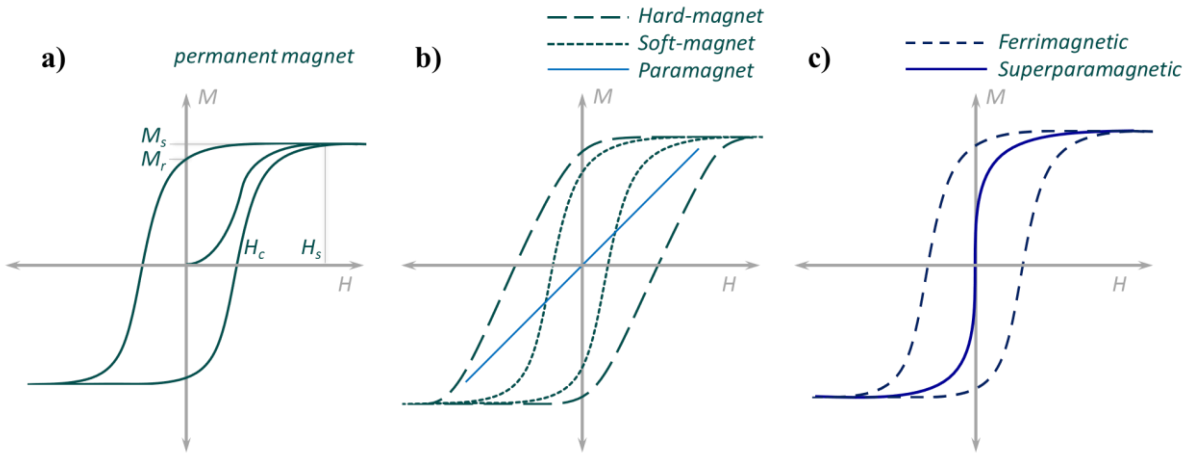

Figure 1.6. magnetization curves: a) permanent magnets assuming normalized saturation magnetization, b) non-permanent magnets, c) transition from ferrimagnetism to superparamagnetism by reduction of the magnetic domains by smaller sizes. [89–91]

Superparamagnetism can be developed from permanent magnets by decreasing their particle size (**Figure 1.7**). In a typical permanent magnet, multiple magnetic domains exist, so that M_r is present without applying a magnetic field. If the size is reduced, there will be less domains till containing only a single magnetic domain in which all moments are aligned showing maximum coercivity. Further below this critical size (d_c), in the nm range, the coercivity and the spontaneous magnetization will also collapse at a minimum size (d_0) for holding a magnetic domain, as the magnitude of the corresponding domain will be also suppressed. Nevertheless, the temperature barrier for spin reorientation would be low enough so that magnetization upon an external field would be possible. Consequently, below d_0 the particle would become superparamagnetic, with no coercivity but with possible magnetization reversal up to high saturation. [89,93,94]

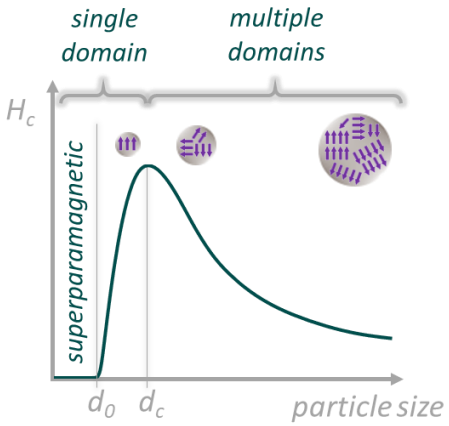

Figure 1.7. Dependence of magnetic coercivity upon the size of the magnetic particle. [89,93,94]

Magnetite is one of the most abundant magnetic materials, composed by iron oxide of mixed oxidations states. Reduction of its particle size will result in a transition from a ferrimagnet, with antiparallel and unequal sub-lattices in every domain, to superparamagnetic iron oxide nanoparticles (SPIONs) (**Figure 1.6-c**). However, the oxidation to maghemite is enhanced in reduced sizes, as more there would be more active surface on the smaller particles, which can explain the presence of a passivation layer. Concentrated colloidal suspensions containing magnetite nanoparticles in are considered ferrofluids, which change their morphological fluid state along an external magnetic field. [94–96]

Magnetite nanoparticles are commonly synthetized either by co-precipitation or by thermal decomposition of iron precursor salts. [91,93–97] Surface functionalization can be performed during the synthesis or as post-modification, to provide stabilization in organic or aqueous media, biocompatibility or some additional functionality. Common ligands to functionalize iron oxide nanoparticles surfaces include carboxylates, amine-derivatives, silanes, diols, phosphonates, etc. Functionalizing compounds can also range from simple molecules to polymers and bioactive substances. [91,93–95,97–99] For instance, thermal reduction of Fe(III) salt

in presence of oleic acid and oleylamine as stabilizing ligands affords oil-dispersible SPIONs. [91,93,94,97]

The manipulation of coercivity and magnetization-switching of magnetic nanomaterials under external fields (magnetic susceptibility) has offered much utility in diverse applications. For instance, assembly or patterning of magnetic nanoparticles can contribute to the development of magnetic storage devices in electronics and for energy storage. [91,93,100] Ferrofluids can be used to push non-magnetic components out of the region under an external magnetic field by magnetostatic repulsion, and for mechano-electronic properties like cooling devices and in audio speakers. [94,96] Regarding magnetic separation, biomolecules, microorganisms or contaminants can be attached to magnetic nanoparticles and then transported according to the field direction, being of interest for immunoassays and wastewater treatment. [94,96] For biomedical applications, several properties of the magnetic nanoparticles must be considered for their optimal biodistribution and targeting strategy, namely size distribution below 100 nm, shape and surface stabilization. [92,95] Thus, other attached components can also include bioactive substances to be magnetically-guided, for targeted drug delivery to specific tissues. [92,94–96] Superparamagnetic nanoparticles have been also used as contrast agents in Magnetic Resonance Imaging to enhance the dark and/or bright image signals of the relaxation processes, [91,93,94,96] which can be complementary for multimodal imaging [93] and for drug delivery monitoring [95]. Moreover, by Magnetic Fluid Hyperthermia, the friction created by magnetization reorientation by an alternating magnetic field will heat locally a targeted tissue, which is of interest for cancer therapy. [89,91,93,94]

Plasmonic nanoparticles

A plasmon can be interpreted as a cloud of conducting electrons with collective oscillation, caused by the interaction of an electromagnetic field at a metal surface. When the size of a noble metal particle is too small, the quantum-size effect involves spatial restrictions in the electron's movement as non-dimensional. As a result, the confined electrons of the conduction band will behave as a collective, non-propagating cloud referred as localized surface plasmon. [4,101,102] This differs from the surface plasmon polaritons which can propagate along a surface. The interaction with light or an electromagnetic field will create a polarized surface, induced by the splitting between the oscillating electronic cloud and the fixed cationic network, in similarity to induced dipoles. The compensation of this excitation will result in a resonance of a characteristic wavelength longer than the nanoparticle size (**Figure 1.8**). A significant interaction with light will occur when the frequency of the incident photons is close to the frequency of the coherent oscillation of the electron cloud. Thus, a localized surface plasmon resonance (LSPR) involves a coherent oscillation of the electron

cloud confined to the nanoparticle surface which absorbs light of resonant frequency. [4,101,103,104] For gold and silver nanoparticles, their characteristic plasmon bands enhance the absorption and scattering of light in the range of the UV-region, and also in the NIR for anisotropic shapes of larger dimensions, while no LSPR is observed for gold nanoclusters smaller than 2 nm. [102]

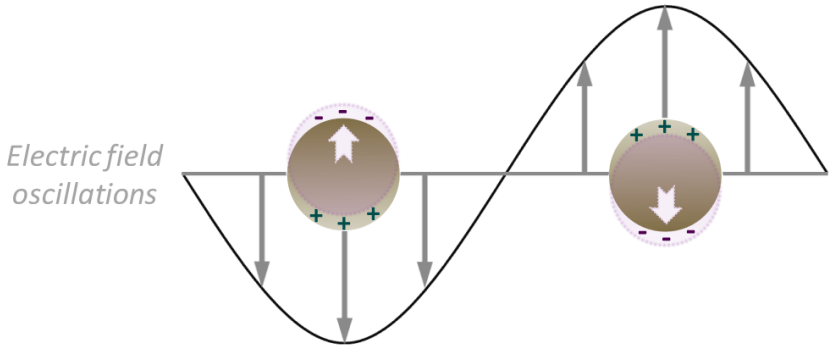

Figure 1.8. Schematic description of the oscillation of a localized surface plasmon in a metal nanoparticle upon the interaction of a magnetic field. [4,103,104]

The absorption of light related to the LSPR of a metal nanoparticle is affected by the dielectric properties and the charge distribution at the metal surface. Concretely, the position, form and intensity of the absorption signals upon wavelength depend on multiple factors: the dielectric constant of the medium, the electron density, the effective electron mass and the size and shape of the electron distribution. [101,105] Controlling these features enables the modulation of the optical properties of plasmonic nanoparticles. For instance, increase of the size of a noble metal nanoparticle will decrease the electron density, involving a red-shift of the wavelength corresponding to the maximum absorption. [4,101] The polarizability for nanoparticles larger than 25 nm causes additional broadening of the absorption peak, as the polarization becomes less homogeneous. On the contrary, for gold nanoparticles smaller than 25 nm, the absorption band becomes wider with smaller nanoparticle sizes. [102] Higher polarizability upon size can also involve higher absorption intensities, which is proportional to the inter-band transitions. [4] Larger metal nanoparticles of specific shapes also provide characteristic absorption, related to quadrupole and multipole resonances. [104] For anisotropic shapes, a longitudinal polarizability along the longest axis of the particle will differ from the transverse one, perpendicular to the long axis. Therefore, two different plasmon bands will be present: the transverse plasmon band will keep the characteristic absorption at about 520 nm while the longitudinal plasmon band will be red-shifted at increasing aspect ratio to values in the NIR region. [4,101,103] When the metal nanoparticles are sufficiently close from each other, shorter inter-particle distances will induce a red-shift and broadening in the absorption signal, attributed to coupling and hybridization effects. [4,101] The effects of the solvent and attached ligands on the LSPR absorption are related to the refractive index in the medium. A red-shift of the absorption maximum occurs proportionally to the refractive index

of the solvents. For the case of organic solvents containing polar and active functional groups which can interact with the metal surface, electronic charge-transfer effects and the chain length of the solvent molecules should be considered. [102,105] When the metal nanoparticles are capped with ligands, the electronic chemisorption of the attached functional group and the thickness of the ligand shell induce variable dampening of the absorption intensity and red-shifts. [101,102,105] For hybrid nanoparticles, nanoalloys and heterostructured nanoparticle assemblies of different compositions, hybridization of the plasmon bands should be considered. [4,101]

Metal nanoparticles are usually synthesized by the reduction of their respective ion precursors. For the synthesis of gold nanoparticles in water, the most acknowledged method is the reduction of the gold salt by sodium citrate under heating. Other methods, which can afford lower reaction temperatures and tuning of particle sizes and shapes, involve diverse reducing and stabilizing agents, namely sodium borohydride, phase-transferring surfactants, thiol- or amino- derivatives and polymers, among other functionalities. [5,102,103,106] To synthesize silver nanoparticles, common reducing and capping agents are sodium borohydride, *N,N*-dimethylformamide, peptide conjugates and polymers. Capping agents in silver nanoparticles are similar to those of gold nanoparticles, with the possibility of stabilization in nonpolar dispersions. [103]

Regarding application prospects of plasmonic nanoparticles, the optical properties in addition to the surface functionalization will conditionate their use in biomedical and sensing procedures. Biosensing is based on the detection of analyte molecules by selective binding to the plasmonic nanoparticle, which will cause a change in the optical response. This optical signal to detect can be colour change, light fluorescence, or light scattering, and is attributed to the LSPR absorption and/or to other labelling agents from surface functionalization. [4,5,101,102,106] In Surface-Enhanced Raman Scattering (SERS), the Raman signal of a molecular probe increases considerably when placed on the surface of a plasmonic particle absorbing light in the NIR region. [4,101,102,106] Additional advantages of noble metal nanoparticles include biomedical applications. For instance, gold nanoparticles afford good biocompatibility [5,106] while silver nanoparticles have also shown anti-bacterial properties [107]. By proper surface coating, these nanoparticles can present a good biodistribution, which is of interest for bioimaging and for targeted therapy. Visualization of plasmonic nanoparticles in biological samples is possible by various bioimaging techniques. Raman and dark-field microscopy are based on visualization of scattering signal assisted by the LSPR, while fluorescence and confocal microscopy may require additional labelling. Gold nanoparticles can be also used as contrast agents in photoacoustic imaging and for electron labelling in computed tomography, and also as radiosensitizers in radiotherapy. [106] For drug and gene delivery, surface functionalization is required not only to attach the bioactive compounds, but

for stabilization and efficient targeting. The release of the bioactive conjugates can be stimuli-responsive with specific functional groups and also light-mediated, assisted by the inherent optical properties. [5,106] By photodynamic therapy, nanoparticles absorbing in NIR radiation in combination with photosensitizers, once in a targeted tissue, would be heated upon laser irradiation, offering selective destruction of tumour cells. [5,106]

Stabilization and Self-Assembly of nanoparticles

Nanoparticles can be formed by top-down or from bottom-up approaches. Top-down methods involve the breaking-up of a bulk solid into smaller particles usually by physical forces, while bottom-up methods involve the building of particles from precursor substances, usually by a chemical reaction. [5,100,108] In a typical bottom-up approach in liquid medium, the nanoparticle precursors would react by reduction, co-precipitation, thermal decomposition, polymerization or cross-linking. The surface functionalization or stabilization of nanoparticles can be made with capping ligands and/or with other reducing agents, during the synthesis or as a post-modification. This functionalization would determine the dispersibility of the nanoparticles on a given liquid phase as well as the functionality, which includes biocompatibility, labelling, stimuli-responsiveness or use as building blocks for self-assembly. [91,95,97,98,108]

Formation of nanoparticles according to LaMer diagram

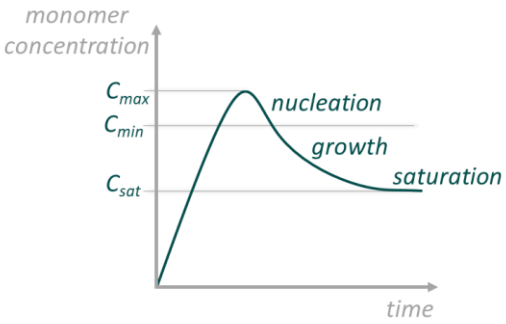

Figure 1.9. LaMer diagram as concentration of monomer precursor to form the nanoparticle upon time. [1,93,110]

During the synthesis of inorganic nanoparticles from ion precursors and other reagents in solution, the resulting products would initially form nuclei seeds which then would coalesce or include other product monomers to reach larger sizes. A correct balance between the nucleation and growth steps will afford uniform nanoparticles of defined size and shape. According to the LaMer mechanism (**Figure 1.9**), the nucleation must be raised above a critical concentration of nanoparticle "monomer" precursor (C_{min}), up to a maximum concentration of critical supersaturation (C_{max}) as a rate-limiting step. In a second stage, the concentration

of precursor decreases significantly till reaching again C_{min} and the saturation concentration (C_{sat}), so that nucleation cannot continue. In a final stage, there would be only growth of the resulting nuclei "clusters", based on the diffusion of the remaining precursor. [1,91,93,109,110] A temporal separation between nucleation and growth would permit the control of the nanoparticles size. For instance, if there is a fast nucleation process, most of the monomers will be consumed to form the nuclei and the growth will be minimized and slow, resulting in smaller and monodisperse particle sizes. On the contrary, when multiple nucleation processes occur at different times or when the growth is too prolonged, polydispersity and Ostwald ripening will take place. An efficient "burst" nucleation can be made by a rapid injection of the reagents, known as "hot injection", or by a rapid heating at the optimal temperature as "heating-up" method. [91,93,95,100] Additionally, the use of stabilizing agents on the nanoparticles surface should prevent uncontrolled growth. [1,109]

Microwave-assisted synthesis of nanoparticles

The use of microwaves constitutes a promising technology to afford chemical reactions with more efficiency and in an automated, sequential way. Microwaves consist on electromagnetic radiation with wavelengths in the range of cm to m. The chemical reactions to be enhanced with microwaves are based on dielectric heating (**Figure 1.10**). For this, the reaction solvents need to be polar or containing ions for absorbing the microwave irradiation. The incidence of microwaves creates an oscillating electric field. The dipoles will align though rotation and create molecular friction, while the ions or charged particles will oscillate though back-and-forth movement and cause collisions with neighboring components (**Figure 1.10-a**). As a result, a uniform, homogeneous heating will be generated from the electromagnetic energy of the microwave radiation. On the contrary, the reaction vessel should be of a material which has barely interaction with the microwaves, to allow a predominant transmission to the inner content. [108,111]

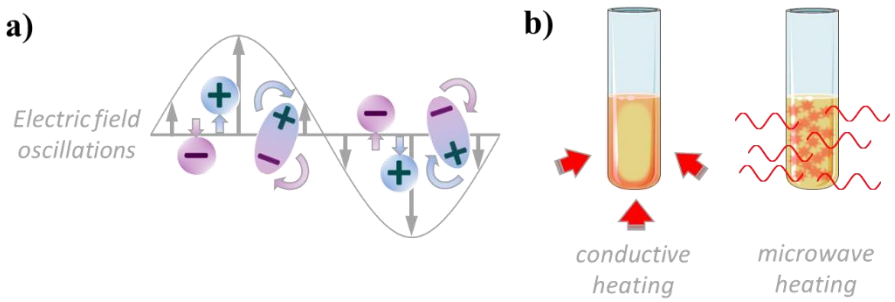

Figure 1.10. Scheme representation of the dielectric heating from microwave irradiation. [108]

Microwave irradiation offers multiple advantages when compared with the conventional heating in liquid baths or heating instruments (**Figure 1.10-b**). For instance, the resulting self-heating is selective to the reaction media with dielectric properties, leading to a direct, faster heating of the reaction mixture in a simultaneous, homogeneous way. Consequently, the chemical reactions can proceed faster -with shorter reaction times-, and more energy-efficient, leading in some cases to higher yields. Superheating can also occur if the reactions are made in sealed vessels, with temperatures above the boiling point of the solvents and with increased pressure, which would shorten even more the reaction times. [108,111]

Especially for the synthesis of nanoparticles, a fast heating of the precursors mixture by microwave irradiation will imply a more efficient nucleation to surge separately before a limited growth. [111,112] Therefore, advantages related to microwave-assisted synthesis of nanoparticles include higher monodispersity and better control of sizes and shapes. Nanoparticles synthesized with microwaves can be also dispersible in water or in nonpolar solvents using adequate solvents and capping agents. The nanoparticles to form with microwaves can be of an extensive variety of compositions, such as metallic, metal oxides, metal chalcogenide, metal fluoride, metal phosphate, core-shell hybrid nanoparticles, etc. Different morphologies and crystalline lattices of very good definition can be also achieved by the assistance of microwaves. [108,111,113,114] Microwave-assisted synthesis of nanoparticles represent also an alternative towards the use of more sustainable methods according to Green Chemistry principles, in terms of energy-efficiency, safety and the possibility of employing non-toxic reducing and stabilizing agents with the ion precursors. [112]

Control of interactions for the assembly of nanoparticles

The stability of nanoparticles in a dispersing medium relies on the overall balance between attractive and repulsive interactions (see **Section 1.1**). Restricting or manipulating these interactions between nanoparticles is relevant for their dispersibility and for their controlled assembly, preventing irregular agglomeration. Inter-particle interactions include electrostatic, magnetic, steric, hydrogen bonding and van der Waals forces, and can also involve dipolar or hydrophilic-hydrophobic configurations. [1,2,115–123] The properties conditioning these interactions can be inherent to the nanomaterial or provided by functional coating. [117,118,120,122,124] Consequently, the organization of nanoparticles in a controlled manner can be arranged by external physical fields, by designed surface functionalization with/without additives, and/or by the use of templates. [94,116–122,124–130]

Coating agents of nanoparticles can range from capping ligands to polymeric shells. [116–118,124] Conjugation strategies of functionalized nanoparticles can be with bio-molecules or bioactive substances, organic templates, labelling agents or stimuli-responsive compounds. [116–119,122–125] Nanoparticle surface functionalization can be provided during their synthesis or as post-

modification. Moreover, the functionalization can be specific to the nanoparticle composition. For instance, noble metals like gold or silver nanoparticles have a strong affinity for thiol derivatives, [5,99,131] while metal oxide nanoparticles can be functionalized with carboxylate, silane, phosphate or di-hydroxyl derivatives. [91,131,132]

The ordering of nanoparticles into larger assemblies provides colloidal supercrystals, superlattices or other nanostructured composites, considered similar to the organization of atoms or molecules into crystalline and supramolecular structures. [116,118–121,123,125,128] There are several ways to modulate the ordering and the inter-particle distances, such as the type of interactions, the ligands chain length, the number density of ligands on the particle surface, the presence of unbound ligands or surfactants, anisotropic shape or surface configurations, etc. [115,117,118,121,133] Sometimes, it is also possible to provide stimuli-responsiveness and reversibility on macroscopic scale. [116,118,122,134] Moreover, co-assembly of different types of nanoparticles can offer collective properties from each individual nanoparticle and enhancing effects. [119,120,125,127,128,130]

Assembled nanostructures over a surface include arrays of ordered nanoparticles in periodic distances, monolayers of packed nanoparticles, nanoparticle chains, thin films or other nanostructures of hierarchical patterns. [94,115,116,119–122,124,126–128,130,133,135,136] Some procedures for the self-assembly of nanoparticle films over a surface involve Langmuir-Blodgett techniques, dip-coating, drop-casting and spin-coating, with subsequent solvent evaporation. [94,127,130,133,135,137]

To form anisotropic or directional organizations, nanoparticles of non-spherical shapes, dipolar or amphiphilic properties, or templating effects must be used. [118,120–122,125–128,130,133] Templates can consist on either solid scaffolds, substrates with patterned surfaces or colloidal self-organized dispersions. [121,122,126] Concretely, soft-templates for self-assembly include block-copolymer structures, DNA origami scaffolds, biological systems or liquid-liquid dispersions. [116,118,120–122,125,127,130,133,134,138] The pre-defined nanoparticle arrangements by templates can be of variable scalability and dimensionality. [120,121,127,130,133,134,137]

The collective properties of nanoparticle assemblies can be relevant for sensing, optoelectronics, data-storage and energy-harvesting applications. [116,117,119,121,122,125–128,130,133,134]

Hybrid nanomaterials

The creation of novel nanostructures of hybrid compositions can offer new perspectives of applications, based on the combination of the individual properties of different nanomaterials. For instance, the superparamagnetic properties of iron oxide nanoparticles can be combined with the plasmonic properties of noble metal nanoparticles. [139–143] The type

of morphology and conjugation will affect the inherent properties of the individual components. [141,144,145]

Hybrid nanoparticles can be of diverse heterostructures: core-shell, core-satellite, yolk-shell, dumbbell heterodimers, linker-connected heterodimers, oligomeric or multimeric nanocomposites, etc. [93,125,139–146] Additionally, the conjugation of the different inorganic compounds can be by direct contact due to seed formation at the surface of a nanoparticle precursor, [139,141–147] or by surface pre-functionalization with coating agents, which can be linker ligands [93,125,141,144] or inter-layering compounds [139,143,146–148]. For instance, core-shell nanostructures sometimes require pre-coating or functionalization of the first component with a polymer shell or with multi-layer materials, to direct the insertion of the outer components. [139,143,147] On the other hand, heterodimers or multimers can be also formed by covalent binding, with ligands containing orthogonal functionalities specific for each metal. Complex structures can be also formed, from peptide-like bonds and complementary biomolecules pairing to enzyme-mediated linkages, polymerization or DNA-origami mediated assemblies. [125,144] Optical responses can be optimized with linkers to control the inter-particle distance. [141,144] Regarding one-pot synthesis of hybrid nanoparticles, several methods have been developed based on the sequential seed-mediated growth over another nanoparticle precursor, also assisted by microwaves, so that the shell or second particle should be formed at a different temperature than the core or first particle, or at different times, with an optimal molar ratio of the precursors. [111,140,141,145] Another approach to form hybrid nanostructures is by directed reduction or directed assembly at an oil-water interface. [149–152].

The applicability of hybrid nanoparticles relies usually in the combined properties, and sometimes also on synergistic, enhancement and stabilization effects. Additionally, multiple functionalization is possible by conjugation of different capping agents on each nanoparticle domain. The appearance or enhancement of spectroscopy signals, by the LSPR of noble metal nanoparticles or by labelling functionalization, is of interest for colorimetric visualization, labelling, SERS and chiroptical responses. This can be useful for detection of toxic substances and for immuno-sensing. [139,140,144,146] With hybrid nanomaterials as heterogeneous catalysts, the rate of a reaction improves with additional charge-transfer effects, different crystalline lattices, in addition to surface functionalization and stabilization. [145,146] Heterostructured magneto-plasmonic nanoparticles can also provide enhanced catalytic activity, due to the concentration of active electrons at the contact between both compounds, with the additional advantage of magnetic separation. [140,145] Multimodal imaging with hybrid nanoparticles will be based on the use of contrast agents for different imaging techniques, as well as the possibility of surface functionalization with other labelling agents. [93,139,140,142] Biomedical applications also include combination therapy and theragnostics. [139,140,142,145,146]

1.4 Liquid-in-liquid dispersions for nanoparticle synthesis and assembly

Soft-templates usually involve non-solid, labile components in a liquid dispersion. Some characteristic examples of soft-templates include conventional emulsions and organized systems of polymers and biomolecules. Microemulsions can provide additional advantages based on their smaller sizes, simplicity of the components and thermodynamic stability.

Templated synthesis of nanoparticle from reverse microemulsions

One of the most studied applications of microemulsions is as nanoreactors for templated synthesis of nanoparticles. These soft-templates allow controlled reactions between the ion precursors under restricted conditions, so that specific size and shapes may be modulated. Nanoparticles formed in reverse microemulsions can be organic, inorganic or of hybrid compositions. Inorganic nanoparticles include metal, metal oxide, metal halide, and semiconductor materials, and can be synthesized typically by reduction or by co-precipitation. Organic nanoparticles are usually composed from synthetic polymers or biopolymers, resulting from microemulsion polymerization or by cross-linking. In a typical microemulsion-templated synthesis, the formation of nanoparticles is made either by mixing equivalent microemulsions, each containing different reacting compounds, or by addition of some of the reactants to the microemulsion containing the other precursor components is also possible. Several factors like water content and type of components can affect the size and shape of the resulting nanoparticles. [21,24,27,85,86,139,153–155]

Nanoparticles can be also made from templates synthesis in polyelectrolyte-modified microemulsions. The combination of polyelectrolytes with surfactants can also modulate the properties and interactions of microemulsions, and the polyelectrolytes can act both as reducing and coating or stabilizing agent. [1] Some representative examples of microemulsion-templated synthesis in ternary mixtures containing polyelectrolytes have provided polyethyleneimine-coated gold nanoparticles [156,157] and cadmium sulphide quantum dots, [158] as well as poly(diallyldimethylammonium chloride)-coated magnetite, [159] zinc sulphide, [160] cadmium sulphide [158] and barium sulphate [161,162] nanoparticles. Additional examples include polyampholyte-coated gold [70] and barium sulphate [69] nanoparticles, anisotropic barium sulphate nanoparticles [161,162] and chitosan-combined hydroxylapatite nanofibers [160].

From self-organized systems to self-assemblies.

Colloidal dispersions can be used as soft-templates for the formation of nanoparticle assemblies. In this approach, self-organized systems would be initially formed from the incorporation of nanoparticles and other surface-active agents to a liquid dispersion. These

self-organized systems would mediate the nanoparticle interactions, acting as soft-templates for the subsequent self-assembly upon solvent evaporation. Other parameters such as temperature and additives can tune the morphology of the assembled nanostructures. [133,138] Analogously, directed assembly of nanoparticles at liquid-liquid interfaces can provide hierarchical arrangements. [120–122,127,129,134,136,138]

The self-organization of nanoparticles at a liquid-liquid interface can result in the formation of Pickering emulsions and colloidosomes, favoured by the reduction of interfacial energy. [13,15,122,129,134–136,138,163,164] These effects can be used for directed synthesis and assembly of nanoparticles. [135] For instance, heterodimeric nanoparticles can be formed by directed reduction of ion precursors at the surface of oil-dispersible nanoparticles, which were self-organized at the oil-water interface. [131] Moreover, colloidosomes can also act as a template for the assembly of nanoparticles under confined conditions, forming semi-hollow supra-crystalline nanostructures under specific conditions. [152] Gold-magnetite nanocomposites were also formed from nanoparticles of different solvent dispersibility, at the water-oil interface stabilized by Pluronics. [151] Other interfacial-based approaches consist on layer-by-layer assemblies or encapsulations, based on sequential coatings or interfacial layers. [129,134,135,165,166]

Bicontinuous microemulsions, with thermodynamic stability, have been used for the formation and/or assembly of versatile nanostructures defined by the inter-connected liquid-phase channels. [130,167] Bicontinuous emulsion-like gels, with interfacially-jammed liquid-phase domains, are referred as Bijels and constitute other type of soft-templates for the formation of planar assemblies. [122,134,138]

2. Characterization methods

Characterization of microemulsion phases

Ternary phase diagrams are helpful to differentiate dispersion phases at different ratios between the components in the mixture (**Figure 1.3**). Conductivity titrations provide information about droplet interactions and phase-transitions, based on the displacement of ions. For instance, percolation thresholds are recorded as a sudden increase in conductivity at a given water content, temperature or droplet volume fraction. Transition from w/o droplets to bicontinuous structures can be registered by a stabilization in the measured conductivity. Turbidimetry titrations can determine with better precision the water incorporation limits, and also the formation of other mesophases. Micro-Differential Scanning Calorimetry (micro-DSC) can distinguish different types of dispersed water at different water content, according to the crystallization and melting peaks. Visualization of microemulsion droplets, and morphological changes in the dispersion, can be provided by cryo-Scanning Electron Microscopy (cryo-SEM). The changes in the microemulsion properties can be also influenced by the composition of the liquid phases and the incorporation of additives.

Other characterization techniques of reverse microemulsions, which have been widely used, are mentioned as follows: diverse types of binary phase diagrams are useful to study the phase behaviour upon content of dispersed phase, temperature and pressure; viscosity behaviour can show phase transitions and inter-droplet interactions; Light Scattering has been used to study the swelling and diffusion of droplets; analytical ultracentrifugation can also determine the size distribution and the aggregation number; Polarizing Microscopy is useful to identify liquid crystalline phases; Spectrophotometry techniques can be applied on dynamics and kinetic studies; Nuclear Magnetic Resonance, Fourier transform Infrared spectroscopy, Small-Angle Scattering and X-Ray spectroscopy studies have been also used for structural characterization, and moreover, theoretical models and Molecular Dynamics simulations can predict or provide explanations about microemulsion interactions and phase properties. [8,21,24,27,28]

Characterization of nanoparticles

Dynamic Light Scattering (DLS) will provide an approximate estimation of the nanoparticle size based on the hydrodynamic diameter, calculated from the diffusion coefficient. Zeta potential can provide information about the electrostatic stabilization according to the electrophoretic mobility. Fourier transform Infrared spectroscopy (FTIR) can confirm surface functionalization by the presence of characteristic functional groups. Small Angle X-Ray Scattering (SAXS) can offer an interpretation about the structures and interactions of nanoparticles in a liquid phase.

Visualization of nanomaterials requires usually electronic microscopes, namely Scanning Electron Microscopy (SEM), Transmission Electron Microscopy (TEM) and Scanning-Transmission Electron Microscopy (STEM). Additionally, with Atomic Force Microscopy (AFM) other surface properties can be characterized according to the force measurements, topographic imaging or manipulation of forces. The composition and other surface properties of nanoparticles can be also measured with Energy Dispersive X-ray spectroscopy (EDX) and X-ray Photoelectron Spectroscopy (XPS).
Other techniques used to characterize nanoparticles of specific properties include: UV-Vis absorption related techniques for plasmonic nanoparticles magnetic hysteresis loops for magnetic nanoparticles.

Spectrophotometric characterization

The interaction of light with matter can result in several processes, namely absorption, transmittance, reflectance and scattering. These different types of interactions can be useful to study optical properties, approximate sizes, characteristic functional groups and stability.

UV-Vis-NIR Absorption and Transmittance Spectroscopy

Electromagnetic radiation in the ultraviolet (UV) region has characteristic wavelengths ranging from about 200 to 400 nm, for the visible (Vis) region goes from around 400 to 700 nm, and the near-infrared (NIR) region consider wavelengths in the range from 700 to 2500 nm. A light spectrophotometer can measure differences in the intensity of the incident light (I_0) and the recorded light after being forwarded through a sample (I_T). The comparison between the intensities at different wavelengths can be expressed in transmittance, usually in percentage (*T%*) (**Equation 2.1**), or absorbance (*A*) as the opposite of the logarithmic form (**Equation 2.2**):

$$T\% = \frac{I_T}{I_0} \cdot 100 \qquad \textbf{[Equation 2.1]}$$

$$A = log\frac{I_0}{I_T} = -log\frac{T\%}{100} \qquad \textbf{[Equation 2.2]}$$

The absorbance or transmittance profiles upon wavelength can detect and study the presence and properties of light-absorbing entities. Samples can range from liquid solutions or dispersions to transparent films and solids. For organic molecules containing special functional groups, the absorption will be based on excitation of their electrons. For nanoparticles composed of noble metals, their characteristic absorption bands at given wavelengths of maximum intensity are attributed to their LSPR properties (see **Section 1.3**).

Dynamic Light Scattering

Quasi-Elastic Light Scattering, also known as Photon Correlation Spectroscopy or Dynamic Light Scattering (DLS), can provide hydrodynamic size distributions of dispersed colloids. The colloidal particles or droplets to be measured by DLS should have Brownian motion, that is, random, temperature-dependent diffusion in the dispersing medium. The Stokes-Einstein equation (**Equation 2.3**) states the relationship between the hydrodynamic radius (r_h) and the translational diffusion coefficient (D). Other involved parameters are the Boltzmann constant (K_B), the temperature (T) and the viscosity of the dispersion (η).

$$r_h = \frac{K_B\, T}{6\pi\, \eta\, D} \qquad \textbf{[Equation 2.3]}$$

The diffusion coefficients can be calculated from the fluctuations on the intensity of the back-scattered light. A Fourier transform will provide the decay of the scattering intensity in correlation with time, known as intensity-time auto-correlation function. This involves a lower correlation or probability of finding a given particle at longer times, as it would have moved. The auto-correlation function should be transformed using the cumulants fitting method to extract the diffusion coefficients from the decay constants. [1,3,21,24]

Therefore, the conversion of the auto-correlation function can relate the intensity percentage with the size distributions. Larger particles scatter more than smaller particles, and the scattering intensity will have a lower decay with larger particle sizes as they would move slower (lower diffusion) and would lower the intensity fluctuations. Thus, the scattering profile for different size distributions will show signals of higher intensity percentage for the larger group, even though they might not predominate. For a more precise characterization of the smaller particles, the number and volume distribution should be calculated according to the respective scattering intensity upon size.

Fourier-Transform Infrared Spectroscopy

Infrared (IR) radiation comprises wavelengths in the range from µm to mm. Molecules can absorb this electromagnetic radiation at certain frequencies so that their chemical bonds can vibrate by stretching or bending. These specific absorptions to upper vibrational energy levels can be registered for a defined range of frequencies, usually in terms of wavenumber ($\bar{\upsilon}$), by Fourier Transform Infrared Spectroscopy (FTIR). Thus, the presence of characteristic functional groups of a compound can be found according to wavenumbers and widths of the absorption bands, in the wavelength range from 400 to 4000 cm^{-1}. Especially the FTIR spectra of a known compound can be used as fingerprint for its identification in other samples.

Turbidimetry

Turbid dispersions usually involve larger dispersed entities of certain instability, leading to phase-separation or sedimentation. Their appearance is not optically clear because the dispersed droplets or particles are too big to let the light be transmitted, so that scattering effects will predominate. Therefore, turbidimetry is an optical technique which can estimate the stability and organization of a liquid dispersion. Turbidity titrations can be made by the incorporation of additives or by changing the temperature of a dispersion, for a better characterization of phase-transitions. The measurement of a turbidimeter will be based on the intensity of the absorbed light, using a sensor to provide the percentage of turbidity. Moreover, this technique can be combined simultaneously with other measurements like conductometry and potentiometric titrations. [1,2]

Electrochemical characterization

The conductivity can be measured over a liquid dispersion, or over a surface. Generally, a defined voltage should be applied in order to measure fluctuations on the resulting electric current, registering the local voltage or the resistance.

Conductometry

Charge displacements in a liquid dispersion can be sensed with an electrode cell. The conductance is registered based on differences in the applied alternating voltage. For the case of reverse microemulsions, the charges include usually surfactant counter-ions and a minor contribution of dissociated surfactant. Conductivity measurements on microemulsions offer an insight about the diffusion of these ions in the dispersed phase, based on surfactant dissociation by micellar swelling and on temporary fusion or clustering of microemulsion droplets. Conductometry titrations can be recorded upon water content, temperature and surfactant concentration, providing information about initial swelling, droplet-droplet interactions and phase transitions. [8,21,27,30,35,36,68,72] In combination with other measurements like turbidity, complementary interpretation of phase transitions can be provided. [1,2] The influence of the composition of microemulsion and incorporated additives can be also compared. [19,27,35,40,48,68,72]

Zeta Potential measurements

The electrostatic stabilization of a colloidal particle or droplet is directly associated with the configuration of the electric double-layer of interfacial ions over its surface. The Zeta Potential is defined as the electro-kinetic potential difference between a dispersed colloid and the

dispersing medium, at the effective slipping plane of the ionic double-layer. The inner-layer of ions, known as Stern layer, is composed of counter-ions adsorbed between the surface and the Stern plane. The outer-shell of ions, known as diffuse layer, is composed of ions and counter-ions between the Stern plane and slipping plane. The distance between the colloid surface and the slipping plane, in which the net electric charge is equal to the net surface charge of the dispersed colloid, is known as Debye length. [1–3]

The Zeta potential (ζ) can be calculated from the electrophoretic mobility (μ_E) according to additional parameters (**Equation 2.4**), as it is influenced by the viscosity of the medium (η), the dielectric permittivity (ε) and the conditions of the Henry function ($f(\kappa,r)$).

$$\zeta = \mu_E \cdot \frac{3\,\eta}{2\varepsilon \cdot f(\kappa,r)} \qquad \textbf{[Equation 2.4]}$$

There are two approximations to interpret the Henry function. For Smoluchowski approach (**Equation 2.5**), a thin ion double-layer is considered, mostly used for dilute dispersions. On the contrary, for Hückel approach, a thick ion double-layer is considered. In the interpretation, ε_r is the dielectric permittivity of the medium and ε_0 is the permittivity of free-space. [1,2]

$$\zeta = \frac{\mu_E \cdot \eta}{\varepsilon_r \cdot \varepsilon_0} \qquad \textbf{[Equation 2.5]}$$

Additionally the electrophoretic mobility (μ_E) can be calculated from the electrophoretic drift velocity (v_E) using an electrophoretic cell. [1,3] By Electrophoretic light scattering, the drift velocity is extracted from the fluctuations in the back-scattering intensity induced by the diffusion of the particles, referenced as Doppler shift. [2,3] Generally, Zeta potentials in the range above +20 mV or below -20 mV indicate sufficiently charged particles, and therefore electrostatic stabilization by repulsion between the ion double-layers. The Zeta potential values can be also affected by properties of the dispersing medium, such as ionic strength, pH and composition of the liquid phase.

Resistivity

To characterize the conductivity properties of a film, a voltmeter can be used to measure the intensity current upon an applied voltage. The electrodes, connected to the voltmeter and to an electricity source, can be placed over contact points of a conductive material on modified glass slides, on modified indium tin oxide (ITO) slide, or on interdigitated modified electrodes. The conductivity value (κ) is the inverse of the resistivity (ρ) and provides an idea about whether a material or medium is conductive or not. The resistivity, measured in Ω/cm, is intrinsic of the material composition can be calculated from the electric resistance (R) at a fixed length (L) and cross-sectional area (A) of the conductive medium (**Equation 2.6**). For the

case of a surface of a certain area, the sheet resistivity ρ can be calculated using a four-point probe configuration. For this calculation (**Equation 2.7**), the inner-voltage (V_{int}) between two intermediate points and the current outer-intensity (I_{ext}) between two outer-point electrodes are measured along a fixed applied voltage (V_{ext}). The four points should be at the same distance along a line. [168]

$$\rho = R \cdot \frac{A}{L} = \frac{V}{I} \cdot \frac{A}{L} \qquad \text{[Equation 2.6]}$$

$$\rho = 2\pi A \cdot \frac{V_{int}}{I_{ext}} \qquad \text{[Equation 2.7]}$$

Thermo-analytical characterization

Differential Scanning Calorimetry

When a phase transition is induced on a material, heat will be emitted or adsorbed. For instance, solidification processes are normally exothermic -releasing heat- while melting is usually endothermic -absorbing heat-. With Differential Scanning Calorimetry (DSC), the presence of glass transitions, crystallizations or melting behaviour can be studied by comparing the differences in the heat flow during a temperature ramp.

A differential scanning calorimeter contains two vessel holders, one for the reference probe and the other one for the sample probe. The reference vessel can be empty or containing a reference compound. The vessels should be enclosed, only in contact with the heating and cooling systems, so that the heat will not be exchanged between themselves nor with the external environment. For measuring differences in the heat flow during heating or cooling, the temperature is changed simultaneously on both vessels at a fixed rate, and the difference of temperatures is registered from measured temperature-dependent resistance. The different behaviours of a material to be heated or cooled during a phase transition, in respect to the reference, are recorded upon time and temperature to provide the calorimetry curves with characteristic phase transitions. [169]

Crystallization peaks, below the melting temperature, can be distinguished in the cooling curves while melting peaks will appear in the heating curves. Moreover, micro-DSC can provide better sensitivity and accuracy, to detect smaller thermal effects or measure smaller samples. For reverse microemulsions, differences in the melting behaviour of the confined water can provide information about the properties at different water contents, to be distinguished as bound, interfacial or bulk water. [55,67,72,73,170]

Microscopy

Visualization of samples of very low sizes can be observed using appropriate microscopes by mediation of light, electrons or contact force. Size distributions can be also obtained by counting and statistical analysis of the entities. Generally, optical microscopes are used for lower magnifications, to provide images above the µm range. For nanoscale visualization, electron or scanning probe microscopes must be used.

According to the Rayleigh criterion for an optical microscope (**Equation 2.8**), the resolution limit to visualize a minimal distance, as the distance between a double-slit (δ), is given by the wavelength, the refractive index of the surrounding medium (n) and the diffraction angle (α).

$$\delta = \frac{0{,}61 \cdot \lambda}{n \ \sin\alpha} \qquad \textbf{[Equation 2.8]}$$

Based on the de Broglie wave-particle duality, light is composed of photons with an associated electromagnetic wave. However, the mass of a photon would not allow lower wavelengths for the visualization of smaller entities. Electrons are of larger mass, so that they can have associated lower wavelengths. Therefore, when light cannot provide a higher resolution, accelerated electrons can be used instead. Light microscopes use optical lenses while electron microscopes use electromagnetic lenses. [1,171,172]

On a different approach, topographic images can be also obtained based on the recording of surface interactions at strategic points of the sample, referred as Scanning Probe Microscopy.

Light microscopy

An optical microscope or light microscope uses a light source and a set of lenses to focus and visualize a sample under magnification in the mm to µm range. The samples to visualize are usually over a glass slide and should be thin or transparent enough so that the light beam can pass through from below through a condenser lens. Specific distances are needed between the focal point and the sample for providing a clear mirror image on the eyepieces or camera at different magnifications. Live movements or responsiveness can be also observed and recorded.

With the incorporation of crossed polarizing filters in the light microscope, polarized light microscopy can be performed for the characterization of crystalline or liquid crystalline structures. The second polarizing filter, referred as analyzer, has the polarization direction perpendicular to the first polarizer. Thus, the resulting configuration of crossed filters would supress the light unless there is another deviation from a birefringent or crystalline material in the sample. The interaction of the light with a crystal will depend on the orientation of the crystalline lattice, which is of interest for the visualization of liquid crystalline phases. For an anisotropic crystal, the light would get refracted out of phase in two polarized orientations

from two refractive indices, so that there is inherent birefringence. The visualization of the recombined rays provides characteristic patterns, depending of the orientation of the optical axis from the birefringent material to the analyser. [41]

Scanning Electron Microscopy

When accelerated electrons are interacting with a sample, the detection of secondary electrons and/or inelastic back-scattered electrons can provide topological information. This is used in Scanning Electron Microscopy (SEM) for a 3D-visualization. Secondary electrons are emitted from the inelastic scattering over valence-shell or conduction-band electrons, while inelastic back-scattered electrons result from the collisions of beam electrons with inner-shell atomic electrons. [173]

Cryo-SEM is a variant of SEM to visualize colloidal liquid dispersions without solvent evaporation. For this, a small volume of the sample should be previously cooled fast to cryogenic temperatures, so that the morphology of the original liquid phase is preserved. Cryo-SEM differs from cryo-EM (also referred as cryo-TEM), from which the electron beam is transmitted to provide visualization from biological samples, micellar structures, or entities in sub-nanometer resolution. [8,174]

Transmission Electron Microscopy

When accelerated electrons are transmitted through a sample, the projection of transmitted electrons can provide morphological information according to the contrast in electron density and atomic weight. This is used in Transmission Electron Microscopy (TEM) for a 2D-visualization, obtaining better spatial resolution than SEM. For organic moieties and compounds of lower electron density, the contrast created by scattered electrons might not be enough for their visualization and might require pre-treatment by deposition of contrast additives. [1,171,172]

With High Resolution Transmission Microscopy (HRTEM), it is possible to obtain a clearer view under higher magnifications, as well as the combination with other analytic methods. For instance, Scanning-Transmission Electron Microscopy (STEM) is another modality of TEM, in which the electron beam to be transmitted is focused on strategic points. Energy-Dispersive X-ray spectroscopy (EDX) can be also applied on each of the strategic points to provide information about the elemental composition. Other possible analytic techniques are Electron Energy Loss Spectroscopy (EELS), about chemical states, and Electron Diffraction for information about the crystalline lattice. [171,172]

Atomic Force Microscopy

The surface topography of a defined area in a sample can be analyzed according to the interaction force of a nanoscale tip in close contact with the sample, at defined points. This advanced version of Scanning Probe Microscopy, with resolution below the nm range, is known as Atomic Force Microscopy (AFM) or Scanning Force Microscopy. The scanning tip is attached to a cantilever, so that their bending for a certain interaction force is measured by the reflection of a laser light on this cantilever. The cantilever can also be moved by high-precision piezo-electric actuators, to measure across a scanning line or area which can be visualized using a light microscope. [175,176]

To determine the thickness of a film with soft-matter components, the measurement can be operating in the tapping mode, so that the topographic profiles are determined by differences in the vibrational motion of the cantilever, such as frequency and amplitude of the oscillations. With the tapping mode, the probability of damaging the tip is notably reduced, as there are no shear forces like in the contact mode. [175] The measurement is made along a cross-line of a scratch previously made on the film. Thus, the difference in measured height from the lowest point in the sample-free surface of the scratch and a higher point in the unmodified film is interpreted as the film thickness.

X-ray and Electron Spectroscopy

X-rays consist on electromagnetic radiations with wavelengths in the range between 10 nm and 10 pm. They can be formed by the collision of accelerated free electrons or ions against an anode, or atoms in a sample, under the influence of an electric field in vacuum, or also as synchrotron radiation by accelerated particles under magnetic fields. Their energy will depend on the composition of the colliding substrate and the affected shells of the atomic orbitals, from which they also receive their nomenclature, as K, L or M lines. [173] Additionally, the type of interaction of X-rays with a given substance will depend on their radiation energy. Generally, at lower energy the X-rays would be scattered by atoms according to their electron intensity, at medium energy they will affect the electrons in the atomic orbitals and at higher energies there would be interaction with the atom nuclei. Interaction on moderate energy involve excitation of electrons, which will cause X-ray absorption and fluorescence. At energies higher than the binding energies of a given atomic orbital, electrons will be ejected, resulting in ionization. The ionization from the outer-shell will create photoelectrons at a characteristic kinetic energy while the ionization from inner-shell electrons will produce a photoelectric absorption as secondary radiation, causing an Auger electron. [173]

Energy-dispersive X-ray spectroscopy (EDX)

The integration of an X-ray spectrometer in the HRTEM, and also SEM, enables the combination of electron microscopy imaging and spectroscopy analysis. Energy-Dispersive X-ray spectroscopy (EDX), also known as X-ray Energy Dispersive Spectrometry (XEDS), provides information about the elemental composition. It is more recommended to use EDX from the STEM mode for a better switching between the imaging mode and the spectrometry mode.
In EDX analysis, accelerated electrons will collide against the sample on selected points to scan, producing electronic transitions so that the resulting X-rays continuum and X-ray distinguished lines will be recorded as intensity counts. Characteristic peaks, corresponding to the atomic orbitals of the affected electrons, can be shown upon their radiation energy in KeV. For qualitative analysis, these signals are listed according to the elements and the shell of the affected atomic orbitals, as K, L, or M lines. Furthermore, the proportion of an element can be also quantified by integration of the signals. Thus, the composition of a sample can be elucidated. [171–173]

Small-Angle X-ray Scattering (SAXS)

The interpretation of Small Angle Scattering profiles of colloidal dispersions can provide a detailed structural characterization. Small-Angle X-ray Scattering (SAXS) profiles are based on the variations of scattering intensity of X-rays, as *I(q)*, upon the scattering angle vector (*q*) in $Å^{-1}$, according to the scattering angle (θ) (**Equation 2.9**). The behaviour of the elastic scattering of the X-rays beam is attributed to the distribution of electron density of the atoms in the sample. Generally, the scattering intensity can be interpreted as a contribution of the structure factor, *S(q)*, and the form factor, *P(q)* (**Equation 2.10**).

$$q = \frac{4\pi}{\lambda} \cdot \sin(\theta/2) \quad \text{[Equation 2.9]}$$

$$I(q) \approx P(q) \cdot S(q) \quad \text{[Equation 2.10]}$$

P(q) is related to the size of the scattering objects in the dispersion, while *S(q)* is related to the associations and spatial distribution between the dispersed units. At lower *q*-values and for dilute concentrations, *S(q)* tends to unity, so that *I(q)* can be interpreted by the contribution of *P(q)*. The radius of gyration (R_G) can be then obtained by the Guinier approximation (**Equation 2.11**). [177,178]

$$Ln|I(q)| = Ln|I_0| - \left[\frac{q^2 {R_G}^2}{3}\right] \quad \text{[Equation 2.11]}$$

In the higher *q*-region, other parameters can be interpreted, for instance shape and surface-to volume ratio. The larger the *q*, the smaller the scale to interpret, so that large *q*-values are more related to the crystalline structure. By the use of appropriate models fits, other structural information of dispersed colloids can be interpreted. [177,178] In any case, a combination with other characterization techniques is recommendable for supporting the interpretations.

X-Ray Photoelectron Spectroscopy (XPS)

The photoelectric effect is caused when electromagnetic radiation of wavelengths below 200 nm ejects electrons from outer atomic orbitals. In X-ray Photoelectron Spectroscopy (XPS), also known as Electron Spectroscopy for Chemical Analysis (ESCA), the incidence of an X-ray beam on the surface of a solid sample will cause the emission of photoelectrons. The ejected electrons can be recorded according to their kinetic energies (*KE*). These kinetic energies will depend on the photon energy of the incident X-rays ($h \cdot \upsilon$) and the binding energy of the ejected electron (*BE*) for the ionization (**Equation 2.12**), so the binding energies of the ejected electrons can be calculated. [179]

$$BE = h \cdot \upsilon - KE \qquad \textbf{[Equation 2.12]}$$

A photoelectron spectrum can be made by counting the ejected electrons according to their binding energies, usually indicated in keV. The binding energies of the resulting peaks are characteristic of the elements present in the sample, and also the orbitals from which the electrons are ejected and the chemical environment. The signals of a sample to study will be interpreted by comparison in listed libraries of binding energies or XPS spectra of reported compounds. For instance, small shifts in the binding energy are related to changes in the chemical state, so that elements with added valence electrons will have increasing shielding and the measured binding energy will be lowered, and *vice-versa*. Additional features can be interpreted according to intensities and shapes of the signals. Thus, XPS can provide additional information about the elemental and quantified composition, including the oxidation state and the surface functionalization. [167,179,180]

3. Aim and perspectives of the project

The goal of this PhD project consisted on the study of interactions and assembly possibilities between nanoparticles of different liquid dispersibility, directed at the water-oil interface of reverse microemulsions (**Scheme 3.1**).
The reverse microemulsions were based on quasi-ternary mixtures with Aerosol-OT (dioctyl sodium sulfosuccinate, AOT) as surfactant. On one hand, oleyl-capped superparamagnetic iron oxide nanoparticles (SPIO(Ol)NPs) and/or silver nanoparticles (Ag(Ol)NPs) were incorporated in the continuous alkane-alkanol phase. On the other hand, polyethyleneimine-stabilized gold nanoparticles (Au(PEI)NPs) were confined in the dispersed water phase.

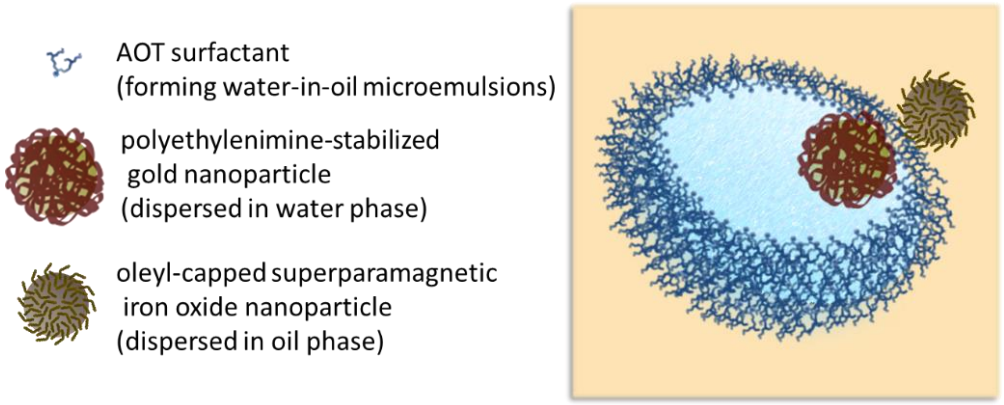

Scheme 3.1. Interpretation of the interfacial assembly of nanoparticles of different solvent dispersibilities at the water-oil interface of reverse microemulsions.

At first, an approach to form heterodimers in reverse microemulsions was explored based on the interactions at the water-oil interface between oil-dispersible and water-dispersible nanoparticles. Nonetheless, other processes were predominating, as the AOT as surfactant should also have a significant influence. An understanding of all the processes involved, regarding both microemulsion properties and nanoparticle interactions, was made up based on multiple characterization properties. First, the microemulsion properties were investigated based on the inter-droplet interactions and the dispersed water. Above the water incorporation capacity, phase-separation made more evident aggregation phenomena of nanoparticles. The control of this aggregation was crucial to obtain defined assemblies of nanoparticles of variable shapes and compositions.

4. Results and discussion

The nanoparticles were strategically made with different surface coating for their selective dispersion in determined liquid phases. Oil-dispersible nanoparticles were capped with oleic acid and oleylamine, while water-dispersible nanoparticles were stabilized with hyperbranched polyethyleneimine (PEI). The oleyl-capped nanoparticles were synthesized in a microwave reactor, using oleic acid and oleylamine as capping ligands, to provide dispersibility in non-polar solvents as well as smaller nanoparticle sizes and higher monodispersity (**Section 1.3**), respectively. [111,181] For the SPIO(Ol)NPs, a thermal decomposition of the iron precursor via polyol method afforded very monodisperse sizes of about 4 nm. [113,151,182] Previous characterization proved their superparamagnetic properties. [151] The Ag(Ol)NPs were synthesized by reduction of the silver precursor in dimethylformamide, [114,183,184] obtaining slightly larger sizes between 4 and 5 nm, less monodisperse than the SPIO(Ol)NPs. The water-dispersible Au(PEI)NPs were synthesized with PEI as both reducing and stabilizing agent. An adapted protocol using higher ratio of gold precursor and shorter reaction times was preferred to obtain lower particle sizes of about 5 nm. [157,185] These nanoparticles were incorporated and combined in reverse microemulsions of quasi-ternary mixtures of different components.

The modulation of microemulsion properties is based on the flexibility of the surfactant film, the water confinement, and the droplet-droplet interactions. The characterization of microemulsions could be made by using multiple methods on the isotropic water-in-oil phases: conductivity, micro-DSC and cryo-SEM for this research. Microemulsion phase properties were compared in past research to study the influence of incorporated polyelectrolytes (**Section 1.2**), as well as their use as templates for the synthesis of nanoparticles (**Section 1.4**). [1,24,62,66–73,156–162] For our case, the characterization of microemulsions is made with the purpose of comparing the effect of using different oil solvents, and specially to study the incorporation of nanoparticles with different solvent affinities based on their surface functionalization.

The nanoparticle properties could be characterized based on their size distribution, optical properties, magnetic responsiveness and electrostatic stabilization. The optical properties observed by UV-Vis absorption and transmittance are attributed to the Localized Surface Plasmon Resonance (LSPR). DLS and TEM used for size distribution and Zeta Potential for electrostatic stabilization. Light microscopy also with polarized light was also used to observe assemblies in larger scale. The morphology of the nanostructures after solvent evaporation could be visualized by Electron Microscopy. More specialized characterization consisted on SAXS, EDX, XPS, FTIR and AFM.

The first part is related to the phase behaviour in the quasi-ternary mixtures containing oil and water phases with AOT as surfactant. The presence of different types of nanoparticles and the different oil solvents are especially compared (**Section 4.1**). For the second part, the modulation of microemulsion properties is explained by diverse characterization methods on the isotropic L_2 phase region. The interactions between droplets and/or nanoparticles are especially helpful to understand subsequent phase transitions and nanoparticle assemblies (**Section 4.2**). The third part is focused on the formation and characterization of biphasic Winsor phases at low AOT content. Thin films of assembled nanoparticles in filament networks were formed after drop-casting of the upper microemulsion phase. Thus, diverse characterization methods before and after solvent evaporation could provide a better understanding about the processes involved (**Section 4.3**). The last part is concerning the resulting magnetic heterocoagulate after phase separation at higher water content with gel formation on the bottom phase. Different phase-transfer procedures afforded magnetic-responsive oil-in-water nanostructures of encapsulated water-dispersible nanoparticle domains in a matrix shell of oil-dispersible nanoparticles (**Section 4.4**).

4.1 Quasi-ternary phase diagrams

*This section is part of the following published articles and manuscripts in preparation:

- "Template-mediated self-assembly of magnetite-gold nanoparticle superstructures at the water-oil interface of AOT reverse microemulsions", *J. Coll Int. Sci.* ***2021****, 581, 44-55*;
- "From Nanoparticle Heteroclusters to Filament Networks by Self-Assembly at the Water-Oil Interface of Reverse Microemulsions", *Langmuir* ***2021****, 37, 8876-8885*;
- "Nanostructured assembly of magnetic and plasmonic nanoparticles transferred from AOT Winsor phases to oil-in-water functional dispersions", *ChemNanoMat* ***2022****, e202200353 (in press)*;
- "Reverse microemulsions with green solvents" (*in preparation*).

The phase diagrams of oil-AOT-water mixtures at room temperature reveal isotropic regions corresponding to optically-clear L_2 phases, at lower water contents (**Figures 1.3, 4.1, 4.2**). These regions are associated to the presence of reverse microemulsions that can incorporate water without destabilization effects, being referred as Winsor type IV systems. At water contents above the incorporation capacity, phase-separation occurs, resulting in other types of Winsor phases: Winsor type II consists on an upper L_2 phase with the excess of water as a remaining bottom phase, Winsor type III contains an additional middle phase to the upper L_2 and the lower aqueous phase and the Winsor type I system contains an upper oil phase and a predominant lower aqueous phase associated to L_1 dispersions (**Figure 1.4**). [19,37] At higher AOT content, viscous dispersions and gel formation are observed, attributed to enhanced interactions and packing effects of microemulsions. [40,45] Thus, phase-separation at higher AOT concentration results in the formation of a viscous, gel-like bottom phase.

The use of pentanol as co-surfactant was thought of utility for a larger incorporation capacity (**Figure 4.1-a**) of water and for the possibility to adjust the microemulsion droplet to smaller, more monodisperse sizes of lower viscosities. Similar phase behaviour is observed when using either heptane-pentanol or hexane-pentanol (1:1 mass ratio) as solvent combinations for the oil phase (**Figure 4.1-b**). For this reason, the formulations containing heptane instead of hexane were later preferred regarding environmental considerations. Additionally, the use of heptane as oil component affords slightly higher incorporation capacity of water. This can be attributed to a larger affinity of heptane, being of similar chain length as the ethyl-hexyl tails of AOT. [34]

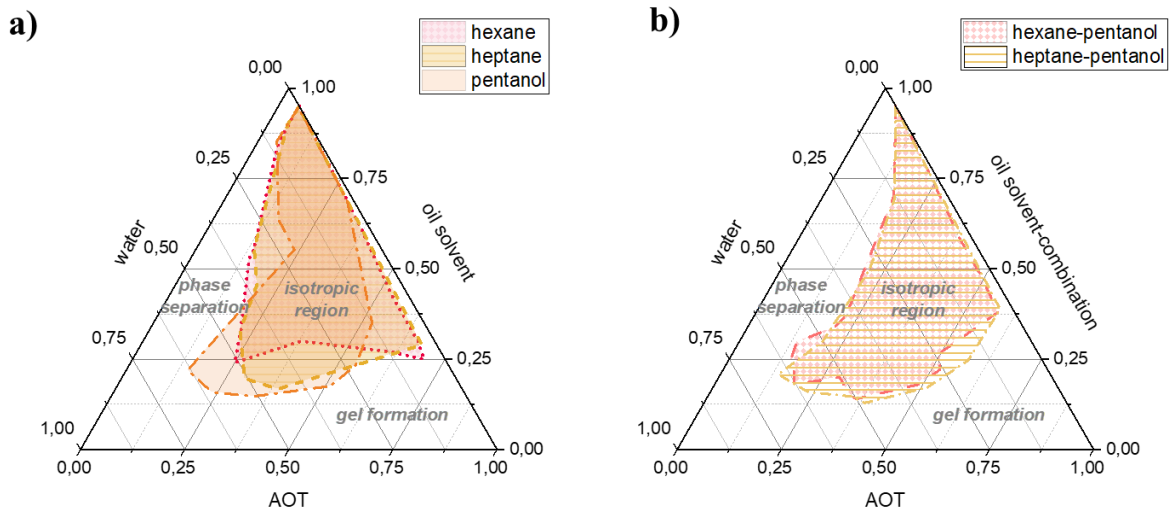

Figure 4.1. Partial phase diagrams of the quasi-ternary mixtures water/AOT/oil, with the oil phase containing different solvent compositions: a) hexane, heptane or pentanol; b) hexane-pentanol or heptane-pentanol in 1:1 mass ratio.

The isotropic L_2 phase regions are not significantly modified when the oleyl-capped nanoparticles are incorporated in the quasi-ternary system (**Figure 4.2**). Noteworthy for the case of SPIO(Ol)NPs, the formation of middle phases was enhanced and the isotropic region at higher water and surfactant content was extended, which is associated to the formation of bicontinuous phases. On the contrary, a significant reduction of the L_2 phase region was observed with the incorporation of PEI-stabilized nanoparticles (**Figure 4.2**). This behaviour differs considerably from previous studies of microemulsions containing PEI instead of PEI-coated nanoparticles. [72] When both types of nanoparticles with different surface coating and dispersibility are incorporated, similar phase behaviour is observed as for the case of Au(PEI)NPs alone, indicating a stronger effect of the AOT-PEI interactions than that of the interdigitation between alkyl chains. Additionally, similar phase behaviour was observed when the SPIO(Ol)NPs were substituted by Ag(Ol)NPs (**Figure 4.2-b**). For some cases, coagulation of

Ag(OI)NPs in AOT microemulsions could happen before reaching the water incorporation capacity, if then this was reduced in the presence of Au(PEI)NPs.

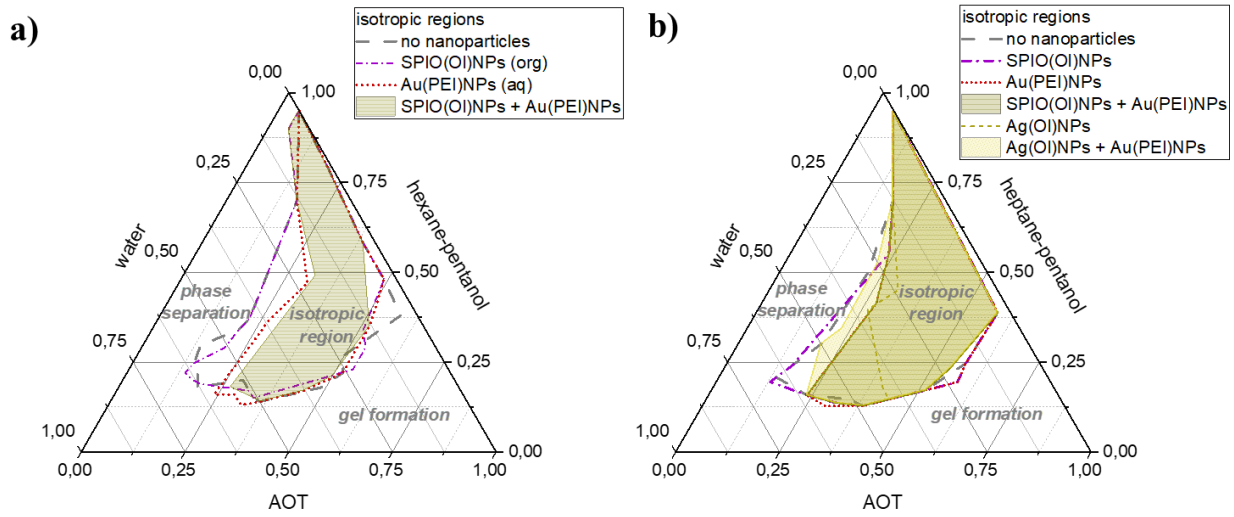

Figure 4.2. Partial phase diagrams of the quasi-ternary mixtures, in absence and presence of 0.5 wt.% SPIO(OI)NPs, 0.5 wt.% Ag(OI)NPs and/or 0.3 wt.% Au(PEI)NPs: a) water/AOT/hexane-pentanol, b) water/AOT/heptane-pentanol.

For a better understanding and more detailed comparisons of the microemulsion properties and the effect of the different types of nanoparticles, characterization of the isotropic L_2 phase region is necessary. Although AOT does not require co-surfactant to stabilize reverse microemulsions due to its branched hydrophobic tails [8,21], the incorporation of middle-chain alcohols as co-surfactants is useful to investigate their effect. Moreover, remarkable effects related to interfacial assembly of the incorporated nanoparticles were found after phase-separation above the water incorporation capacity.

4.2 Isotropic phase properties

*This section is part of the following published article and manuscript in preparation:

- "Template-mediated self-assembly of magnetite-gold nanoparticle superstructures at the water-oil interface of AOT reverse microemulsions", *J. Coll Int. Sci.* ***2021****, 581, 44-55*;
- "Reverse microemulsions with green solvents" (*in preparation*).

Multiple characterization techniques of the isotropic L_2 phase can provide very useful information about the microemulsions regarding inter-droplet interactions, water confinement and inner morphology. Especially different trends upon increasing water content provide an insight about the phase transition of microemulsions from water-in-oil droplets to bicontinuous structures. Thus, conductometric titrations also combined with turbidity, micro-

DSC, UV-Vis absorption and cryo-SEM were used to characterize microemulsions in absence and presence of different nanoparticle combinations.

Conductometric and turbidimetric titrations

The exchange of ions from temporary clustering of microemulsion water droplets can be recorded as electric signals. Especially percolation transitions are identified as a sudden increase in the conductivity above certain water content or temperature. These processes are attributed to the droplet-droplet interactions, which are closely related to the flexibility of the surfactant film. Thus, droplet interactions can be affected by the composition of the oil and water phases, by the type of surfactant and its counter-ion and concentration, and by the presence of additives (**Section 1.2**). [36,48,62,66–72,186–188]

Conductometric titrations upon water content in wt.% were measured at defined oil-to-surfactant mass ratios (ω). Alternatively, turbidimetric titrations can provide a complementary insight about the water incorporation capacity, leading to phase-separation and formation of liquid crystalline mesophases. These effects can be studied for different oil solvents and AOT concentration (**Figure 4.3**), and in the presence of nanoparticles (**Figure 4.4**).

The composition and ratio of the oil phase have a high influence in the conductivity and turbidity behaviour. (**Figure 4.3-a,b,c**). When microemulsions are dispersed only in alkanes, only a slight increase in conductivity is observed, to be later faded out till reaching a second jump step, leading to turbidity and phase separation. The addition of water to reverse microemulsions in pentanol as the oil phase leads to a continuous increase of conductivity (**Figure 4.3-b,c**). When both alkane and alcohol are combined, a first maximum is reached at about 25-27 wt.% water, followed by a plateau and then reaching a second increase at about 50-60 wt.% (**Figure 4.3-b,c,d**). These plateaus have been previously observed for similar reverse microemulsions systems [45,71,188] and are associated to the transition to bicontinuous phases. [8,68,72]

Regarding the comparison of the turbidity appearance (**Figure 4.3-b**), the water incorporation capacity is significantly increased in presence of pentanol. On the other hand, transition to liquid crystalline phase regions are also observed when only heptane is used as oil solvent, indicated by a sudden decrease in the turbidity and a slight decrease in the conductivity, from which similar observations were previously reported. [8,42]

For the comparison of conductivity trends at different surfactant concentration, two dilution lines were chosen along the L_2 phase with hexane-pentanol as the oil solvents. The fixed ratios for each titration line were at ω = 40/60 and ω = 50/50 (**Figures 4.3-d, 4.4**). For both cases, the conductivity was kept at low values up to 10 wt.% water (compositions points, A1, A2) and followed similar trends. With higher incorporation of water, the conductivity increased till

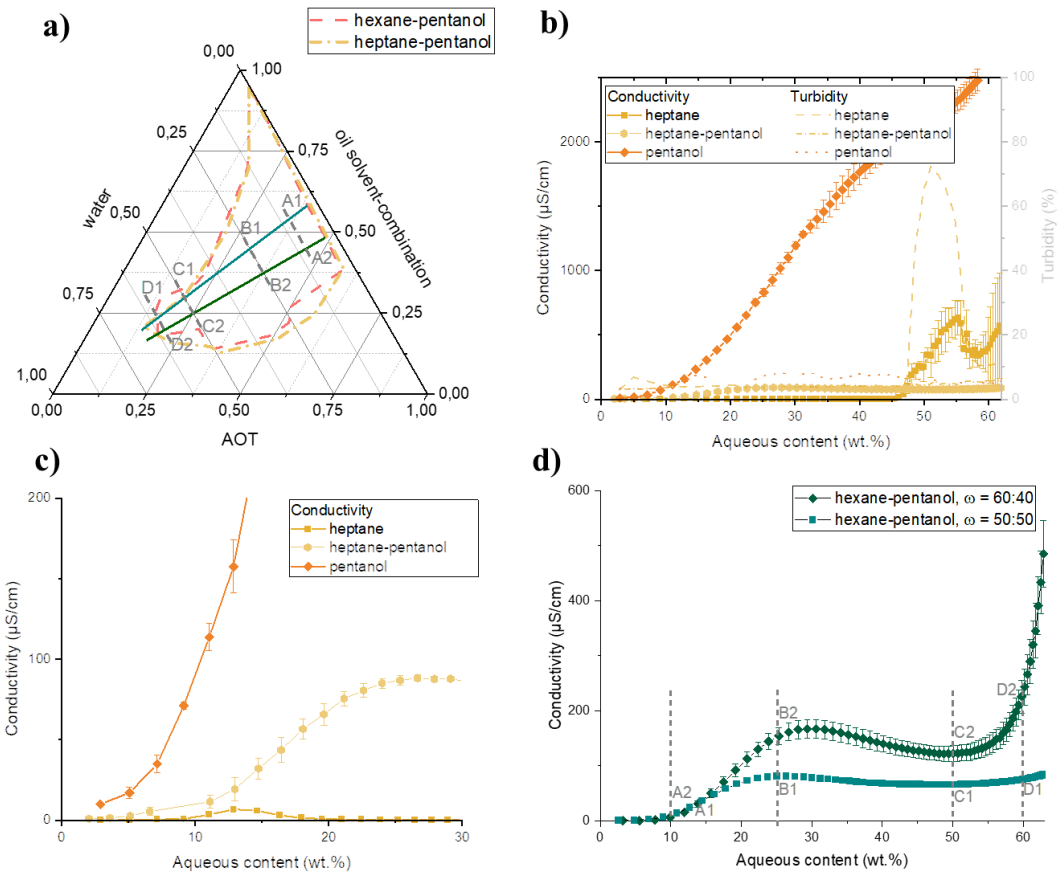

Figure 4.3. a) partial phase diagrams of the isotropic regions for the quasi-ternary mixtures water/AOT/hexane-pentanol and water/AOT/heptane-pentanol with the two titration lines, with corresponding composition points; b) comparison of conductivity and turbidity titration curves of microemulsions in heptane and/or pentanol as oil phase solvents; c) comparison of conductivity titration curves of microemulsions in hexane-pentanol as oil phase at ω = 40/60 and ω = 50/50. (Adapted with permission from *J. Coll. Int. Sci. 2021, 581, 44-55*, Copyright 2020, Elsevier)

reaching a relative maximum at about 25-27 wt.% (points B1, B2). Higher values, with the maximum at slightly higher water content, was reached for ω = 50/50 (point B2). By further addition of water, similar plateaus with relative decrease in the conductivity are observed, slightly more pronounced for ω = 50/50. The final jump in conductivity at values between 50 and 60 wt.% water is also more significant for higher surfactant ratio although the water incorporation capacity is similar for both dilution lines. The larger conductivity values reached for higher surfactant concentration are likely due to a higher quantity of AOT counter-ions.

The effect of nanoparticles on droplet-droplet interactions was studied for reverse microemulsions in hexane-pentanol as the continuous oil phase. Conductivity titrations were performed at both ω = 40/60 (titration line 1) and ω = 50/50 (titration line 2). The presence of SPIO(Ol)NPs or Au(PEI)NPs were compared (**Figure 4.4**). Thus, enhanced increase in conductivity was observed for microemulsions containing SPIO(Ol)NPs while hindered increase appeared for microemulsions containing Au(PEI)NPs. This indicated that the droplet-

droplet interactions are enhanced in the presence of oil-dispersible SPIO(Ol)NPs while hindered in the presence of water-dispersible Au(PEI)NPs (**Scheme 4.1**). Such effects can be attributed to the modulation of the surfactant film properties. For the case of SPIO(Ol)NPs, interdigitation between the oleyl capping ligands and the surfactant tails are likely to increase the microemulsion interactions. On the contrary, Au(PEI)NPs are likely to increase the rigidity of the surfactant films by attractive interaction with the AOT head groups. [66]

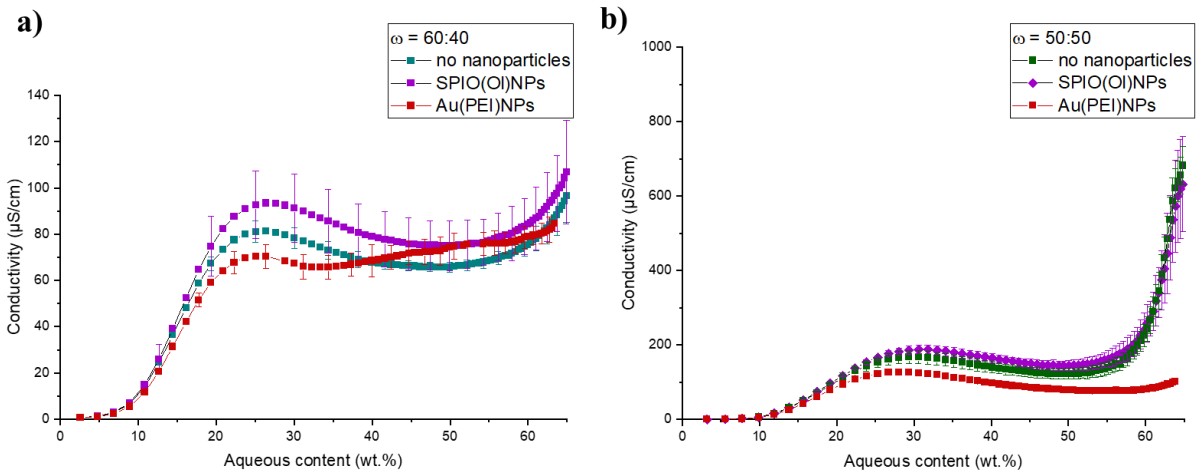

Figure 4.4. Comparison of conductivity titration curves of microemulsions in hexane-pentanol as oil phase, in absence or presence of SPIO(Ol)NPs or Au(PEI)NPs, at different surfactant concentration: a) ω = 40/60, b) ω = 50/50. (Adapted with permission from *J. Coll. Int. Sci.* 2021, *581, 44-55*, Copyright 2020, Elsevier)

For a more concise characterization of the microemulsion properties at specific water contents, micro-DSC, UV-Vis absorption and cryo-SEM were used on defined composition points along the dilution lines.

Micro-DSC

Differential Scanning Calorimetry provides information about glass transitions, appearing initially in the cooling curves, and about the melting behaviour, appearing later in the heating curves. With the increase of temperature on reverse microemulsions, the resulting melting peaks, of characteristic temperature (T_m) and enthalpy (ΔH_m), can be related to the properties of the confined water. Thus, upon incorporation of water, it is possible to differentiate the transitions from bound water (T_m < -10 °C) to interfacial (T_m between -10 °C and 0 °C) and bulk water (T_m = 0 °C). Moreover, the amount of unbound water is proportional to the resulting ΔH_m. [67,72,73,170] . Appearance of free water over a certain critical *W* can be also determined by the crystallization peaks, which can appear at lower temperatures upon smaller dispersed volumes. [55,170] On the other hand, the decrease in the relative size can be attributed to the formation of bicontinuous structures. [55] Although the swelling of microemulsions will favour

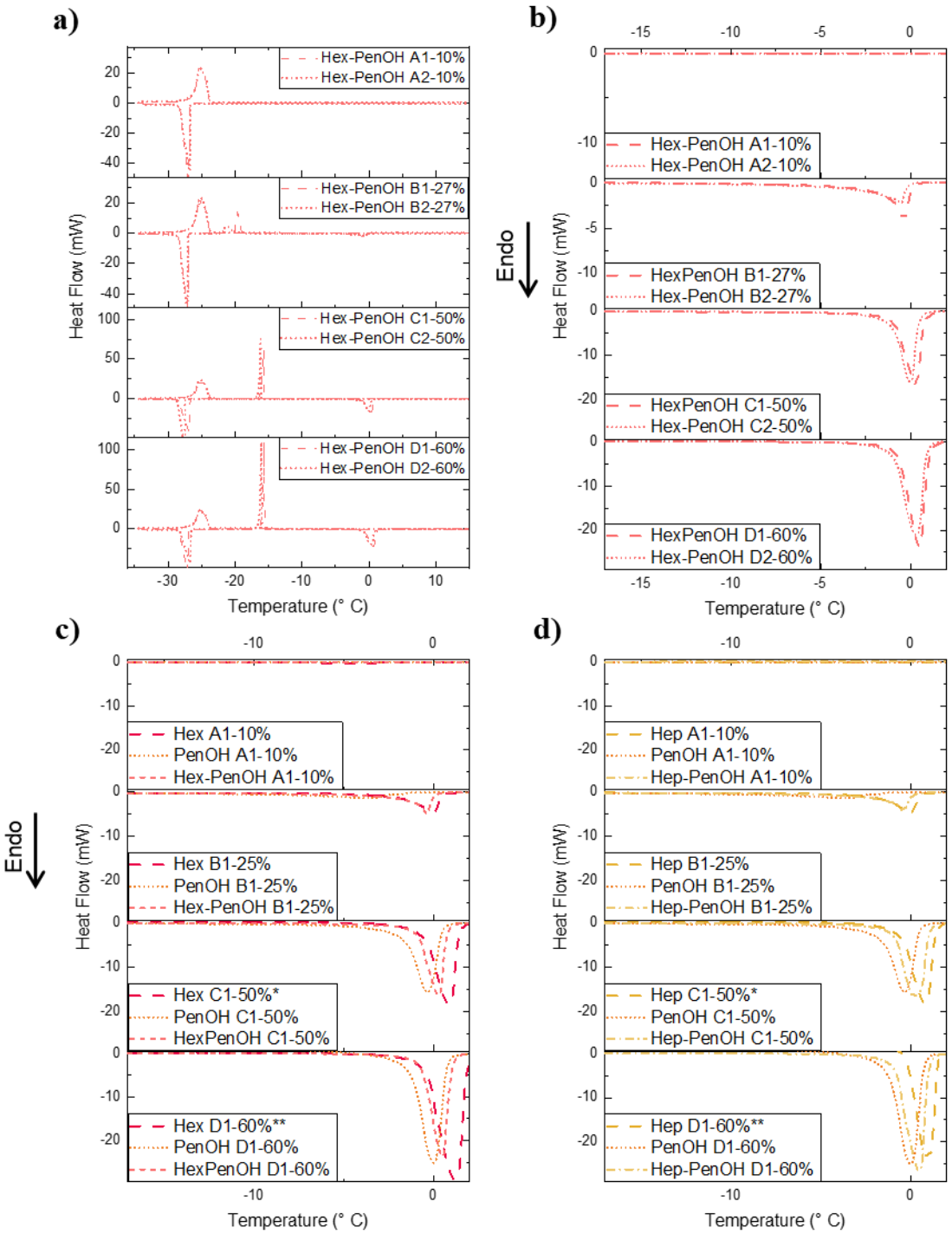

Figure 4.5. Comparison of micro-DSC heating curves of microemulsions at increasing water contents: a) whole calorimetric profile at ω = 40/60 or ω = 50/50, in hexane-pentanol as oil solvents; b) melting peaks at ω = 40/60 or ω = 50/50, in hexane-pentanol as oil solvents; c) melting peaks at ω = 40/60 in heptane, pentanol or heptane-pentanol as oil solvents.

percolation phenomena, [47,54] attributed to a higher flexibility of the surfactant film [30] and to solvated ions [35], the percolation threshold is not directly related with the appearance of bulk water [189].

The micro-DSC profiles, and resulting parameters, are corresponding for the composition points at defined water contents in wt.%: A (10 wt.% water), B (25-27 wt.%), C (50 wt.%) and

D (60 wt.%). Additionally, these points of defined water content were used for the dilution lines at fixed ω as A1, B1, C1, D1 (ω = 60/40) and A2, B2, C2, D2 (ω = 50/50).
The overall calorimetry profiles (**Figure 4.5-a**) consist on an initial cooling process down to -34 °C, followed by a heating process to complete the temperature cycle. Exothermic crystallization or glass-transition peaks appeared at temperatures between -12 and -34 °C in the cooling process, while endothermic melting peaks appeared in the range of -10 to 0 °C in the heating process. The signals at about -25 °C correspond to the undecane used as reference and should remain invariable. Thus, the swelling behaviour of microemulsions at different water contents could be studied according to the magnitude and temperature shifting of the corresponding melting peaks (**Figures 4.5, 4.6, 4.7, 4.8**, **Tables 4.1, 4.2**). For instance, at higher AOT concentration, the presence of melting behaviour corresponding to the confined water is hindered (**Figures 4.5-a,b, 4.7**, **Table 4.2**), in accordance to larger proportion of water molecules interacting with the surfactant film. When pentanol is used as co-surfactant with either hexane or heptane, no freezable water was detected below 10 wt.% content for both dilution lines. This means that all the interstitial water is tightly bound to the AOT head groups, likely through H-bonding and dipole interactions with the sulfonate groups and with the counter-ions. [55,170] The appearance of water melting peaks was mostly observed at water contents above 15 wt.%, whose melting peaks progressively increase in ΔH_m and approach T_m closer to 0 °C with more addition of water. This indicates swelling of the microemulsions with the incorporated water. The swelling behaviour is also affected by the composition of the continuous oil phase (**Section 1.2**). [48,54,55,190] Unlike the higher conductivity values of reverse microemulsions in presence of pentanol (**Figures 4.3-b,c**), the hindered appearance of bulk water suggested by the micro-DSC curves (**Figure 4.5-c,d**) implies that lower segregation of the dispersed unbound water might be related to interfacial interactions. [55] Very similar behaviour was found for hexane-pentanol and heptane-pentanol as oil-phase components (**Figure 4.5-b,c,d**), showing a mayor contribution of the pentanol as co-surfactant in the microemulsion properties.

The effect of the nanoparticles on the melting behaviour at increasing water content is again opposite according to their surface functionalization (**Figure 4.7**). The SPIO(Ol)NPs contributed slightly to lower ΔH_m and T_m (**Figure 4.7, 4.8**, **Table 4.2**), resulting in broader melting curves and enhanced splitting between interfacial water and bulk water. The prevalence of interfacial water besides bulk water can be correlated to enhanced inter-droplet fusion, also observed with reverse microemulsions containing polycations. [73] On the contrary, the presence of Au(PEI)NPs contributed slightly to the appearance of bulk water. This can be attributed to a replacement of water molecules interacting with the AOT head groups at the interface by the PEI coating (**Figure 1.5**) of the Au(PEI)NPs. Thus, less interstitial water is formed in presence of Au(PEI)NPs and the transition of the dispersed water to have bulk water properties is favoured.

Table 4.1. Micro-DSC average values of T_m and ΔH_m corresponding to microemulsions, at representative points of water content along the along the dilution lines of ω = 60/40, in heptane, pentanol or heptane-pentanol as oil phase.

samples	water content (wt.%)	bulk water in heptane		bulk water in pentanol		bulk water in heptane-pentanol	
		T_m / ° C	ΔH_m / (J·g^{-1})	T_m / ° C	ΔH_m / (J·g^{-1})	T_m / ° C	ΔH_m / (J·g^{-1})
	5	-	-	-	-	-	-
A1	10	-3.9	5.96	-	-	-	-
	15	0.1	15.09	-12.6	1.04	-5.1	8.50
	16	0.0	17.67	-11.5	2.88	-4.3	11.38
	17	-0.6	22.70	-10.7	5.12	-3.4	14.75
	20	-0.6	38.54	-6.4	13.21	-0.5	25.45
B1	25	0.0	50.56	-3.7	27.75	-0.4	41.04
	27	0.2	64.72	-2.8	37.92	-0.3	45.13
C1	50	*0.8**	*142.93**	-0.3	119.07	0.3	131.37
D1	60	*0.9***	*178.39***	0.0	162.20	0.5	159.56

* turbid phase; ** viscous, clear phase

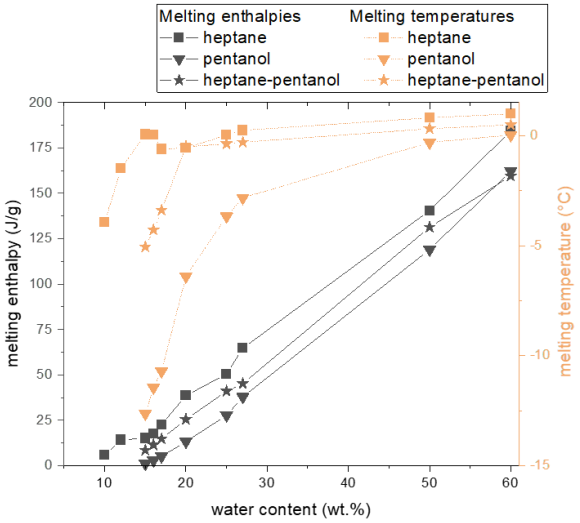

Figure 4.6. Comparison of micro-DSC average values of T_m and ΔH_m from Table 4.1, at representative points of water content along the along the dilution lines of ω = 60/40, in heptane, pentanol or heptane-pentanol as oil phase.

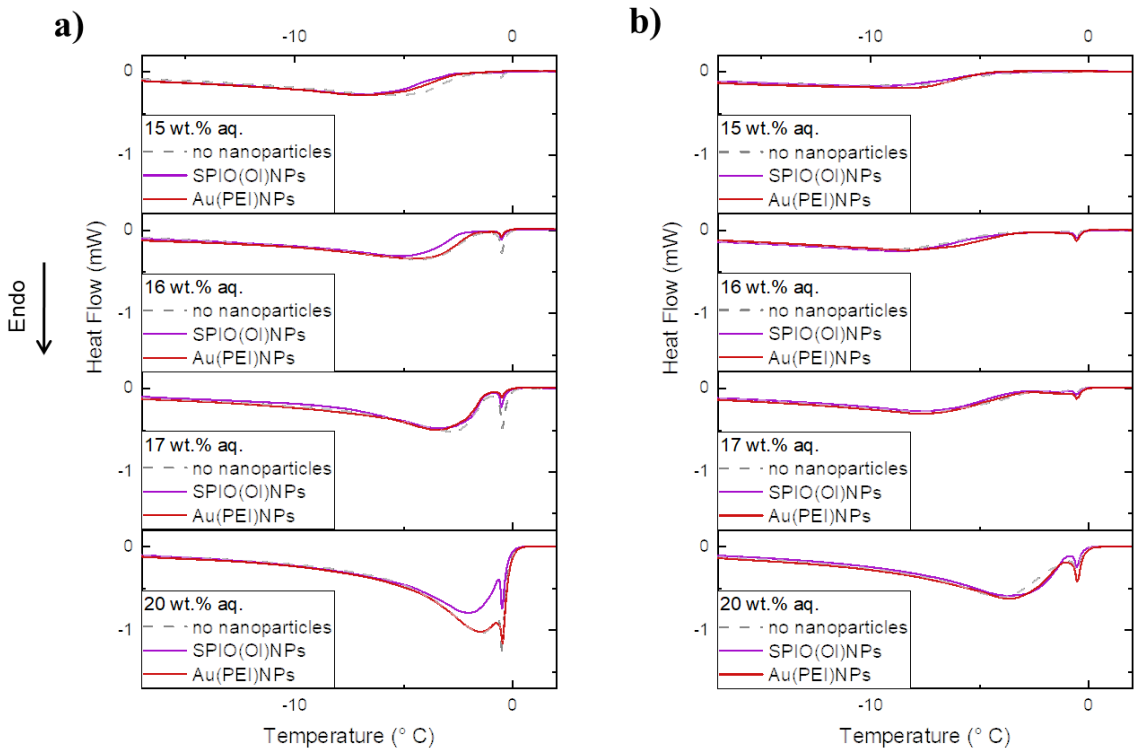

Figure 4.7. Comparison of micro-DSC heating curves of microemulsions at increasing water content in hexane-pentanol as oil phase, in absence or presence of SPIO(Ol)NPs or Au(PEI)NPs, at different AOT concentrations: a) ω = 40/60, b) ω = 50/50.

Table 4.2. Micro-DSC average values of T_m and ΔH_m, corresponding to hexane-pentanol/AOT/water microemulsions, at different wt.% water and ω, in absence or presence of SPIO(Ol)NPs or Au(PEI)NPs. (Adapted with permission from *J. Coll. Int. Sci.* 2021, *581, 44-55*, Copyright 2020, Elsevier)

samples	ω	aq. content (wt.%)	bulk water in hexane-pentanol		(“) with SPIO(Ol)NPs		(“) with Au(PEI)NPs	
			T_m / ° C	ΔH_m / (J·g^{-1})	T_m / ° C	ΔH_m / (J·g^{-1})	T_m / ° C	ΔH_m / (J·g^{-1})
A1	40/60	10	-	-	-	-	-	-
	“	15	-4.8	8.56	-6.7	6.25	-6.6	7.19
	“	16	-1.8	11.29	-5.0	8.88	-4.4	10.20
	“	17	-1.9	15.38	-3.1	15.00	-3.2	14.55
	“	20	-0.5	26.78	-1.3	22.58	-0.7	26.30
B1	“	27	-0.3	53.31	-0.4	50.90	-0.4	55.37
C1	“	50	0.4	142.93	0.3	140.09	*	
D1	“	60	0.5	178.39	0.5	179.94	*	
A2	50/50	10	-	-	-	-	-	-
	“	15	-8.0	2.10	-9.1	1.37	-7.9	1.47
	“	16	-8.8	3.24	-8.4	3.93	-5.4	6.24
	“	17	-7.1	7.07	-7.3	6.51	-7.2	7.21
	“	20	-4.0	18.61	-3.4	18.11	-2.5	19.06
B2	“	27	-0.6	49.64	-0.9	44.40	-0.5	49.72
C2	“	50	0.0	136.91	-0.1	135.10	*	
D2	“	60	0.4	175.05	0.3	174.09	*	

* turbid phase

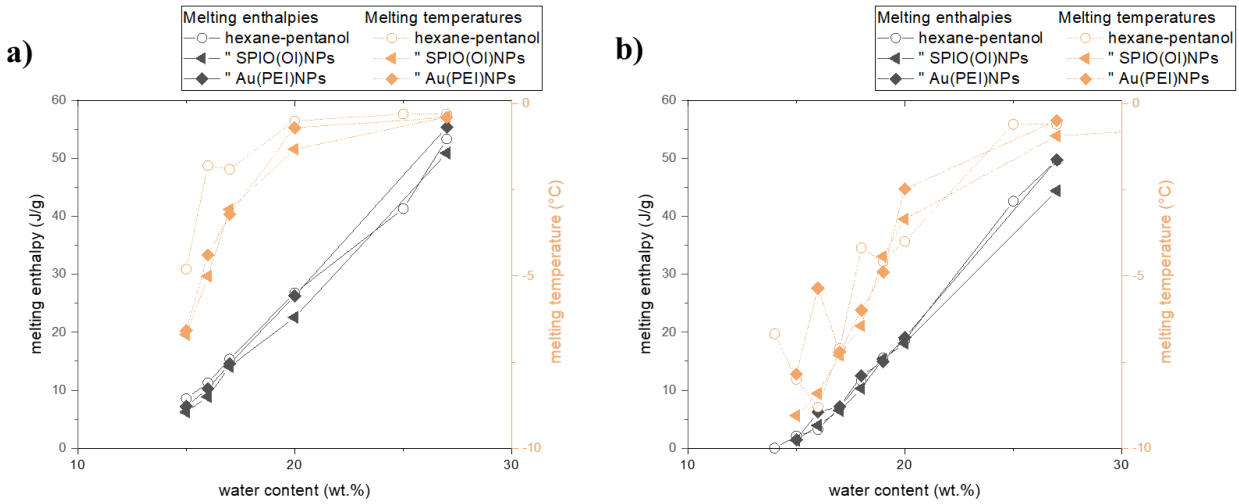

Figure 4.8. Comparison of micro-DSC average values of T_m and ΔH_m with hexane-pentanol as oil phase from Table 4.2, at representative points of water content along the along the dilution lines at different AOT content: a) ω = 60/40, b) ω = 50/50.

UV-Vis absorption

The change of colour of the Au(PEI)NPs from red in the water dispersion to violet after incorporation to the AOT microemulsions, more remarkable upon time, suggested aggregation-related effects. These changes can be better quantified by the UV-Vis absorption signals attributed to the LSPR (see **Section 1.3**). Similar trends could be observed on microemulsions at 10 and 27 wt.% aqueous content with time (**Figure 4.9-a,b**). In agreement with the colour aspect, a red shift of the absorption maximum from 522 to 530 nm was observed together with a damping and broadening of the plasmon band, more evident at longer times in the AOT microemulsions. Red shifts have been previously attributed to shorter inter-particle distances, [4,101] while decrease and broadening of the absorption intensity is related to a reduction in the electron density at the surface by adsorbed species. [101,102,105] This could be related to polyelectrolyte-surfactant complex formation between the PEI and the sulfonate head groups (**Figure 1.5**), triggering agglomeration of the confined Au(PEI)NPs (**Figure 4.9-c**).

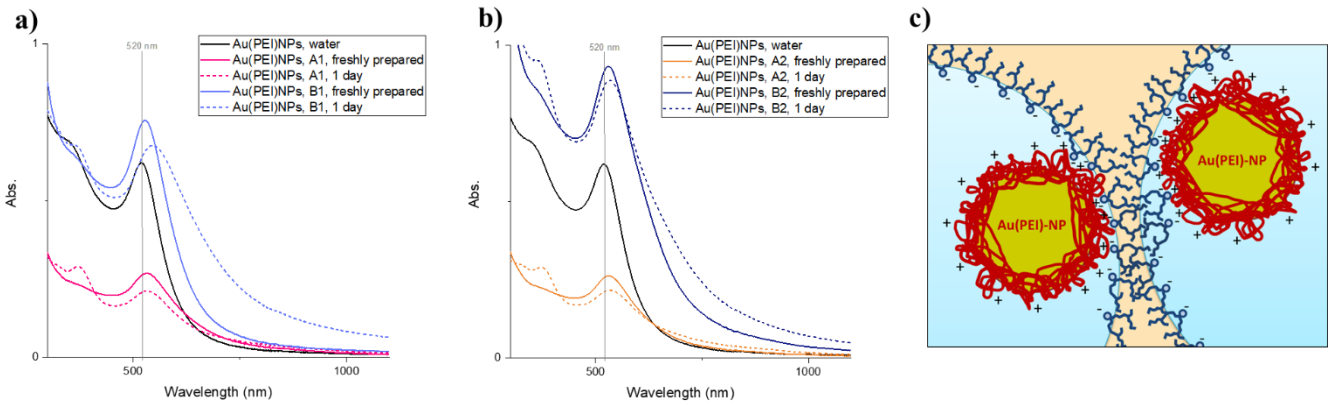

Figure 4.9. a,b) UV-Vis absorption profiles of Au(PEI)NPs in water and in AOT microemulsions with 10 and 27 wt.% aqueous content, in hexane-pentanol as oil solvents, and at different times after incorporation, at ω = 40/60 and 50/50, respectively; c) proposed scheme model for the agglomeration of Au(PEI)NPs by mediation of the AOT surfactant with the PEI coating. (Adapted with permission from J. Coll. Int. Sci. 2021, 581, 44-55, Copyright 2020, Elsevier)

Cryo-SEM

The morphology and phase transitions of microemulsions from water-in-oil droplets to bicontinuous structures can be visualized from cross-section of a freeze-fractured dispersion, without solvent evaporation. [8,68,69,72,174] Samples at different water contents could be compared, and different combinations of solvents, oil-to-surfactant ratios and the incorporation of SPIO(Ol)NPs and/or Au(PEI)NPs resulted in different effects (**Figures 4.10, 4.11, 4.12**).

For all samples with 10 wt.% water, individual droplets of sizes below 50 nm could be observed. When the water content is the range of 25-57 wt.%, a transition into larger droplets of less defined morphologies and agglomeration effects are related to an increase in inter-droplet interactions (**Figures 4.10, 4.11, 4.12**). The presence of pentanol in the oil phase increased the water incorporation capacity so that transition to bicontinuous structures could be observed at higher water contents (**Figures 4.10**). Thus, the effect of pentanol as co-surfactant was revealing its role in the modulation of the flexibility of the surfactant film to form bicontinuous phases, in which w/o droplets coexist with w/o structures. Similar droplet morphologies are observed when using either hexane or heptane as oil components.

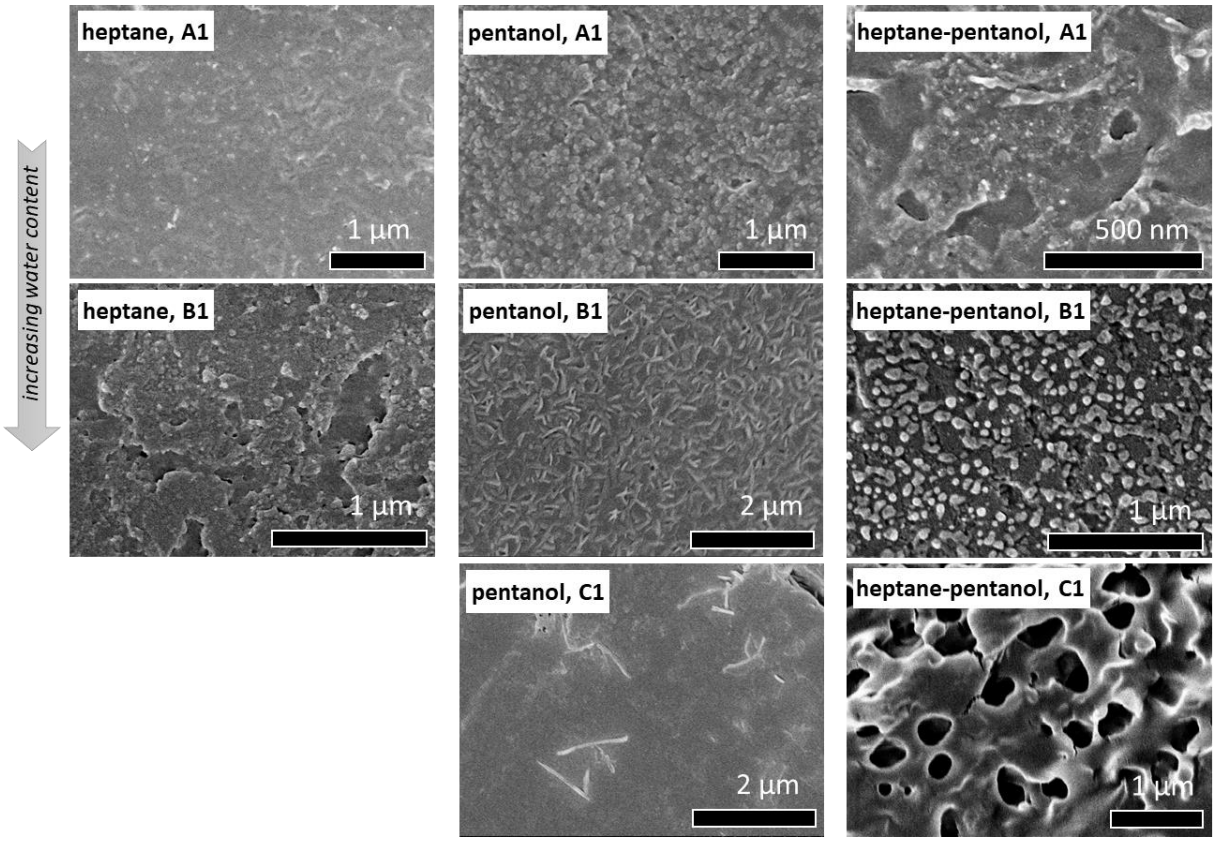

Figure 4.10. Representative cryo-SEM micrographs of the L_2 phase along at 10 wt.% (A1), 25 wt.% (B1) and 50 wt.% (C1) water contents, along the dilution line with ω = 40/60 in heptane, pentanol or heptane-pentanol as oil solvents.

The effect of nanoparticles was observed for microemulsions in hexane-pentanol as solvents for the oil phase (**Figures 4.11, 4.12**). Similar transitions were obtained for both dilution lines, with equivalent morphologies for each water content for ω = 60/40 (**Figure 4.11**), if then the transition to bicontinuous structures appeared at lower water content for ω = 50/50 (**Figure 4.12**). When SPIO(Ol)NPs were incorporated in the AOT microemulsions, slightly larger droplet sizes and increased inter-connections are obtained, contributing to the transition of bicontinuous structures (**Figures 4.11, 4.12**). The presence of Au(PEI)NPs kept similar droplet sizes and morphologies, but with enhanced contrast. Nevertheless, the water incorporation capacity and the flexibility of the AOT film for the transition to bicontinuous structures were significantly reduced with the incorporation of Au(PEI)NPs. The combination of both SPIO(Ol)NPs and Au(PEI)NPs resulted in a synergistic effect, in which the droplet sizes were reduced significantly. This is likely due to an increase of the interfacial area related to directed Au(PEI)NPs- SPIO(Ol)NPs interactions at the water-oil interface.

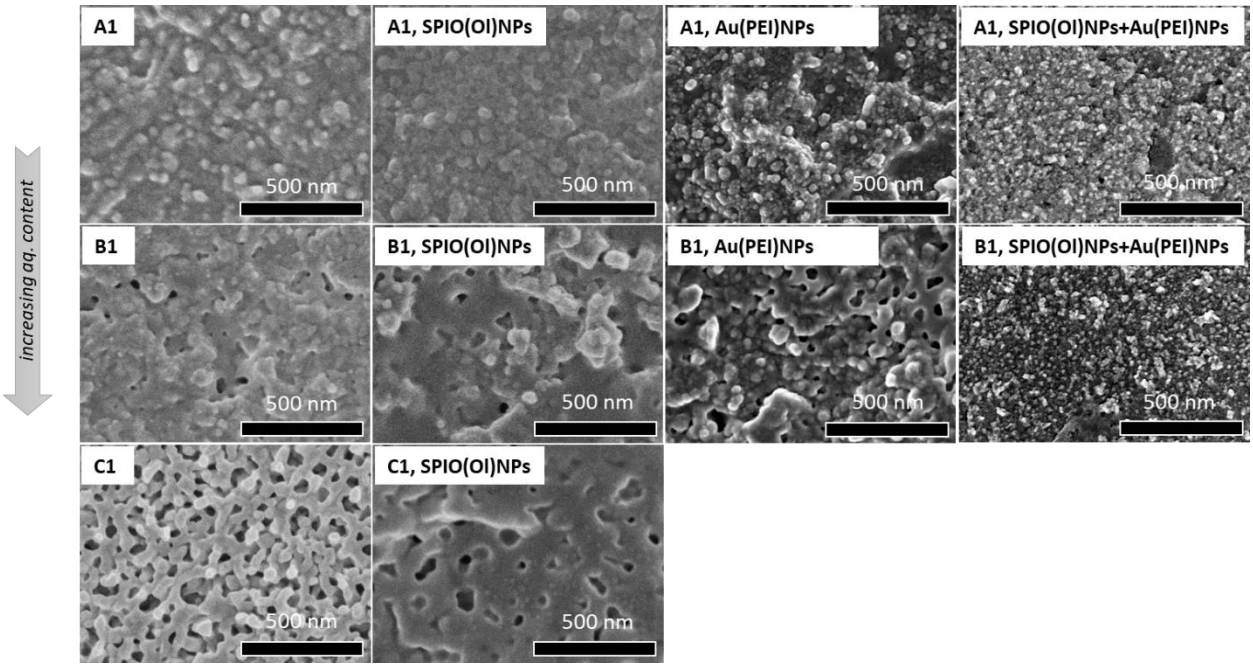

Figure 4.11. Representative cryo-SEM micrographs of the L_2 phase in hexane-pentanol at 10 wt.% (A1), 27 wt.% (B1) and 50 wt.% (C1) water contents, along the dilution line with ω = 40/60 in hexane-pentanol as oil solvents, also in presence of SPIO(OI)NPs and/or Au(PEI)NPs. (Adapted with permission from *J. Coll. Int. Sci. 2021, 581, 44-55*, Copyright 2020, Elsevier)

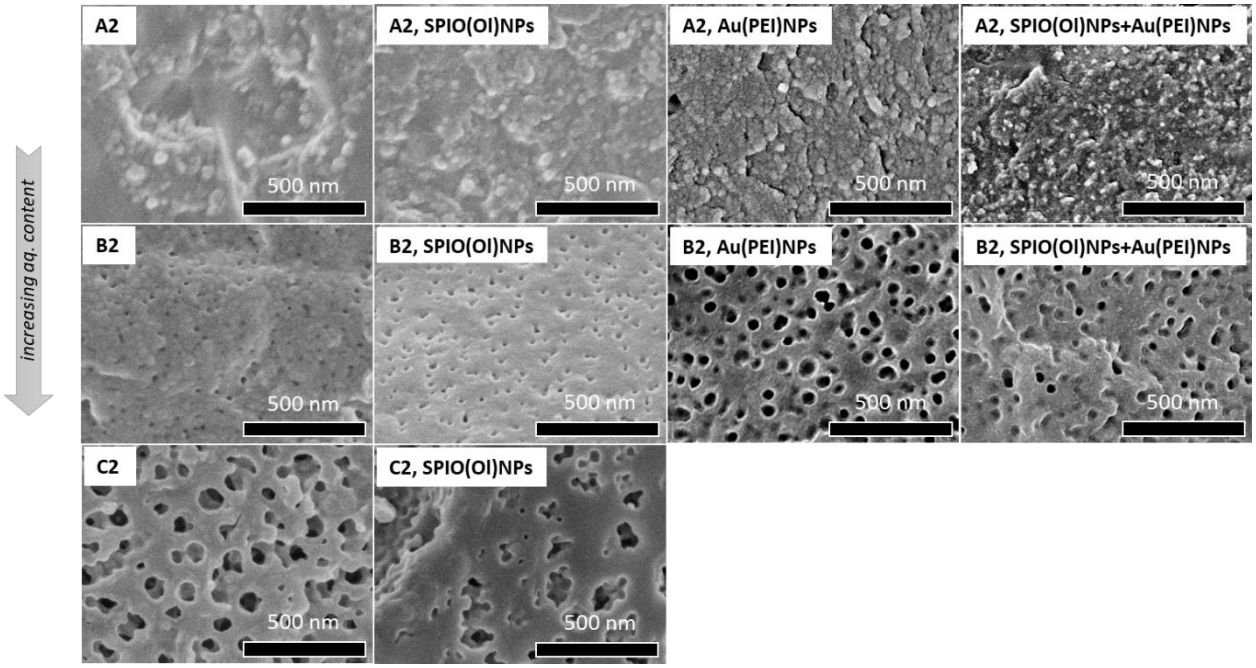

Figure 4.12. Representative cryo-SEM micrographs of the L_2 phase in hexane-pentanol at 10 wt.% (A2), 27 wt.% (B2) and 50 wt.% (C2) water contents, along the dilution line with ω = 50/50 in hexane-pentanol as oil solvents, also in presence of SPIO(OI)NPs and/or Au(PEI)NPs. (Adapted with permission from *J. Coll. Int. Sci. 2021, 581, 44-55*, Copyright 2020, Elsevier)

Conlusions on the isotropic phase

From the previous observations, it can be concluded that different combination of nanoparticles can modulate the microemulsion properties in different ways (**Scheme 4.1**). Oleyl-capped nanoparticles contribute to enhance the droplet-droplet interactions of reverse microemulsions while PEI-stabilized nanoparticles hinder droplet-droplet interactions. These effects should be related to increase or decrease the flexibility of the surfactant film, respectively. In presence of both types of oleyl-capped and PEI-stabilized nanoparticles, a synergistic increase in interfacial area results in smaller, more-interacting droplet sizes.

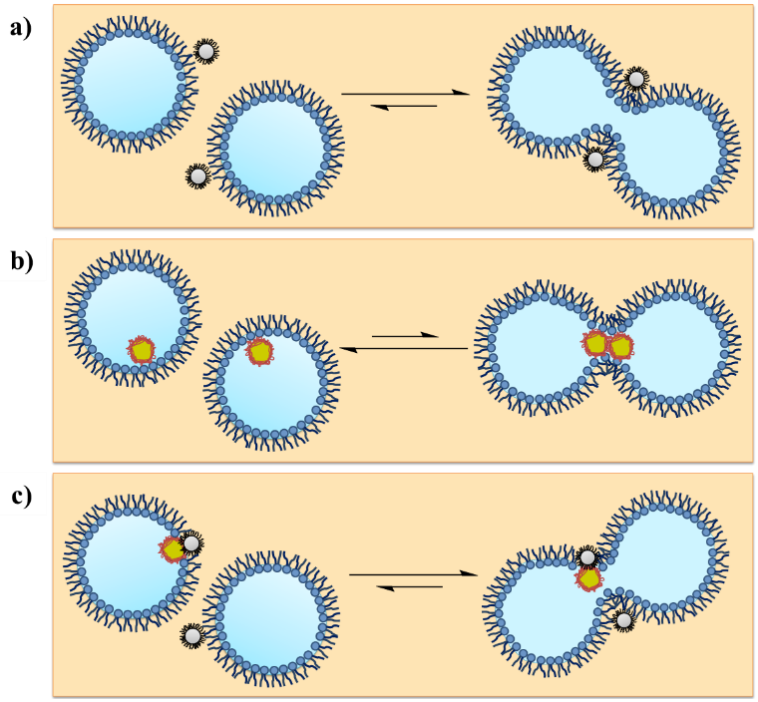

Scheme 4.1. Proposed effects on the inter-droplet interactions by different nanoparticle combinations, based on the modulation of the AOT film: a) SPIO(Ol)NPs, b) Au(PEI)NPs, c) SPIO(Ol)NPs with Au(PEI)NPs. (Adapted with permission from *J. Coll. Int. Sci. 2021, 581, 44-55*, Copyright 2020, Elsevier)

4.3 Assembly in filament networks from Winsor Phase type II

*This section is part of the following published articles and manuscripts in preparation:

- "Template-mediated self-assembly of magnetite-gold nanoparticle superstructures at the water-oil interface of AOT reverse microemulsions", *J. Coll Int. Sci.* ***2021****, 581, 44-55*;
- "From Nanoparticle Heteroclusters to Filament Networks by Self-Assembly at the Water-Oil Interface of Reverse Microemulsions", *Langmuir* ***2021****, 37, 8876-8885*;
- "Versatility about the surface templated-assembly of nanoparticles from reverse microemulsions to filament networks" (*in preparation*).

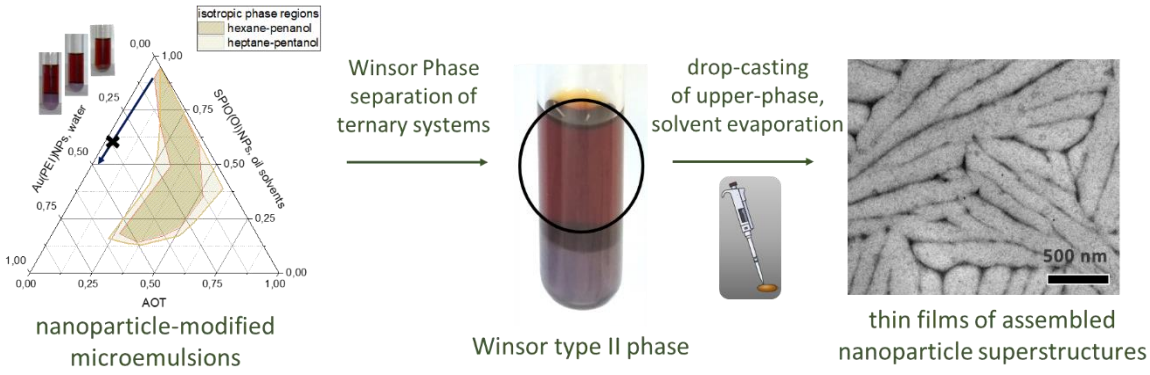

Scheme 4.2. Sequential steps for the formation of WPII systems and the surface assembly into nanostructured filament networks by drop-casting of the upper L_2 phase containing oleyl-capped nanoparticles and PEI-stabilized nanoparticles.

At low surfactant concentration (ω = 95/5) and above the water incorporation capacity, phase-separation results in a Winsor type II phase (WPII) consisting on an upper L_2 phase and the excess of water as a bottom phase. When nanoparticles are incorporated, the oleyl-capped SPIO(Ol)NPs and Ag(Ol)NPs tend to stay in the upper phase while the polycation-stabilized Au(PEI)NPs are found mostly in the bottom phase. Nevertheless, a certain quantity of PEI-stabilized nanoparticles must be confined in the reverse microemulsions of the upper phase. Drop casting of the upper L_2 phase resulted in well-ordered nanoparticle arrangements in filament networks of larger scale above the μm range (**Scheme 4.2**). Note that these hierarchical ordering in anisotropic shapes and larger sizes are made from tiny, spherical nanoparticles. Therefore, we wanted to provide a better understanding of this process, as well as proving the versatility of this approach to obtain thin films of surface-assembled nanoparticles. For this purpose, multiple characterization techniques were performed either in the upper L_2 phase or over the resulting nanoparticle films after drop casting and solvent evaporation.

Upper microemulsion phase

The upper L_2 phase after enough equilibration time (overnight to few days) had the colour provided by the oleyl-capped nanoparticles (brown or yellow) with a characteristic glimmering

effect, while the lower phase was of characteristic violet colour from aggregated Au(PEI)NPs. Multiple characterization methods were made on these dispersions to obtain a better understanding about the interactions involved. These processes should define the self-organization of the AOT dispersions, acting as soft-templates for the subsequent assembly after solvent evaporation over a surface.

Conductivity measurements and electrophoretic mobility along the WPII mixture

A first insight about the microemulsion phase was obtained by measuring the conductivity at different parts of a given WPII mixture. Especially to check whether there are different sub-layers of variable droplet-droplet interactions and ion exchange in the upper L_2 phase, the conductivity electrode was placed at different points of the biphasic WPII system (**Figure 4.13**). No significant differences were found on most of the L_2 phase locations. Conductivity values were also of relatively low conductivity (under 10 µS/cm) in this microemulsion phase, suggesting a limited droplet-droplet exchange. A slight gradient was more remarkable when approaching the inter-phase, in which a dark layer, likely from concentrated nanoparticle, was found. From these regions there was a drastic increase in conductivity, as the presence of aqueous phase was predominating.

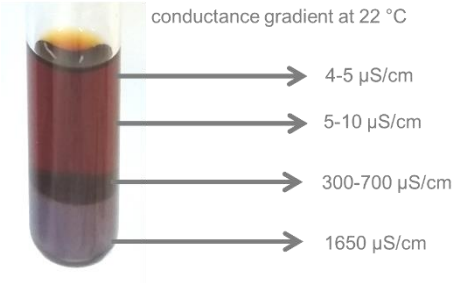

Figure 4.13. Conductivity gradient along the WPII mixture. (Adapted with permission from *Langmuir* 2021, *37, 8876-8885*, Copyright 2021, American Chemical Society)

Additional data about the movement of charges on this upper phase were obtained by Zeta potential from which the electrophoretic mobility was of interest. In any case negligible values of electrophoretic mobility (<0,1 $(\mu m \cdot s^{-1})/(cm \cdot V^{-1})$) were obtained, suggesting again a non-percolating system.

UV-Vis absorption in the upper L_2 phase

The light absorption properties related to the LSPR band of Au(PEI)NPs could provide again useful information about their organization in the L_2 phase. Similar to the behaviour in the isotropic microemulsions (**Figure 4.9**), the red-shifted absorption maximum at 530 nm was an indicative of Au(PEI)NPs aggregation (**Figure 4.14**). [4,101] This red-shift is more pronounced in the presence of SPIO(Ol)NPs, suggesting an enhancement of nanoparticle interactions at the

interface, in similarity to other reports regarding assembled and hybrid nanostructures containing gold nanoparticles. [13,191–193]

The increased absorption intensities of Au(PEI)NPs upon phase equilibration time was quite evident (**Figure 4.14**). Thus, a gradual incorporation of Au(PEI)NPs from the lower phase by diffusion is occurring. A solvent evaporation effect can be excluded by the fact that the changes in the absorption intensity of SPIO(Ol)NPs were insignificant. Moreover, the concentration of Au(PEI)NPs in the upper phase was shown to increase in presence of SPIO(Ol)NPs. Regarding the absorption profiles at different aqueous contents, the incorporation of Au(PEI)NPs at lower addition of aqueous phase did not show a significant contribution. A certain trend regarding an increased incorporation of Au(PEI)NPs was observed only in the range about 20-35 wt.% at increased aqueous content. This should be again related to phase partitioning and diffusion effects of the Au(PEI)NPs from the lower phase to the w/o droplets in the upper phase, in addition to a lower volume fraction of the upper L_2 phase in respect to the increasing lower phase.

Aggregation can look at first not very appealing regarding properties and dispersion stability, even though it occurs under confinement conditions. Nevertheless, this should play a role in the subsequent assembly processes, as demonstrated later with further characterization.

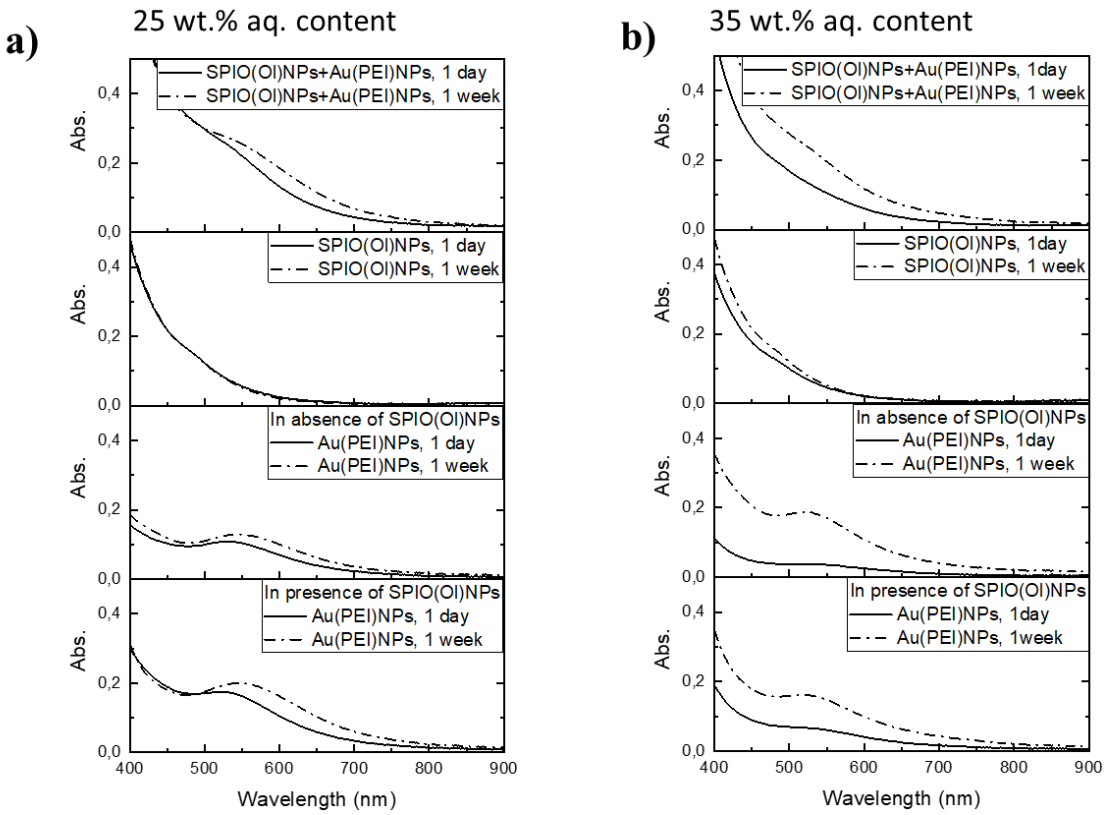

Figure 4.14. UV-Vis absorption profiles of SPIO(Ol)NPs and/or Au(PEI)NPs, in the upper L_2 phase at ω = 95/5, with heptane-pentanol as oil solvents, after one day or one week of phase equilibration, at different water contents: a) at 25 wt.% aqueous content; b) at 35 wt.% aqueous content.

SAXS measurements in the upper L_2 phase and model fittings

The interpretation of Small Angle X-Ray Scattering profiles can provide very useful structural information about liquid dispersions. [177,178,194] In order to obtain a better understanding and comparison of interactions in reverse microemulsions, SAXS was performed on the upper L_2 phases containing different combinations of nanoparticles. The corresponding scattering curves revealed in fact different behaviour in the low-*q* region when SPIO(Ol)NPs or Au(PEI)NPs are incorporated, which is further altered in presence of both types of nanoparticles (**Figure 4.15**) and indicates attractive interactions. Based on extracted parameters of modelling equations, the state and interactions between nanoparticles in the dispersion could be interpreted. As the scattering intensity is much larger in presence of nanoparticles than for the L_2 phase alone, only properties of nanoparticles can be interpreted for this case.

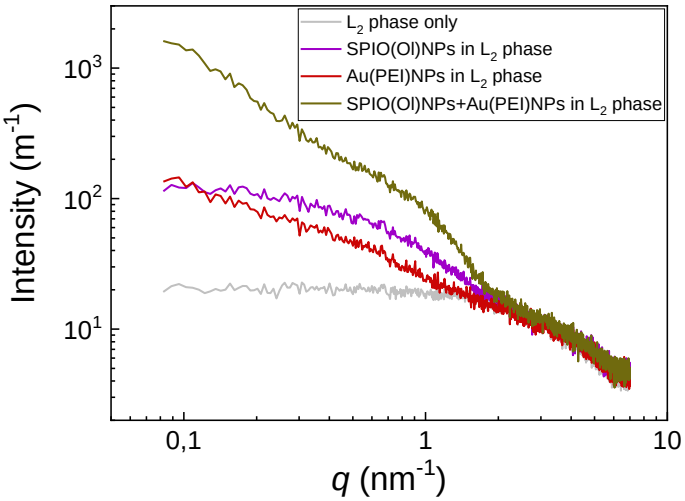

Figure 4.15. SAXS profiles of the upper L_2 phases of WPII systems in absence or presence of SPIO(Ol)NPs and/or Au(PEI)NPs. (Adapted with permission from *Langmuir* 2021, *37, 8876-8885*, Copyright 2021, American Chemical Society)

Two model fittings have been used for this study: the model using Guinier approximation [178] provided information about size distribution of agglomerated -clustered- and free particles; the Random flight model [195–197] provided further information about the number of particles in a cluster, as well as the number density of free and agglomerated particles.

The scattering intensity *I(q)* for a given scattering vector *q* was interpreted as a contribution the following terms (**Equation 4.1**): $I_p(q)$ from non-interacting particles, $I_{cluster}(q)$ from clustered particles and *b* from a constant background.

$$I(q) = I_p(q) + I_{cluster}(q) + b \qquad \textbf{[Equation 4.1]}$$

For single, non-interacting particles, $I_p(q)$ was considered according to the scattering of spheres (**Equation 4.2**), as a combination of the corresponding lognormal number-weighted size distribution of the radii, $f(R, N, \sigma, R_{median})$, and the form factor of a single sphere, $P_s(q, R, \Delta\eta)$. The parameters involved in this interpretation are stated as follows: R as the radius of the sphere and R_{median} as its median value; N as the number concentration of nanoparticles; σ as the width for the size distribution, and $\Delta\eta$ as the scattering length density difference between a particle and the matrix, which is specific for each nanoparticle composition and X-ray energy.

$$I_p(q) = \int_0^\infty f(R, N, \sigma, R_{median}) \cdot P_s(q, R, \Delta\eta)\, dR = \int_0^\infty \left[\frac{N}{\sqrt{2\pi}\,\sigma\,R} \cdot \exp\left(-\frac{\ln(R/R_{median})^2}{2\sigma^2}\right)\right] \cdot \left[\frac{4}{3}\pi\, R^3\, \Delta\eta\, \left(3\frac{\sin(qR) - qR\cos(qR)}{(q\,R)^3}\right)\right]^2 dR \qquad \textbf{[Equation 4.2]}$$

For the first model, $I_{cluster}(q)$ was interpreted with the Guinier approximation, $I_G(q)$ (**Equation 4.3**), in which I_0 is the forward scattering intensity (at q = 0) and R_G is the radius of gyration of the clusters.

$$I_{cluster}(q) \approx I_G(q) = I_0 \cdot \exp\left(-\frac{R_G^2\, q^2}{3}\right) \qquad \textbf{[Equation 4.3]}$$

For the second model, $I_{cluster}(q)$ was stated considering a "random flight cluster" (**Equation 4.4**), [195–197] with a characteristic structure factor, $S_{RF}(q)$ (**Equation 4.5**) in combination with $I_p(q)$ (**Equation 4.2**). Other parameters involved in the structure factor are D as the inter-centre distance of two neighbouring particles, and n as the number of particles or random flight steps in a cluster.

$$I_{cluster}(q) = S_{RF}(q) \cdot I_p(q) \quad \textbf{[Equation 4.4]}$$

$$S_{RF}(q) = \frac{2}{1 - \sin(qD)/(qD)} - 1 - \frac{2\left[1 - \left(\frac{\sin(qD)}{qD}\right)^n\right]}{n[1 - \sin(qD)/(qD)]^2}\,\frac{\sin(qD)}{qD} \qquad \textbf{[Equation 4.5]}$$

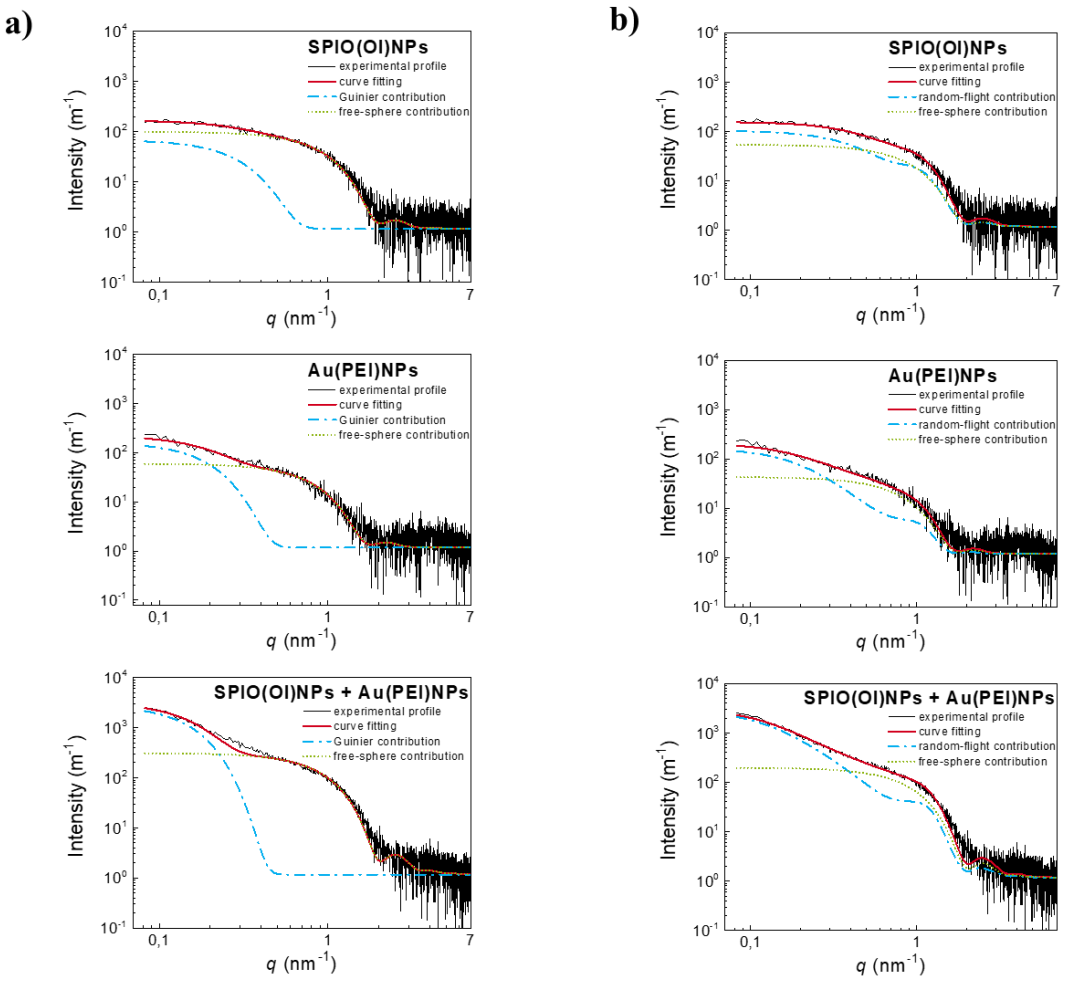

Figure 4.16. SAXS profiles of the upper L_2 phases of WPII systems containing SPIO(OI)NPs and/or Au(PEI)NPs, with corresponding curve fits from each fitting model: a) particle-clusters according to Guinier approximation; b) particle-clusters according to Random Flight approximation. (Adapted with permission from *Langmuir* 2021, *37, 8876-8885*, Copyright 2021, American Chemical Society)

These individual contributions could be plotted for each model by precise fitting [194] for each combination of non-interacting and/or clustered nanoparticles (**Figure 4.16**). Additionally, the values of all parameters could be calculated for each nanoparticle combination in the L_2 phase (**Table 4.3**). For instance, the size of the nanoparticle clusters from SPIO(OI)NPs and/or Au(PEI)NPs could be compared according to the Guinier Model (**Equation 4.3**) and the resulting R_G values (**Figure 4.17-a**). The differences in R_{median} from the free-sphere interpretation (**Equation 4.2**) suggested a major presence of SPIO(OI)NPs in respect to Au(PEI)NPs when both types of nanoparticles are combined. Moreover, the Random-Flight model (**Equation 4.5**) provided an estimation about the number of nanoparticles in a cluster, *n* (**Figure 4.17-a**, **Table 4.3**), as well as their inter-centre distances, *D*. A comparison from the approximated number concentration of free particles and clustered particles was estimated as well from the total *N*, the mean *R*, and the approximated nanoparticle densities and concentrations (**Figure 4.17-b**, **Table 4.3**).

Table 4.3. Calculated parameters from the two model fittings for the interpretation of the SAXS data of the upper L_2 phase with the incorporation of SPIO(Ol)NPs and/or Au(PEI)NPs. (Adapted with permission from *Langmuir* 2021, *37, 8876-8885*, Copyright 2021, American Chemical Society)

	samples		
parameters	SPIO(Ol)NPs	Au(PEI)NPs	SPIO(Ol)NPs + Au(PEI)NPs
Model A: Guiner cluster + "free" spheres			
I_0	68.4	163.8	2904.4
R_G / nm	5.9	9.0	11.5
R_{median} / nm	2.15	2.45	2.15
N / (cm^{-3})	4.8×10^{15}	9.5×10^{13}	1.5×10^{16}
c / ($mg \cdot ml^{-1}$)	1.025	0.113	3.188
Model B: Random-flight cluster + "free" spheres			
n	2	10	25
D / nm	6.5	6.6	6.4
$R_{g,cluster}$ / nm	3.8	8.5	13.0
R_{median} / nm	2.15	2.45	2.15
$N_{cluster}$ / (cm^{-3})	2.5×10^{15}	2.7×10^{13}	5.7×10^{15}
$N_{free\text{-}particle}$ / (cm^{-3})	2.5×10^{15}	6.8×10^{13}	9.3×10^{15}
N_{total} / (cm^{-3})	5.0×10^{15}	9.5×10^{13}	1.5×10^{16}
$c_{cluster}$ / ($mg \cdot ml^{-1}$)	0.530	0.033	1.236
$c_{free\text{-}particle}$ / ($mg \cdot ml^{-1}$)	0.543	0.080	2.022
c_{total} / ($mg \cdot ml^{-1}$)	1.073	0.113	3.258

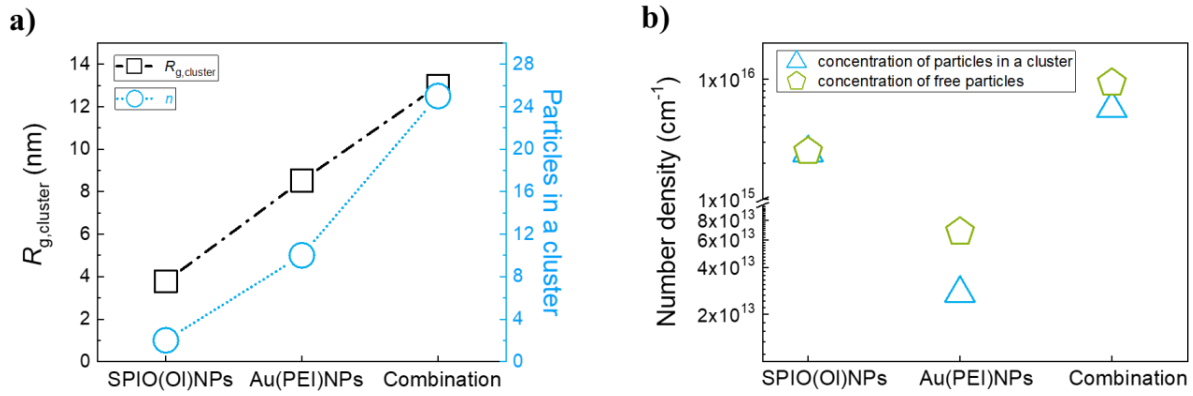

Figure 4.17. Comparison of the calculated parameters form the interpretation of the SAXS profiles of the upper L_2 phases of WPII systems containing SPIO(Ol)NPs and/or Au(PEI)NPs: a) R_G relative to the size of a cluster and n as the number of primary particles in a cluster; b) number density concentration of clustered nanoparticles, N_1, and non-interacting, free nanoparticles, N_2. (Adapted with permission from *Langmuir* 2021, *37, 8876-8885*, Copyright 2021, American Chemical Society)

Regarding the comparison of the cluster size R_G and the number of nanoparticles in a cluster, n, for each L_2 phase in presence of SPIO(Ol)NPs and/or Au(PEI)NPs (**Figure 4.17-a**, **Table 4.3**), aggregation effects were demonstrated in the presence of Au(PEI)NPs. Furthermore, when

the Au(PEI)NPs are combined with the SPIO(Ol)NPs, an enhancement in the cluster growth is shown, suggesting a synergistic effect. The estimated number concentration of agglomerated particles, $N_{cluster}$, also increases significantly in presence of both SPIO(Ol)NPs and/or Au(PEI)NPs (**Figure 4.17-b**, **Table 4.3**). Nevertheless, there is still a remarkable presence of free, non-interacting nanoparticles, which shows that they should also play a cooperative role with the clusters for the formation of assembled nanostructures after solvent evaporation.

DLS measurements in the upper L_2 phase

The presence of larger hydrodynamic sizes of the nanostructures in the upper L_2 phase of the WPII systems than those form the individual nanoparticles was also observed on DLS (**Figures 4.18, 4.19**). Based on the number % of both SPIO(Ol)NPs and Au(PEI)NPs, the hydrodynamic sizes of around 20 nm also indicated nanoparticle clustering, in agreement with the SAXS interpretation. However, it is not clear whether these size distributions are due to the nanoparticle clusters as in SAXS, or also due to the water droplets. No significant differences were observed for the L_2 phases of WPII formulations at increasing aq. content. Contradictory values were provided when only Au(PEI)NPs were incorporated in the WPII systems.

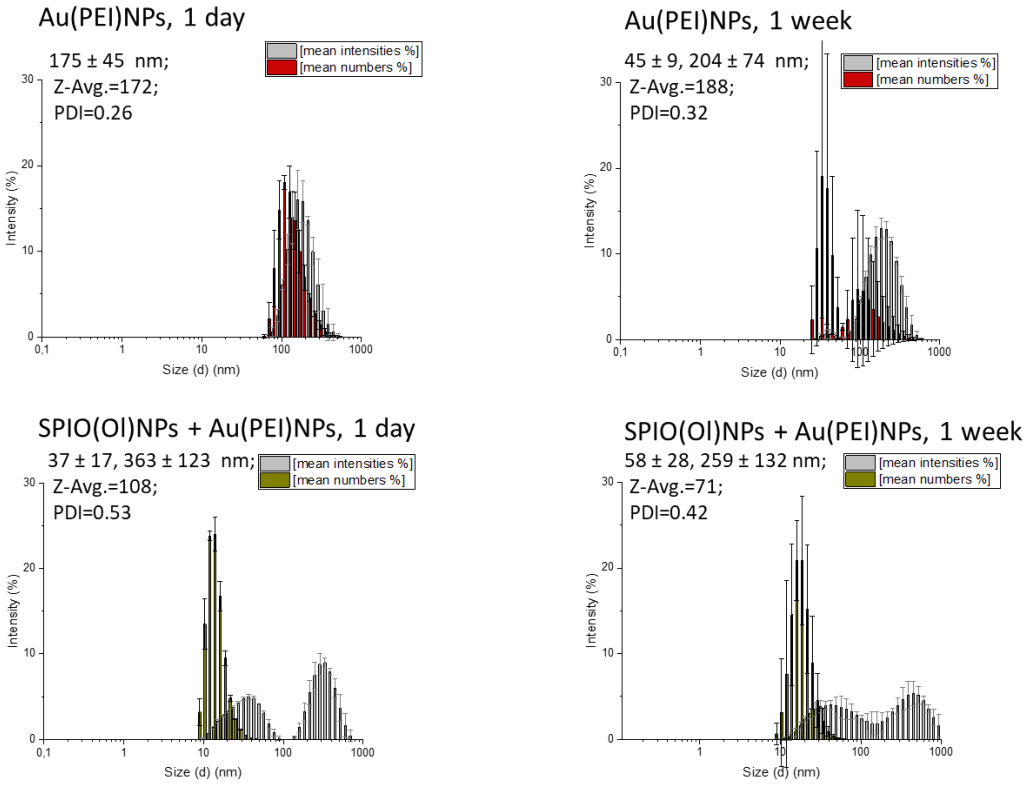

Figure 4.18. DLS plots based on intensity % and number % of the upper L_2 phases of WPII systems containing Au(PEI)NPs without (top row) or with (bottom row) SPIO(Ol)NPs, at 25 wt.% aq. content, after one day (left column) or one week (right column) of phase-equilibration. (Adapted with permission from *Langmuir* 2021, *37, 8876-8885*, Copyright 2021, American Chemical Society)

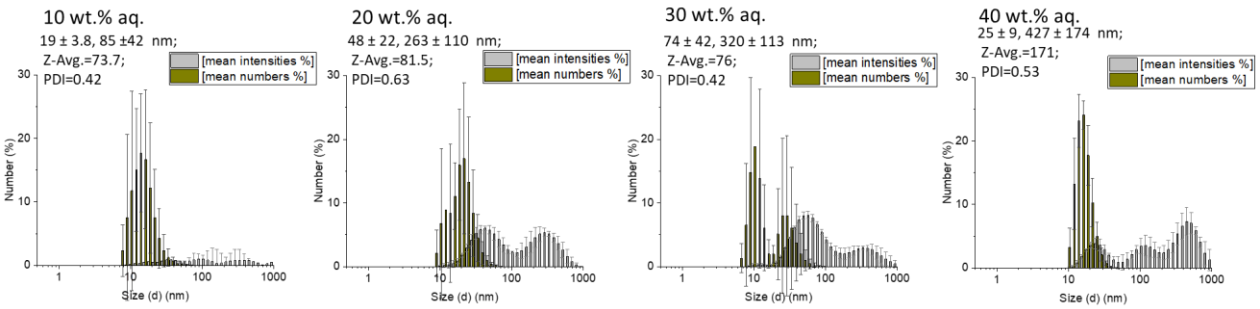

Figure 4.19. DLS plots based on intensity % and number % of the upper L_2 phases of WPII systems containing SPIO(Ol)NPs and Au(PEI)NPs at different aq. contents. (Adapted with permission from *Langmuir* 2021, *37, 8876-8885*, Copyright 2021, American Chemical Society)

Cryo-SEM in the upper L_2 phase

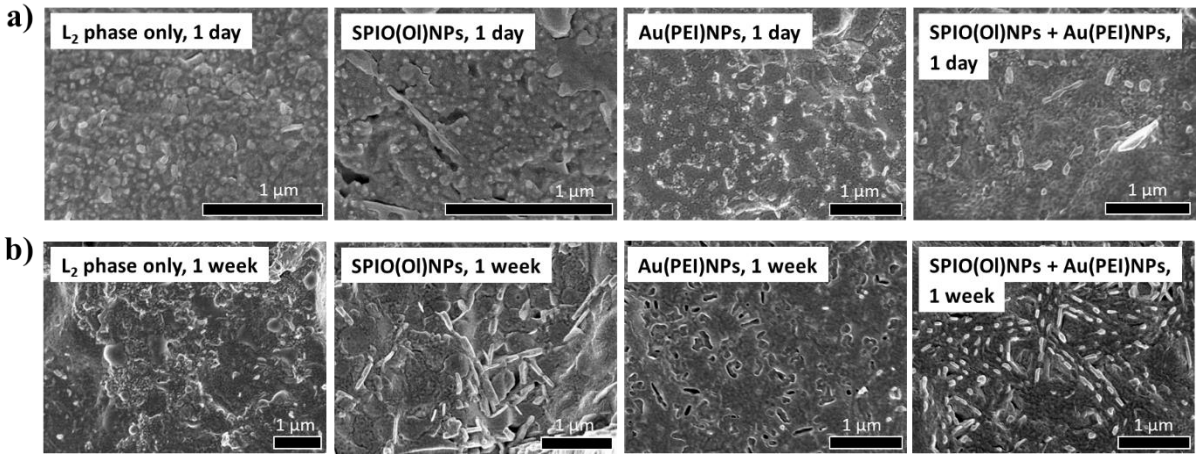

Figure 4.20. Cryo-SEM micrographs of the upper L_2 phases of WPII systems with 30 wt.% water content, in absence or presence of SPIO(Ol)NPs and/or Au(PEI)NPs: a) after one day of phase-separation, b) after one week of phase separation. (Adapted with permission from *Langmuir* 2021, *37, 8876-8885*, Copyright 2021, American Chemical Society)

To visualize the morphology of the microemulsion droplets before solvent evaporation, cryo-SEM was performed on collected samples from the upper L_2 phase. The formation of filament nanostructures was thought to be based on a unidirectional growth of the microemulsion droplets under supersaturated conditions, according to previous research involving the templated synthesis of barite nanofilaments. [198,199] This droplet elongation could be confirmed by cryo-SEM (**Figure 4.20**). Especially a time-dependent elongation of these microemulsion droplets from ellipsoidal to cylindrical structures was observed when comparing the L_2 phases after one day or after one week of phase equilibration of the WPII mixture. This droplet elongation was also observed for samples containing only SPIO(Ol)NPs, which can be based on the enhancement of inter-droplet interactions (**Scheme 4.1**). There is also the possibility that this unidirectional growth is assisted by the presence of pentanol as co-surfactant. [200] In any case, a synergetic effect was observed again with the incorporation

of both SPIO(Ol)NPs and Au(PEI)NPs, in which the cylindrical droplets show a better organization.

Thus, a characterization of the upper L_2 phases resulting WPII mixtures could provide useful information about the properties of these w/o dispersions as a soft-template for the assembly after evaporation of the solvent.

Nanoparticle films after solvent evaporation

Uniform films of relatively large extension can be observed after solvent evaporation of the L_2 phase over a given surface. Multiple surface characterization of the nanostructures films over different surfaces was used to check optoelectronic and structural properties. Thus, UV-Vis transmittance and light microscopy with polarized filter we made on dried samples over glass slides. TEM was made on the usual microscope grid at different water contents and nanoparticle combinations. Samples on a silicon wafer were measured with XPS, AFM and SEM could. The nanoparticle films could be made by drop-casting or by spin-coating. The information provided by these techniques was of interest not only for the interpretation of the templated self-assembly, but also to show different properties and versatility of the nanostructured films.

UV-Vis transmittance of films after drop-casting

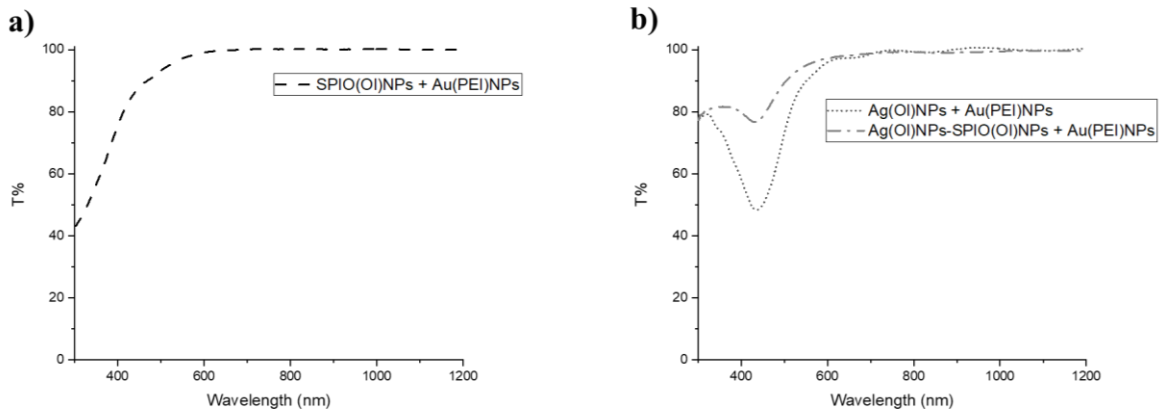

Figure 4.21. UV-Vis transmittance spectra of films from drop-casting of the upper L_2 phase, without the contribution of the glass slide: a) from a WPII mixture in hexane-pentanol at 37 wt.% aq. content in presence of SPIO(Ol)NPs and Au(PEI)NPs; b) from a WPII mixture in heptane-pentanol at 30 wt.% aq. content in presence of Ag(Ol)NPs and Au(PEI)NPs, or SPIO(Ol)NPs-Ag(Ol)NPs 1:1 and Au(PEI)NPs. (Adapted with permission from *J. Coll. Int. Sci. 2021, 581, 44-55*, Copyright 2020, Elsevier)

Transparent films were obtained by drop-casting of the upper L_2 phase over glass slides, from which light transmittance could be measured. Generally, the resulting UV-Vis transmittance

profiles were equivalent to the corresponding UV-Vis absorption in the L_2 phase, with the predominance of the oleyl-capped nanoparticles (**Figure 4.21**). No significant absorption peak was found for the films formed with SPIO(Ol)NPs and Au(PEI)NPs (**Figure 4.21-a**), while a characteristic peak with absorption maximum of about 430 nm was found for the films formed with Ag(Ol)NPs and Au(PEI)NPs, also when both oleyl-capped SPIO(Ol)NPs and Ag(Ol)NPs are combined in the oil phase (**Figure 4.21-b**).

Light microscopy with polarized filter of films after drop-casting

Polarizing microscopy is generally used for the characterization of crystalline structures based on their birefringence. Especially the identification of liquid crystalline phases was of interest to check for optical characterization of the nanostructured films. By comparing the same light microscopy images with and without polarizing filter, a relative change of appearance was observed (**Figure 4.22**). However, the characteristic forms of liquid crystals were not observed. Although the optical properties of these films cannot be attributed to liquid crystals, certain nanoparticle ordering could be suggested.

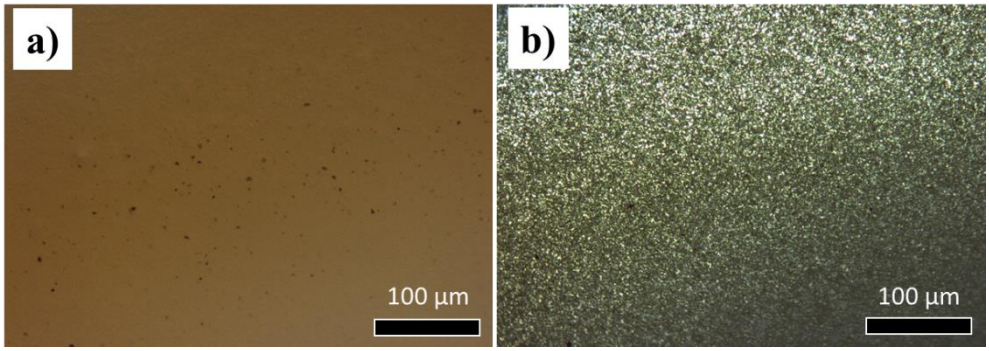

Figure 4.22. Optical light micrographs of thin nanostructured films from drop-casting of the upper L_2 phase from a WPII mixture in hexane-pentanol at 37 wt.% aq. content, in presence of SPIO(Ol)NPs and Au(PEI)NPs: a) without polarizing filter, b) with polarizing filter. (Adapted with permission from *J. Coll. Int. Sci. 2021, 581, 44-55*, Copyright 2020, Elsevier)

TEM of nanoparticle films after drop-casting

The arrangement of tiny, spherical nanoparticles into large, anisotropic filament networks with extension in µm dimensions could be visualized by TEM under different magnifications. The formation of similar nanostructures from AOT microemulsions containing silver ion precursors and their reducing agents had been previously reported. [167,201] In that case, the anisotropic shapes for those cases should result from the reaction between the nanoparticle precursors. For our case, the shape-inducing properties should result from a synergistic effect of combining nanoparticles of different solvent dispersibilities, based on their interactions at

the water-oil interface (**Figures 4.23, 4.24**). A comparison of different films after drop-casting of the upper L_2 phase from WPII phases containing different types of nanoparticles gives an insight to the effects from each nanoparticle combination. It could be observed that the SPIO(Ol)NPs alone can form certain organized packing after solvent evaporation, if then the defined structures are only possible when there is also a minor proportion of Au(PEI)NPs. Thus, different structures are obtained when using only one of the nanoparticle components. Noteworthy, these nanostructures could be observed only from microemulsions with an excess of aqueous phase. TEM was also used for samples resulting from drop-casting of isotropic w/o microemulsions (without phase separation), also containing SPIO(Ol)NPs and Au(PEI)NPs, resulting in indistinguishable images, due likely to an excess of AOT.

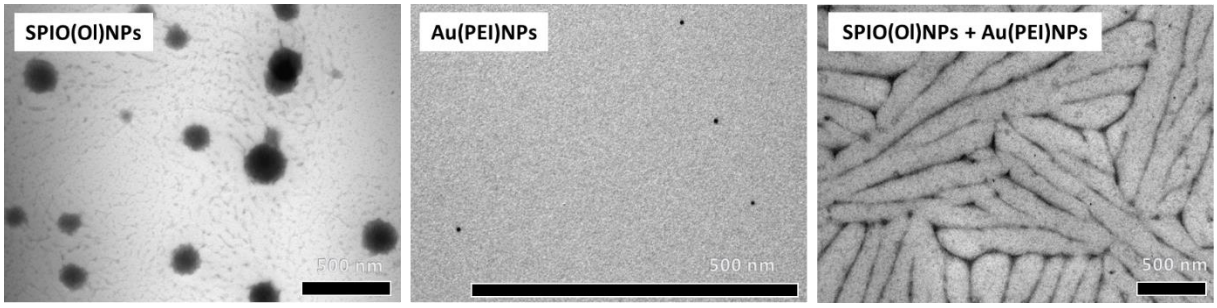

Figure 4.23. TEM micrographs of nanostructures from drop-casting of the upper L_2 phase of WPII with hexane-pentanol as oil solvents, after one week of phase separation with 37 wt.% aq. content, in presence of SPIO(Ol)NPs and/or Au(PEI)NPs. (Adapted with permission from *J. Coll. Int. Sci.* 2021, *581, 44-55*, Copyright 2020, Elsevier)

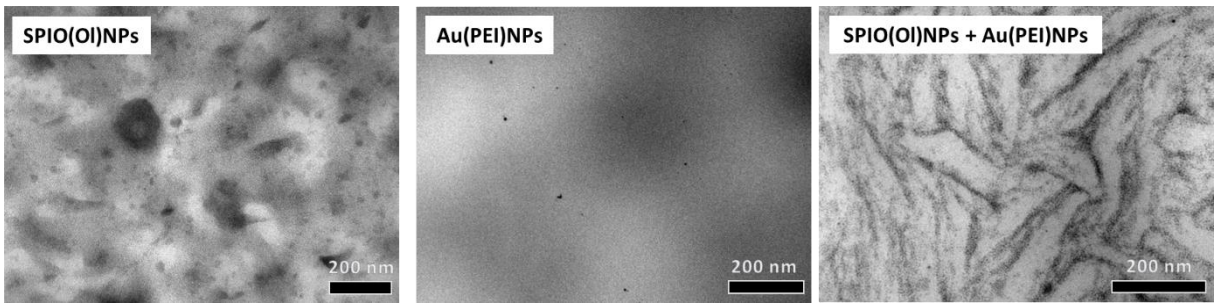

Figure 4.24. TEM micrographs of nanostructures from drop-casting of the upper L_2 phase of WPII with heptane-pentanol as oil solvents, after one day of phase separation, with 30 wt.% aq. content, in presence of SPIO(Ol)NPs and/or Au(PEI)NPs. (Adapted with permission from *Langmuir* 2021, *37, 8876-8885*, Copyright 2021, American Chemical Society)

Various samples were prepared from the L_2 phase of WPII systems, using heptane-pentanol as oil solvents, at increasing water content (**Figure 4.25**). Generally, the further incorporation of water above the isotropic limit causes a larger phase partitioning, increasing the volume proportion of the bottom phase. These partitioning effects should influence the diffusion and assembly of the nanoparticles from the microemulsion phase. For WPII phases with 10 wt.% aqueous content, the surface assembly from the upper phase resulted in an excess of

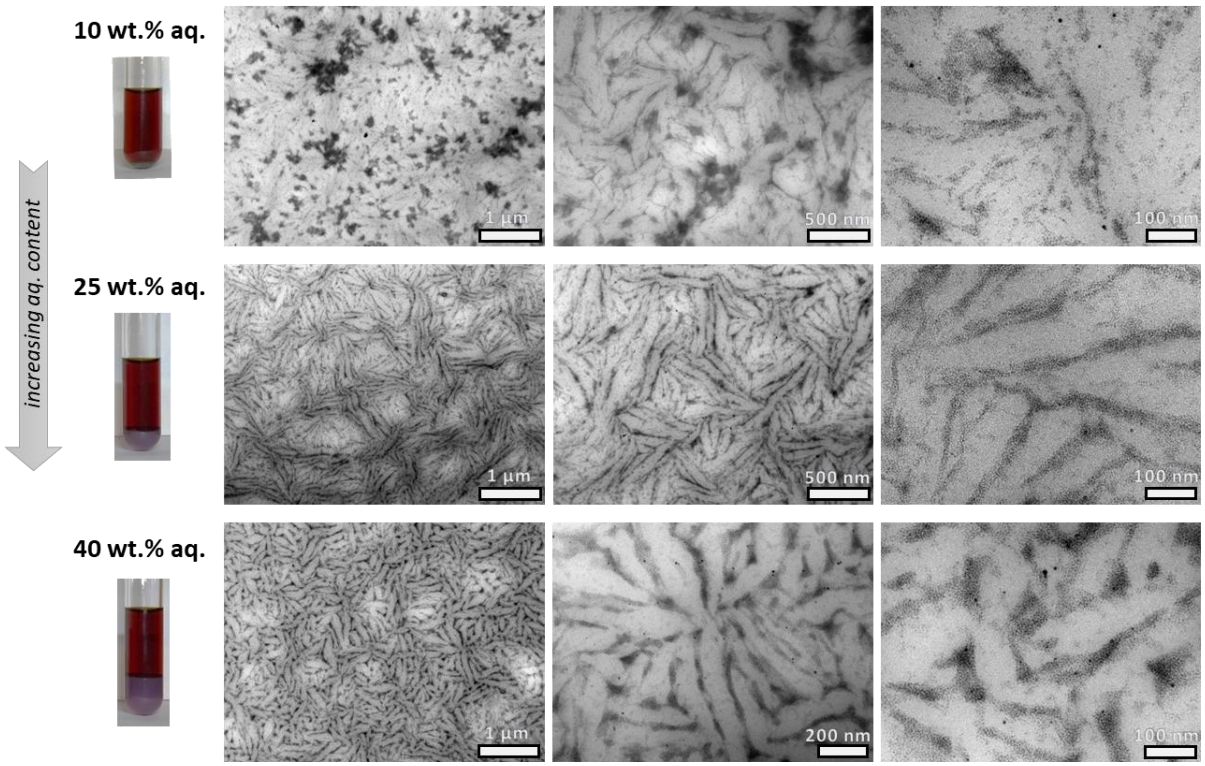

Figure 4.25. TEM micrographs of nanostructures from drop-casting of the upper L_2 phase of WPII in presence of SPIO(Ol)NPs and Au(PEI)NPs, with heptane-pentanol as oil solvents, after one day of phase separation, at 10 wt.%, 25 wt.% or 40 wt.% aq. content. (Adapted with permission from *Langmuir* 2021, *37, 8876-8885*, Copyright 2021, American Chemical Society)

agglomerated Au(PEI)NPs, which could be attributed to the lack of partitioning between separated phases. When phase partitioning is optimized at aqueous content above 20 wt.%, better defined structures could be observed. By further addition of water up to about 40 wt.%, more dense patterns of shorter filament lengths were observed. This effect can be attributed to an increasing presence of heteroclusters which could act as cross-points between nanoparticle filaments, limiting further unidirectional growth. The presence of similar Au(PEI)NP agglomerates from the samples containing only Au(PEI)NPs (**Figures 4.23, 4.24**) and the filament widths of around 25 nm are also in agreement with the cluster sizes interpreted by SAXS (**Figure 4.17-a**).

The solvent components of the microemulsions can also influence on some features of the assembled nanostructures. Although self-assembly into filament networks was possible from hexane-pentanol or from heptane-pentanol as solvent combinations in the oil phase, different time-dependent behaviour was found. For this reason, TEM from L_2 phases was performed at different days of phase equilibration, for WPII systems using either hexane-pentanol or heptane-pentanol, at the same aqueous content and nanoparticles (**Figure 4.26**). Surprisingly, totally opposite time-effects were observed: when using hexane-pentanol, several days are required to obtain better-ordered nanoparticle arrangements; on the contrary, WPII systems with heptane-pentanol afforded well-defined nanostructures after one day of phase

separation, but longer equilibration times resulted in the degradation of these arrangements. On the other hand, defined patterns of nanoparticles can be made in the presence of only heptane as the oil phase solvent (**Figure 4.27**), if then quasi-spherical arrangements were provided. Thus, the presence of pentanol should assist in the formation of elongated patterns.

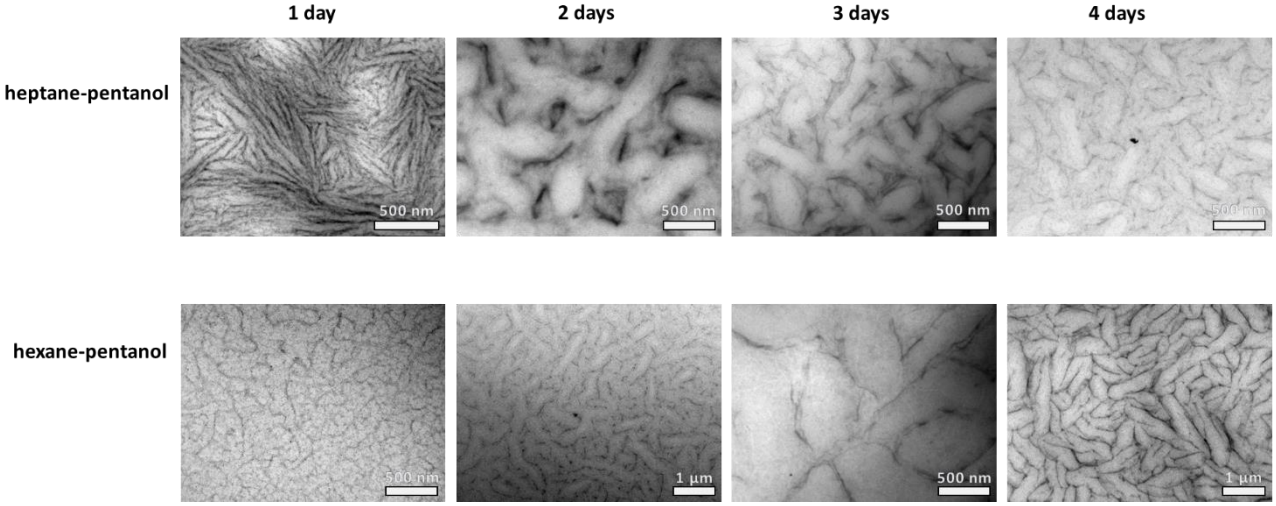

Figure 4.26. TEM micrographs of nanostructures from drop-casting of the upper L_2 phase of WPII after different days of phase equilibration with 30 wt.% aq. content, in presence of SPIO(Ol)NPs and Au(PEI)NPs, using heptane-pentanol (bottom row) or hexane-pentanol (top row) as oil solvents. (Adapted with permission from *Langmuir* 2021, *37, 8876-8885*, Copyright 2021, American Chemical Society)

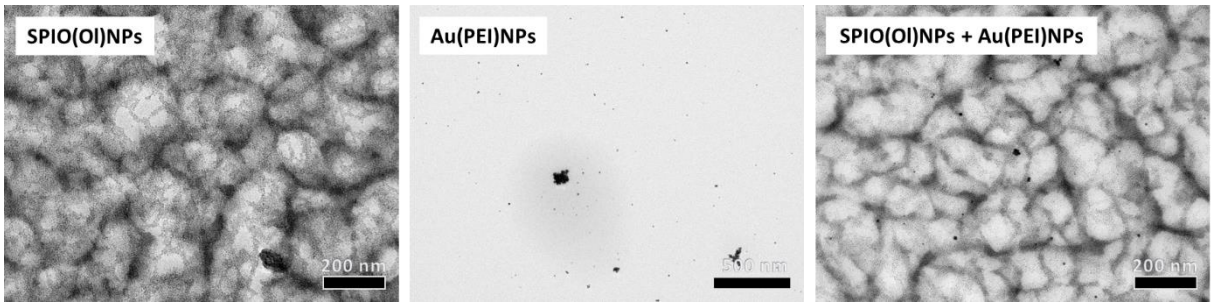

Figure 4.27. TEM micrographs of nanostructures from drop-casting of the upper L_2 phase of WPII with heptane as oil solvent, after one day of phase separation with 30 wt.% aq. content, in presence of SPIO(Ol)NPs and/or Au(PEI)NPs.

These assemblies should be also possible to form by combining nanoparticles of different compositions but keeping their surface functionalization. When the SPIO(Ol)NPs are partially or completely substituted by Ag(Ol)NPs, similar patterns could be observed (**Figure 4.28**). Generally, the presence of Ag(Ol)NPs resulted in the formation of thinner filaments. When both Ag(Ol)NPs and SPIO(Ol)NPs were combined, the patterning was less defined. This could be attributed to a higher polydispersity of the combined oleyl-capped nanoparticles, or to the slightly larger size and size distribution of Ag(Ol)NPs. Although the resulting morphologies from Ag(Ol)NPs with Au(PEI)NPs might slightly differ from the organization of SPIO(Ol)NPs

with Au(PEI)NPs, the organization in filament networks is preserved. Therefore, possible considerations about the superparamagnetic properties of the SPIO(Ol)NPs for the patterning effects in the nanoparticle assemblies should not be relevant.

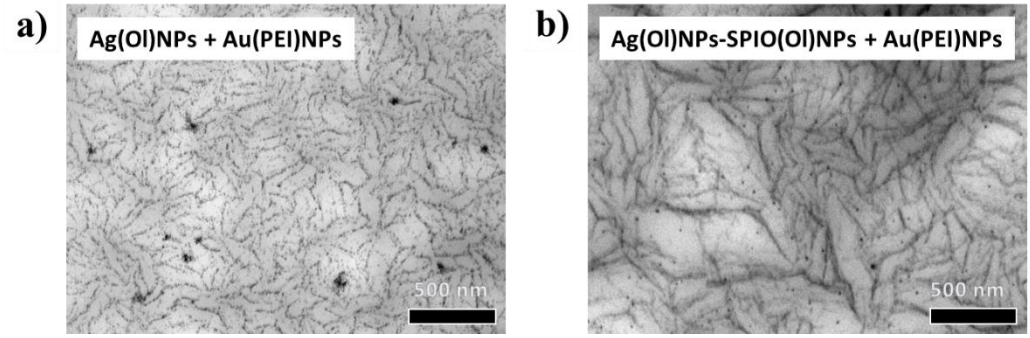

Figure 4.28. TEM micrographs of nanostructures from drop-casting of the upper L_2 phase of WPII after different days of phase equilibration with 30 wt.% aq. content, using heptane-pentanol as oil solvents, with different nanoparticle combinations: a) Ag(Ol)NPs and Au(PEI)NPs, b) Ag(Ol)NPs with SPIO(Ol)NPs in 1:1 ratio and Au(PEI)NPs.

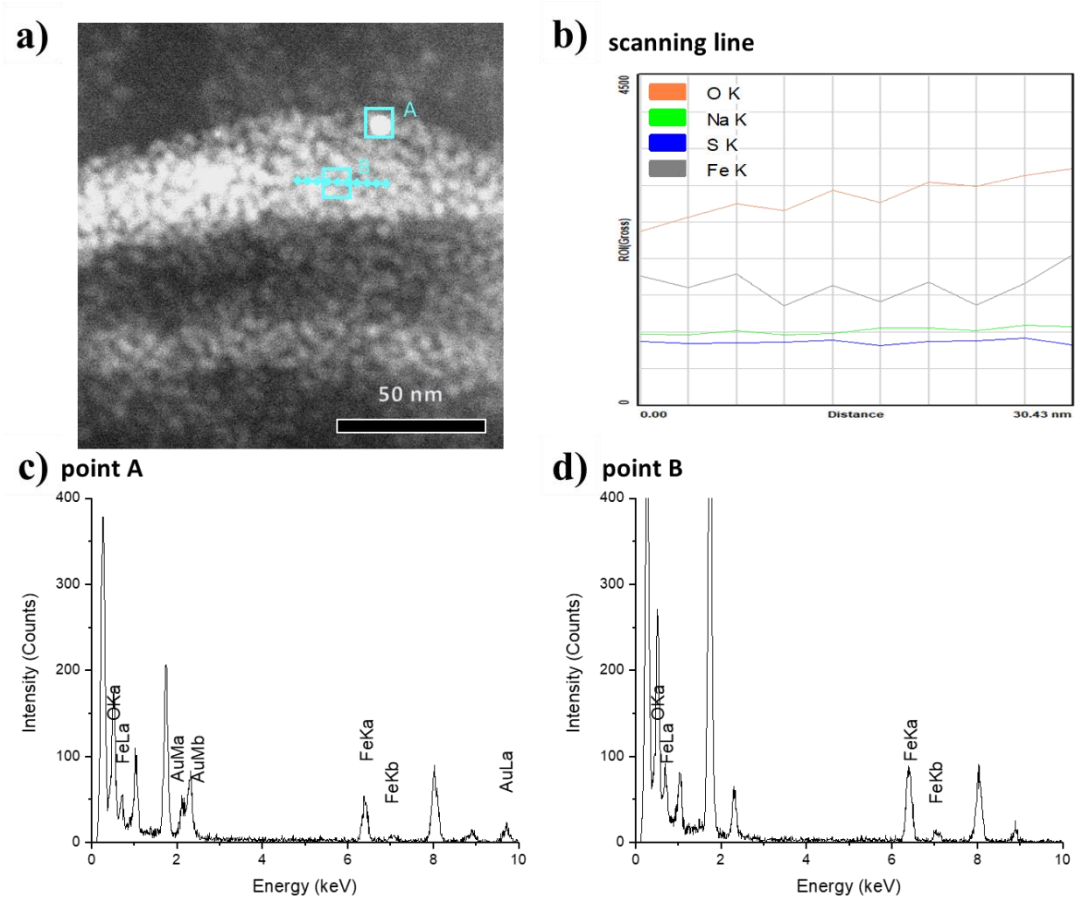

Figure 4.29. a) HRTEM-STEM micrograph from drop-casting of the upper L_2 phase of a WPII mixture with SPIO(Ol)NPs and Au(PEI)NPs in hexane-pentanol; b) corresponding elemental distribution counts along the line scan c, d) corresponding EDX spectra at a point close to one Au(PEI)NP at a point close with only SPIO(Ol)NPs, respectively. (Adapted with permission from *J. Coll. Int. Sci.* 2021, *581, 44-55*, Copyright 2020, Elsevier)

HRTEM and EDX of nanostructured filament networks

By higher magnification in HRTEM, the arrangements between nanoparticles could be better distinguished. Most nanoparticles were of monodisperse sizes of about 4 nm, while larger nanoparticles of about 7 nm were in minor proportion. The elemental analysis provided by EDX in the STEM mode confirmed that most of the components corresponded to the SPION(Ol)NPs, if then a minimum part of Au(PEI)NPs, corresponding to the larger sizes, must be necessary to form the resulting hierarchical structures. An EDX line scanning line along a given filament indicated periodic arrangements between the SPION(Ol)NPs with regular inter-particle distances of about 2 nm, which provides further supporting evidence about crystalline ordering (**Figure 4.29**).

XPS of films after drop-casting

Certain aspects concerning the interactions of nanoparticles after incorporation in the AOT dispersions required further investigation. A possible method to provide more information about the effect of AOT at the nanoparticles surface is based on the emitted photoelectrons by the incidence of X-rays at their binding energies. [167,180] Especially the interactions between Au(PEI)NPs and AOT were of interest, for a better understanding about whether the sulfonate head groups have just electrostatic interactions with the PEI coating or also a direct affinity with the gold surface. [65] Other studies regarding nanoparticle dispersions in nonpolar solvents with AOT revealed that the concentration of AOT can also affect the nanoparticle interactions, behaving as charge controlling agent, in addition to the functionalization with capping ligands. [202] Thus, the differences on the XPS bands of the SPIO(Ol)NPs in the L_2 phase compared to the dispersion in hydrocarbon solvents could provide information the interactions of AOT at the iron oxide surface (**Figures 4.30, 4.31**). However, spectra from the L_2 phase containing Au(PEI)NPs could not be analysed, due to beam damages of the respective samples, if then information about the PEI-coating could be provided (**Figure 4.30-a**).

When the SPIO(Ol)NPs are incorporated in the upper L_2 phase of a WPII mixture, the resulting XPS signals are significantly reduced in intensity compared from the dispersion in only oil solvents (**Figures 4.30-c,d, 4.31**). Focusing on the deconvoluted Fe 2p peaks (**Figure 4.31**), the respective assignments can be made according to a previous report on similar oleyl-capped iron oxide nanoparticles. [180] The most remarkable changes when the Fe(Ol)NPs are in the microemulsion phase include the disappearance of deconvoluted bands at 719 and 733 eV and the Fe^{3+} satellite peaks at 716 and 729 eV. This reduction in intensity of the satellite peaks can be attributed to an increase of electrostatic interactions or to more uncoordinated atoms at the surface, [180] which implies that the SPIO(Ol)NPs surface can be modified in the presence of AOT microemulsions. When comparing the deconvoluted bands of the C 1s and the O 1s signals (**Figure 4.32**), a significant enhancement in the bands assigned to carboxylate groups

is observed when the SPIO(Ol)NPs are in presence of AOT. Especially the predominance of monodentate ligands in respect to bidentate ligands for SPIO(Ol)NPs in the L_2 phase can be attributed to a partial de-capping of the SPIO(Ol)NPs, which should influence on their packing organization upon solvent evaporation. [118,203]

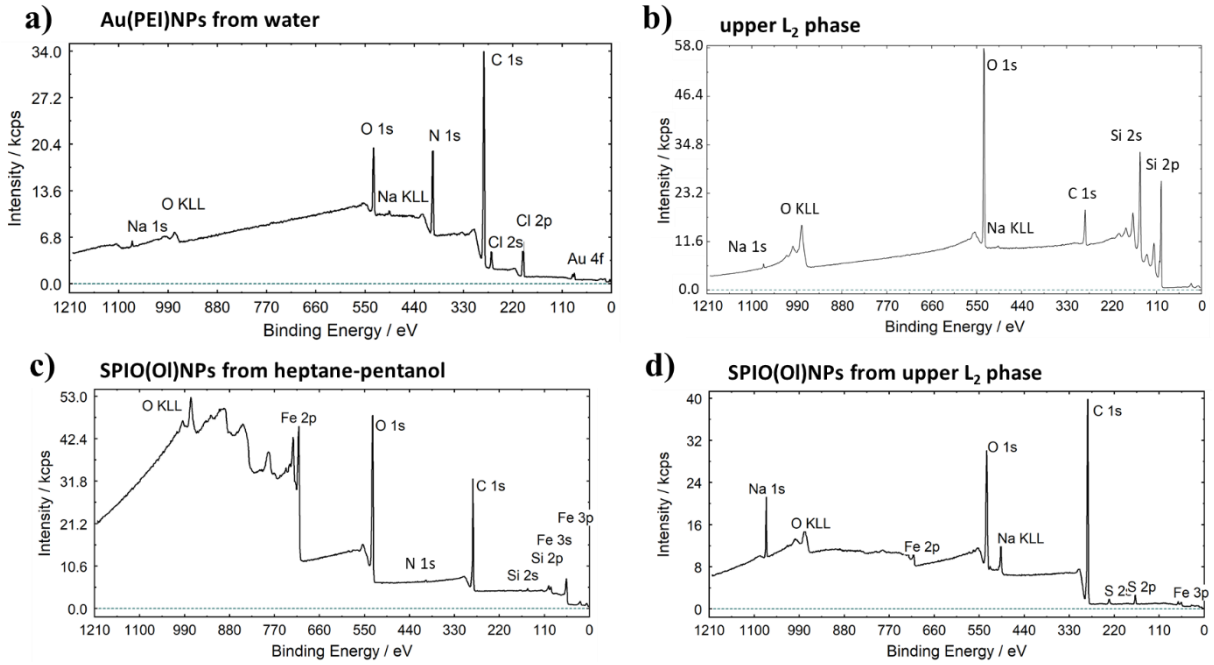

Figure 4.30. XPS spectra after solvent evaporation of nanoparticle and/or microemulsion dispersions: a) Au(PEI)NPs in water; b) remaining compounds from the upper L_2 phase; c) SPIO(Ol)NPs in oil solvent; d) SPIO(Ol)NPs and remaining compounds from the upper L_2 phase. (Adapted with permission from *Langmuir* 2021, *37, 8876-8885*, Copyright 2021, American Chemical Society)

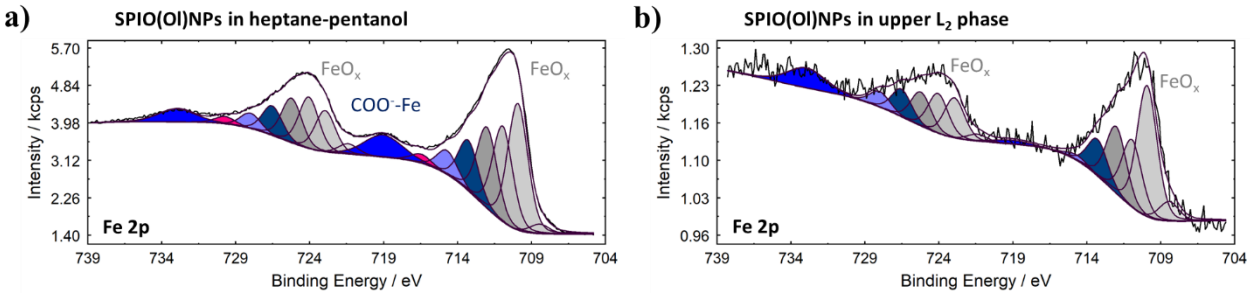

Figure 4.31. XPS spectra comparison between deconvoluted Fe 2p signals of SPIO(Ol)NPs from dispersions after solvent evaporation: a) from only oil solvents, b) from the upper L_2 phase. (Adapted with permission from *Langmuir* 2021, *37, 8876-8885*, Copyright 2021, American Chemical Society)

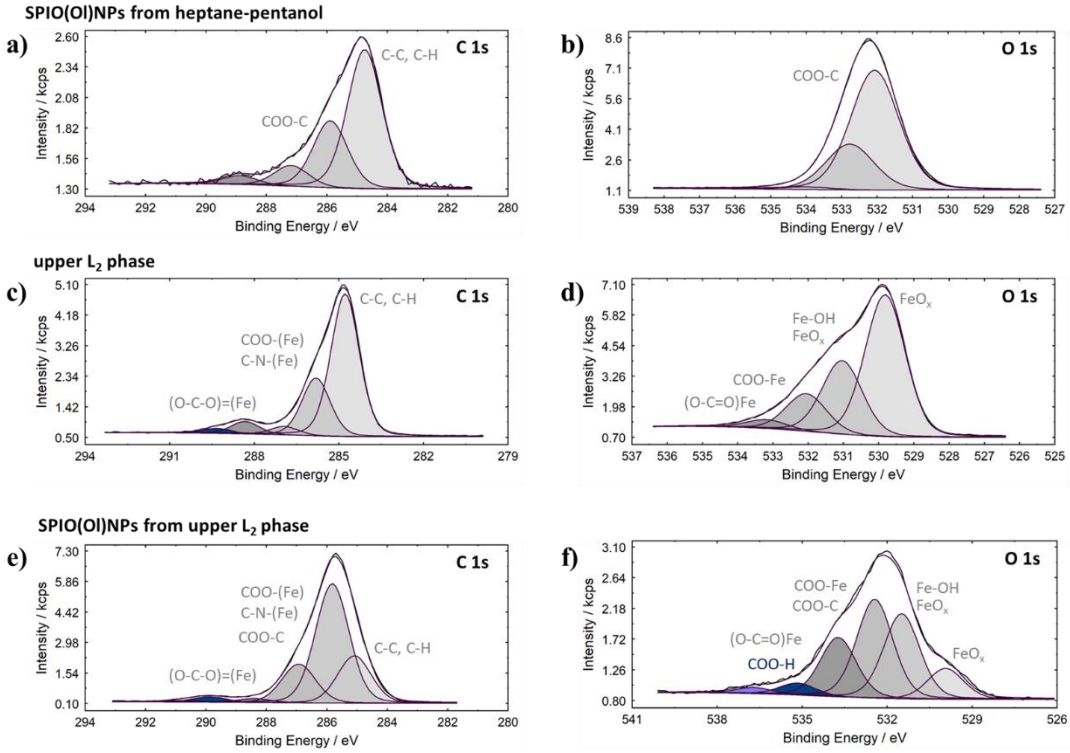

Figure 4.32. XPS spectra comparison between deconvoluted C 1s and O 1s signals of dispersions after solvent evaporation: a, b) SPIO(Ol)NPs from heptane-pentanol; c, d) remaining compounds from the upper L_2 phase; e, f) SPIO(Ol)NPs from the upper L_2 phase. (Adapted with permission from *Langmuir* 2021, *37, 8876-8885*, Copyright 2021, American Chemical Society)

AFM of films after drop-casting or spin-coating

Thin films can be composed of organic and/or inorganic materials arranged over a surface in monolayers or assemblies, with a thickness below the µm range. To prove that the surface assembly of nanoparticles from the upper L_2 phase forms thin films after solvent evaporation, AFM was performed to measure the resulting thickness (**Figure 4.33**). The surface assembly over silicon wafers could be made either by drop-casting or by spin-coating.

The overall thickness of about 200 nm confirmed the formation of a thin film, if then resulted thicker than expected, especially compared to the tiny dimensions of the single nanoparticles below 10 nm. This suggests that the composition of the films should not be based only on nanoparticles, so that the remaining AOT from the microemulsion phase should play a role in the organization of these structures. Note that samples from drop-casting of the isotropic L_2 phase (without phase separation) containing SPIO(Ol)NPs and Au(PEI)NPs could not be visualized by TEM due to a high background contrast, which could be attributed to the formation of thicker films. Additionally, no significant differences in the thickness were observed when the films were formed by simple drop-casting or by spin-coating. For a more precise characterization of the thin film properties, ellipsometry could be also performed.

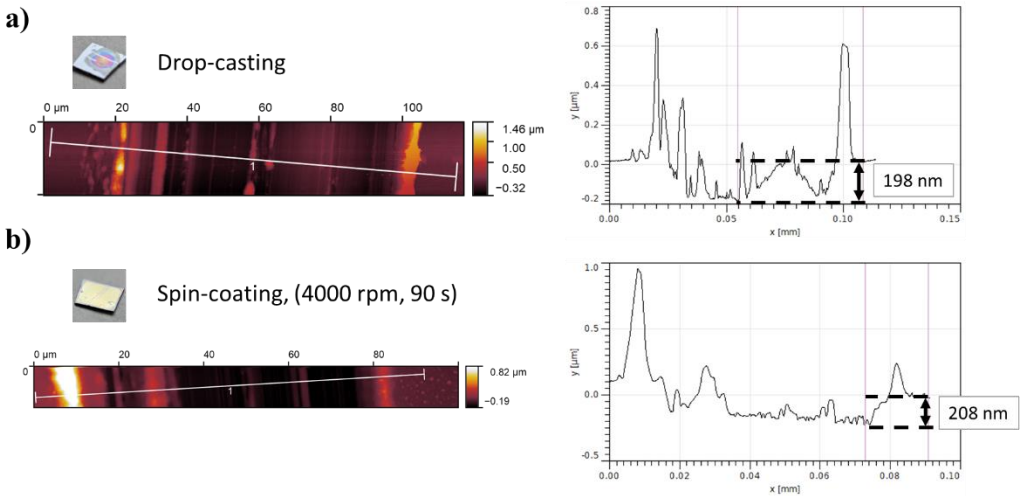

Figure 4.33. AFM measurements performed over a cross-section of nanoparticle films over silicon wafers, from the upper L_2 phase containing SPIO(Ol)NPs and Au(PEI)NPs, with heptane-pentanol as oil solvents, at 30 wt.% aq. content: a) film formed by drop-casting; b) film formed by spin-coating at 4000 rpm under vacuum.

SEM of films after drop-casting or spin-coating

The thin films formed by drop-casting or spin-coating over silicon wafers were also characterized by SEM for the corresponding visualization of the assembly profiles. Equivalent structures were observed in SEM on a silicon wafer as those visualized by TEM on a microscope grid (**Figure 4.34**). However, the morphology of the filament networks changed considerably when the films were made by spin-coating. Possible optimization of the spin-coating for retaining the original morphology of the assemblies could be based on the reduction of the spinning velocity or on a temporal separation between the addition of the dispersion and the spinning of the substrate.

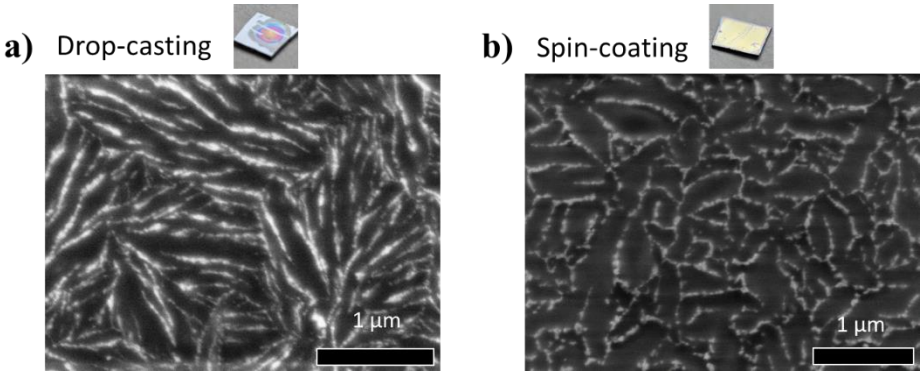

Figure 4.34. SEM micrographs of nanoparticle films over silicon wafers, from the upper L_2 phase containing SPIO(Ol)NPs and Au(PEI)NPs, with heptane-pentanol as oil solvents, at 30 wt.% aq. content: a) film formed by drop-casting; b) film formed by spin-coating at 4000 rpm under vacuum.

Conclusions about the surface assembly from the upper L_2 phase of WPII systems

From the previous characterization results regarding the assembly of nanoparticles from reverse microemulsions in the upper phase of a WPII system, a plausible interpretation could be provided. In the processes involved, a nanoparticle hetero-clustering and a droplet elongation were proved in the L_2 phase. After solvent evaporation, nanoparticle ordering effects and a modulation of the patterns upon water content were observed. A synergistic effect from combining both oleyl-capped nanoparticles and PEI-stabilized nanoparticles were found again. Moreover, the nanostructures arrangements within a thicker film than the nanoparticles size indicated the presence of a remaining matrix, likely from close-packed AOT and water.

The information regarding a clustering of different nanoparticles was provided by UV-Vis absorption, SAXS, and DLS. Especially the interpretation of the SAXS spectra offered a detailed description about the nanoparticle interactions and clustering effects with different combination of nanoparticles (**Figure 4.17**). The red-shift of the LSPR signal of Au(PEI)NPs, by UV-Vis absorption (**Figure 4.14**) and the larger hydrodynamic sizes in the upper L_2 phases than those from the individual nanoparticles (**Figures 4.18, 4.19**) supported the interpretation of a controlled aggregation when the Au(PEI)NPs were incorporated. Similar clustering effects were found in other dispersions of gold nanoparticles. [191,192] For the formation of these heteroclusters, a combination of attractive electrostatic and hydrophobic interactions should be considered (**Scheme 4.3-a**). The electrostatic interactions, leading to Au(PEI)NP destabilization, would occur between the positively-charged PEI and the negatively charged sulfonate head groups of AOT head groups. The hydrophobic interdigitations should be formed with the surfactant tails and the oleyl-capping ligands of the oil-dispersible nanoparticles.

The elongation of microemulsion droplets could be visualized by cryo-SEM at different times of phase-separation (**Figure 4.20**). Elongated droplets were also observed in presence of oleyl-capped nanoparticles, if then the shape-inducing effect was enhanced in combination with PEI-stabilized nanoparticles. This unidirectional growth should be based on different rigidities of the surfactant film of interacting microemulsions (**Scheme 4.3-b**), so that nanoparticles would hinder the approach of additional droplet on the sides in which they are assisting a droplet inter-connection at the water-oil interface. Thus, the growth by incorporation of further droplets should be restricted towards the opposite ends. Similar processes were attributed to the template synthesis of barite nanofilaments. [199] The anisotropic droplet morphologies could be also related to very low surface tension, as the curvature can be partially supressed [8]

The two aforementioned processes should contribute to the resulting nanostructured filament networks after solvent evaporation of the upper L_2 phase. The formation of

heteroclusters from destabilized PEI-coated nanoparticles combined with oleyl-capped nanoparticles (**Figure 4.17-a**) should be relevant for the subsequent self-assembly. However, not all nanoparticles are forming heteroclusters, so that the remaining free nanoparticles should rather contribute to the shape-induced elongation of the microemulsions (**Figure 4.17-b**). The incorporation of Au(PEI)NPs in the upper L_2 phase was also found to depend on the aqueous content, the equilibration time and the partitioning of phases (**Figures 4.13, 4.14, 4.25**). At higher aqueous contents, a general trend of increasing Au(PEI)NPs concentration upon dilution with aqueous phase of the WPII mixture was found. The larger aqueous content also contributed to form more dense patterns of shorter filaments (**Figure 4.25**). This could be attributed to a higher presence of heteroclusters, which would restrict the unidirectional droplet growth. Upon evaporation of the solvents, a transition of the elongated droplets to packed arrangements with periodic inter-particle distances (**Figure 4.29-b**), should also occur in similarity to lyotropic liquid crystalline phases (**Figure 4.22**). Related patterning and periodicity effects were observed from the modulation of nanoparticle interactions which can form close-packed arrangements by interdigitation of their capping ligands and surfactant tails or other free ligands. [128,204,205].

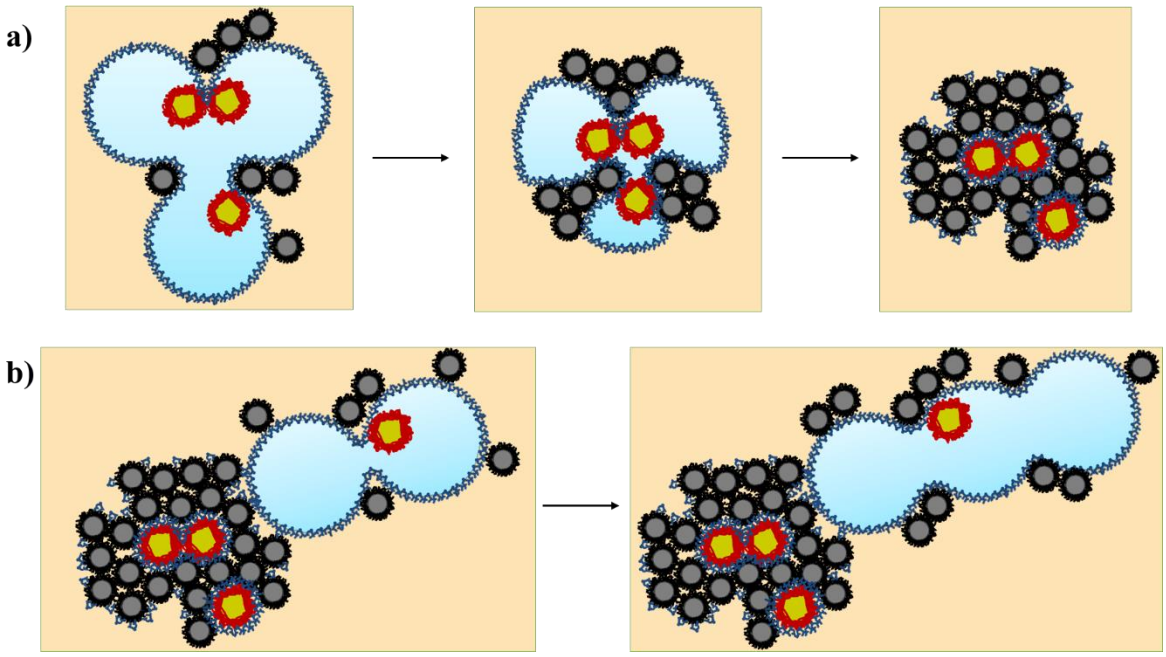

Scheme 4.3. Proposed interpretation about template assembly of oleyl-capped and PEI-stabilized nanoparticles from the upper L_2 phase of WPII systems with AOT as surfactant: a) heteroclustering of nanoparticles; b) droplet elongation, limited by the presence of nanoparticle heteroclusters. (Adapted with permission from *Langmuir* 2021, *37, 8876-8885*, Copyright 2021, American Chemical Society)

Modifications of the nanostructured thin films

The assembly of nanoparticles in filament networks from reverse microemulsions over a surface has proved a new way of templating effects for these colloidal dispersions. However, possible applications are yet to be proven. As a first idea, transparent and conductive thin films should be of special interest for applications related to optoelectronic processes. The optical and electrical properties of these nanostructured films should be related to the nanoparticle compositions, the inter-particle distances and the surrounding compounds. Generally, the electrical properties of a material can be classified according to the values of conductivity or resistivity: conductor materials should have resistivities below 10^{-3} Ω·m, semiconductor materials are of very variable resistivity and (electrical) insulator materials have resistivities above 10^{8} Ω·m.

On a first test, the resistivity of the nanostructured films of SPIO(Ol)NPs and Au(PEI)NPs on surface-modified ITO slides was measured according to the four-point probe set-up. Although the measured local intensity -between the inner contact points- was proportional to the applied voltage -on the outer contact points-, the resulting resistivity was too high, in the range of 10^{10} Ω·m. Nevertheless, a certain increase of the measured intensity upon time of the applied voltage, and the presence of residual intensity current when the external voltage is removed could be attributed as a *condensator-effect*. Similar electronic effects have been demonstrated for nanoparticle assemblies whose inter-particle distance are short enough, based on charge transport by tunnelling effects. [128] Another way to measure the resistance was by directly on interdigitated electrodes whose contact should be closed by the presence of an incorporated material, for this case the nanostructured films. The measured resistance was however too high again, including on films of Ag(Ol)NPs, with a range above 10^{10} Ω.

To improve the electrical properties, sintering tests were also applied to nanostructured films. The melting temperature of nanoparticles is generally lowered from that of the bulk material, resulting in partial fusion of sintering at temperatures lower than the melting point of the bulk material. Vacuum heating of samples is also used to remove remaining organic components, either by evaporation or by decomposition. [128] However, the resulting resistances of the surface-modified ITOs or interdigitated electrodes were again too high.

Visualization by TEM also showed that placing the samples were in a vacuum oven at temperatures above 150 °C resulted in the total degradation of the nanostructured films. The aspect of the films was slightly improved when the heating was made by increasing gradually the temperature in defined steps till temperatures not higher than 120 °C (**Figure 4.35**).

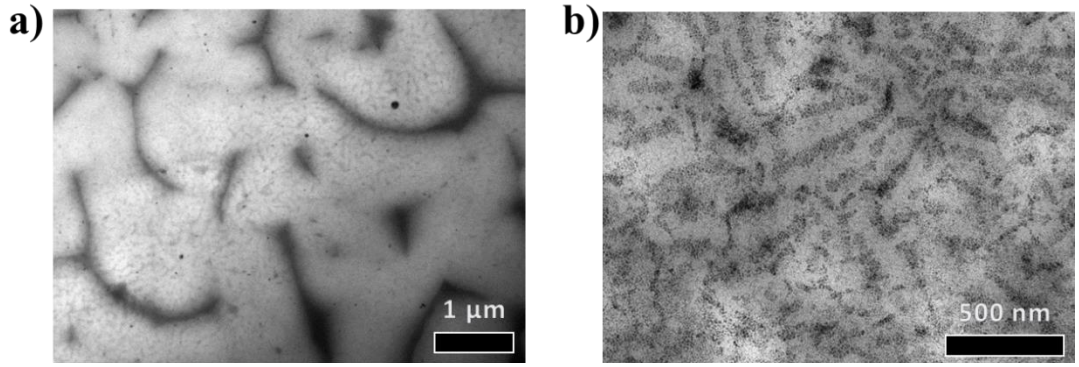

Figure 4.35. TEM micrographs of nanostructures from drop-casting of the upper L_2 phase of WPII mixture after one day of phase equilibration, with SPIO(Ol)NPs and Au(PEI)NPs in heptane-pentanol as oil solvents, placed afterwards in a vacuum oven for about 1-2 h: a) 120 °C; b) 90 °C.

Another strategy to improve the electrical properties of the nanostructured films was based on the substitution of the SPIO(Ol)NPs by Ag(Ol)NPs. The pattern of filament networks could be preserved in presence of Ag(Ol)NPs (**Figures 4.28, 4.36**), and lower sintering temperatures can be applied. However, the original nanostructures were also altered significantly, showing aggregation and polydispersity effects (**Figure 4.36**). Therefore, other possibilities should be considered regarding the optimizations of the optoelectronic properties of these nanoparticle films, to have plausible applications. Optimization possibilities include the use of other solvent components, nanoparticles with different compositions while keeping similar surface functionalization, in-situ polymerization, etc.

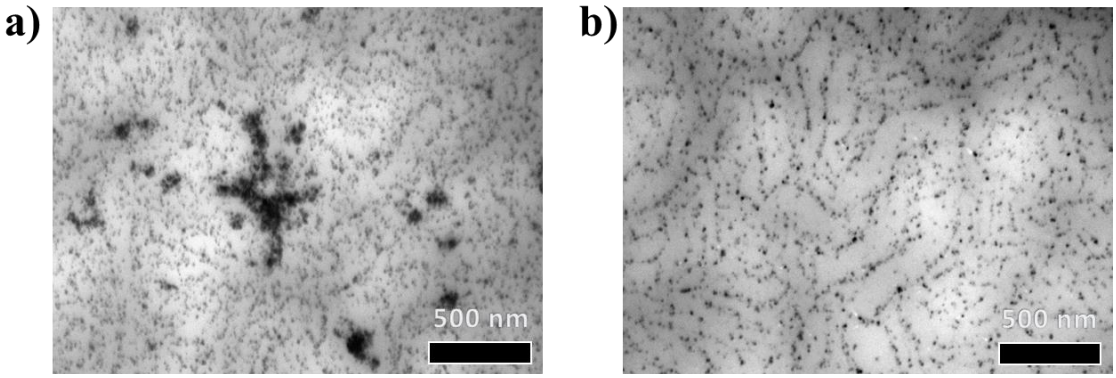

Figure 4.36. TEM micrographs of nanostructures from drop-casting of the upper L_2 phase of WPII mixture after one day of phase equilibration with 30 wt.% aq. content, using heptane-pentanol as oil solvents, placed afterwards in a vacuum oven at 35 °C during 5 days, with different nanoparticle combinations: a) Ag(Ol)NPs and Au(PEI)NPs, b) Ag(Ol)NPs with SPIO(Ol)NPs in 1:1 ratio and Au(PEI)NPs.

4.4 Compartmentalized nanostructures from magnetic heterocoagulates

*This section is part of the following manuscript:

- "Nanostructured assembly of magnetic and plasmonic nanoparticles transferred from AOT Winsor phases to oil-in-water functional dispersions", *ChemNanoMat* ***2022***, *e202200353 (in press)*.

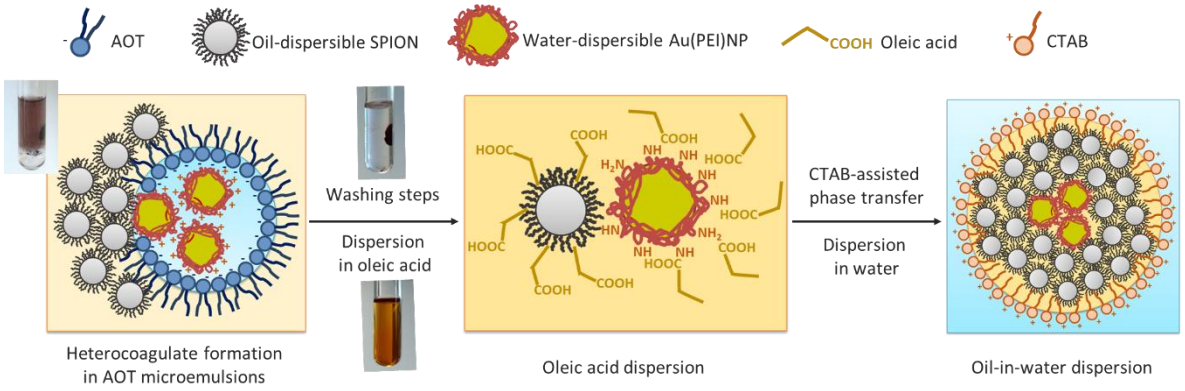

Scheme 4.4. Proposed nanoparticle interactions for the formation of the magnetic heterocoagulate, and then for the phase-transfer into oleic acid and to oil-in-water nanostructured dispersions. (Adapted from *ChemNanoMat* 2022, *e202200353*)

When phase separation occurs at higher AOT content, the increase in viscosity of the lower phase leads to gel-like formation. The incorporation of both magnetic oleyl-capped and PEI-stabilized nanoparticles in this composition mixture resulted in the formation of a coagulate which was responsive to an external magnet (**Figure 4.37-a**). This magnetic-responsiveness was also useful to separate and wash the heterocoagulate from the dispersion. Generally, the incorporation of substances from a dispersion to magnetic-responsive conjugates has been applied for separation processes. In our case, it was of interest to investigate the formation of interfacially-assembled Au(PEI)NP-SPIO(Ol)NP structures. The formation of this heterocoagulate was made either at room temperature or by heating above 50 °C for 30 min before phase-separation occurred. Hexane-pentanol or heptane-pentanol could be used as oil solvents, if then heptane is preferred to hexane. Afterwards, a combination of non-polar solvents (like heptane or hexane), alternating with polar solvents like ethanol, was used to remove remaining components of the original mixture.

FTIR was confirming the presence of both SPIO(Ol)NPs and Au(PEI)NPs in the magnetic heterocoagulate, according to the respective functional groups (**Figure 4.37-b**). Thus, the characteristic Fe-O stretching band at around 590 cm^{-1} from the SPIO(Ol)NPs [113,206] and the N-H stretching band over 3300 cm^{-1} from the Au(PEI)NPs [207] were found in the spectrum of the heterocoagulate after solvent evaporation.

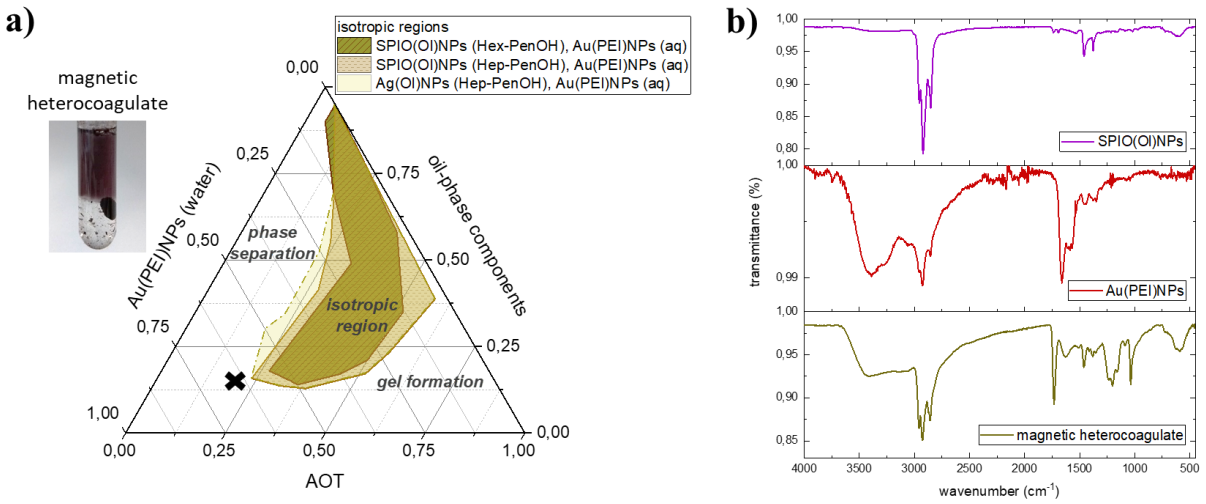

Figure 4.37. a) Partial phase diagrams of the quasi-ternary mixtures, in absence and presence of 0.5 wt.% SPIO(Ol)NPs or Ag(Ol)NPs in hexane-pentanol or heptane-pentanol, and 0.3 wt.% Au(PEI)NPs in water; b) FTIR spectra. (Adapted from *ChemNanoMat* 2022, *e202200353*)

To afford functional dispersions from these heterocoagulates, a stepwise work-up of phase-transfer processes was followed. The main processes involved dispersion in carboxylic acids of long alkyl chains, and oil-in-water transfer assisted by an auxiliary surfactant and in certain ethanol-water ratio (**Scheme 4.4**).

Heterocoagulates in long-chained carboxylic acids

The dispersibility of this heterocoagulate in suitable solvents resulted however of a challenge. Only long-chain carboxylic acids, namely oleic, octanoic and hexanoic acid, were affording optically clear, brown dispersions. This is likely attributed to the possibility of these solvents to form interactions with both types of particles. Thus, there should be hydrophobic interactions with the oleyl-caped nanoparticles and electrostatic interactions with the PEI-coated nanoparticles (**Scheme 4.4**).

UV-Vis-absorption profiles of the heterocoagulate dispersions in carboxylic acids were showing a characteristic peak with a maximum at around 390 nm for oleic acid, which shifts to lower wavelengths for carboxylic acids of shorter chain (**Figure 4.38**). Similar absorption peaks were also found for the respective dispersions containing the individual nanoparticles in the carboxylic acids. The SPIO(Ol)NPs were also showing the aforementioned peak when

dispersed in oleic acid. For the case of Au(PEI)NPs, the characteristic LSPR peak remained at about 520 nm while the shoulder in shorter wavelengths evolved into a second defined peak in the proximity to 390 nm. When Ag(Ol)NPs are partially substituting a fourth part of the SPIO(Ol)NPs, an appearance of a shoulder of around 400 to 500 nm besides the maximum at 390 nm is observed (**Figure 4.38-a**). For the case of the magnetic heterocoagulates formed at room temperature (r.t.), the absence of the plasmon band can be attributed to a majoritarian presence of oleyl-capped nanoparticles or to their masking effect in respect to the minor amounts of Au(PEI)NPs. Moreover, when the heterocoagulates formed at r.t. were dispersed in octanoic and hexanoic acid, the absorption maximum shift to 330 and 300 nm, respectively (**Figure 4.38-b**).

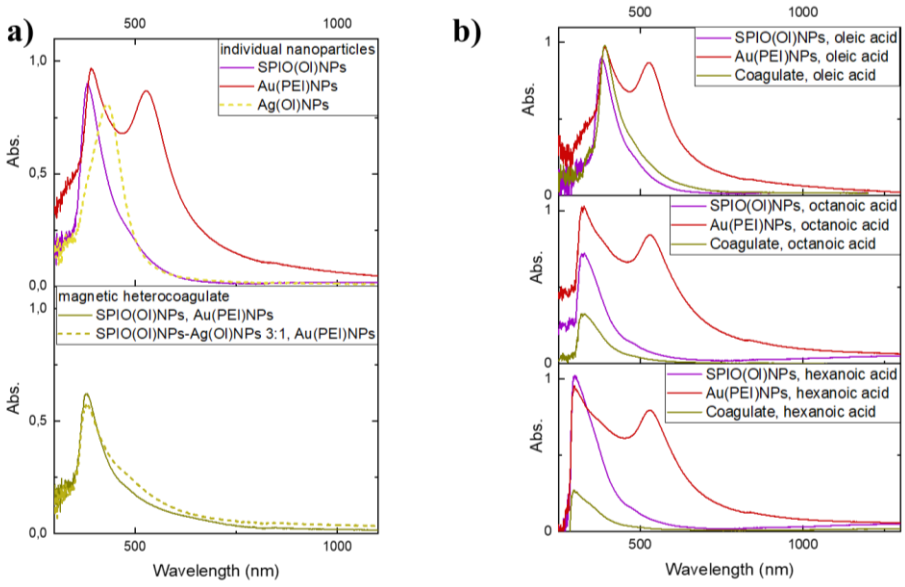

Figure 4.38. UV-Vis absorption spectra of nanoparticle dispersions in carboxylic acids: a) oleic acid containing the individual SPIO(Ol)NPs, Ag(Ol)NPs or Au(PEI)NPs (top panel) and the heterocoagulates formed at r.t. (bottom panel); b) oleic, octanoic and hexanoic acid containing the heterocoagulates from SPIO(Ol)NPs and Au(PEI)NPs formed at r.t. (Adapted from *ChemNanoMat* 2022, *e202200353*)

When the heterocoagulates were initially formed under heating, the UV-Vis absorption of the respective dispersions in oleic acid show increased intensity and the appearance of a second band at around 400 to 600 nm (**Figure 4.39-a**). This enhancement can be attributed to a higher incorporation of nanoparticles, specially from Au(PEI)NPs besides the oleyl-capped nanoparticles. The presence of nanoparticle clusters was also suggested by the respective DLS plots of the heterocoagulate dispersions in oleic acid (**Figure 4.39-b**, **Table 4.4**), as larger hydrodynamic sizes were obtained for the heterocoagulate dispersions than for the respective dispersions containing the individual nanoparticles.

Nevertheless, TEM micrographs could not provide any good visualization of the resulting nanostructures (**Figure 4.39-c**), as the carboxylic acids cannot be completely removed under mild conditions. This implied the necessity of finding a suitable dispersing medium, with the preference of aqueous systems.

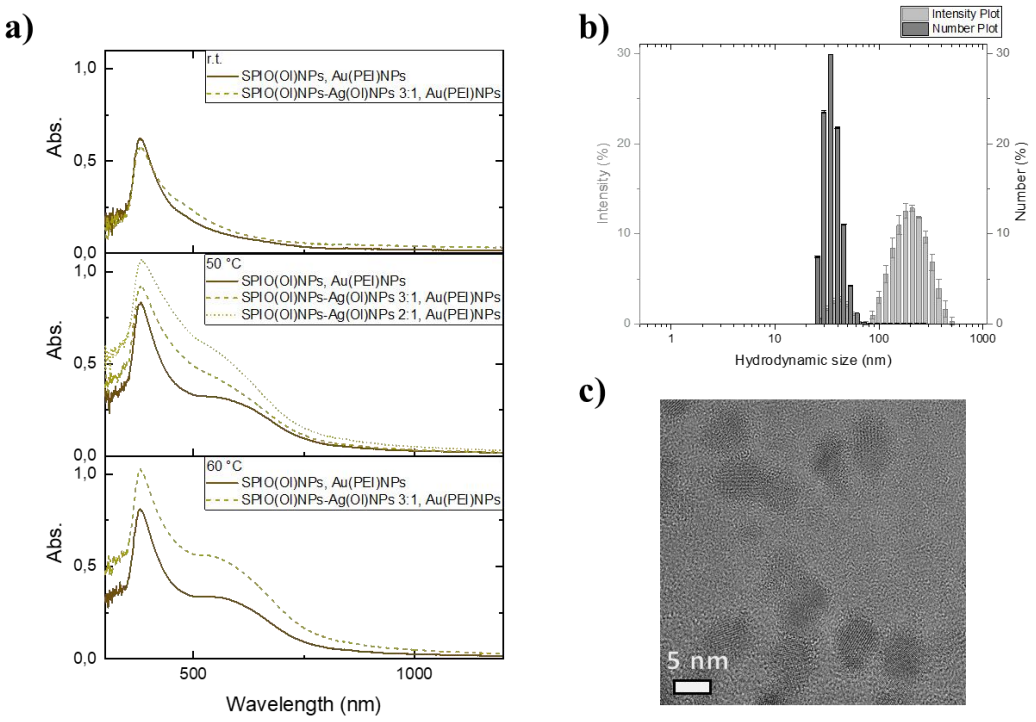

Figure 4.39. Characterization of heterocoagulate dispersions in oleic acid, formed at r.t., 50 °C or 60 °C, with partial substitution of SPIO(Ol)NPs by Ag(Ol)NPs: a) UV-Vis absorption spectra of the resulting heterocoagulates; b) DLS intensity and number plots of the heterocoagulate formed from SPIO(Ol)NPs and Au(PEI)NPs at r.t.; c) HRTEM of the resulting nanostructures from SPIO(Ol)NPs and Au(PEI)NPs at r.t. (Adapted from *ChemNanoMat* 2022, *e202200353*)

Phase-transfer of heterocoagulates in water dispersions

The oleic acid dispersions could be transferred into water by mediation of an auxiliary surfactant with an adequate volume ratio of ethanol in the water mixture (**Scheme 4.5**). This is based on the formation bilayers between the hydrocarbon chains of oleyl groups and the alkyl chains of the auxiliary surfactant, as described in a proposed report to stabilize hydrophobic nanoparticles in water. [208] A minimum proportion of ethanol was needed to avoid phase-separation between oleic acid and water. Tested surfactants included CTAB, SDS and Brij 35, and the water-ethanol volume ratio could be 1:1 or 1:2, if then higher proportion of ethanol was preferred. Moreover, an optimal volume ratio between dispersions of oleic acid and water-ethanol was found optimal up to 2:15. Thus, the resulting dispersions were washed by centrifugation and removal of supernatant, and the redispersion of the sediment in water afforded the oil-in-water heterocoagulate dispersions.

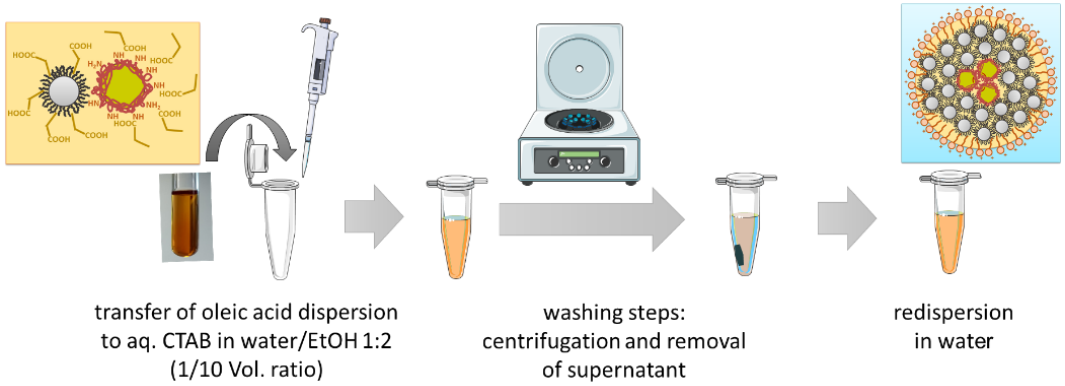

Scheme 4.5. Stepwise phase-transfer of the heterocoagulate dispersions from oleic acid to water. (Adapted from *ChemNanoMat* 2022, *e202200353*)

Oil-in-water heterocoagulate dispersions in the water medium

UV-Vis absorption was performed again on the resulting aqueous dispersions from the phase-transfer. Generally, the characteristic signal of about 390 nm in the oleic acid dispersions were not observed anymore, if then similar absorption band profiles in the 300-600 nm range can be correlated with those of the respective oleic acid dispersions (**Figure 4.40-a**). Additionally, the overall absorption behaviour, including a small peak of about 840 nm, can be correlated to the respective dispersions of oleic acid with CTAB and water (**Figure 4.40-b**). Thus, a possible interpretation could be based on a masking effect of the surfactant-stabilized oil shell. Similar profiles could be obtained with other auxiliary surfactants like SDS, if then the absorption intensity was lowered (**Figure 4.40-c**), indicating that a less efficient phase-transfer resulted in lower concentration of heterocoagulate.

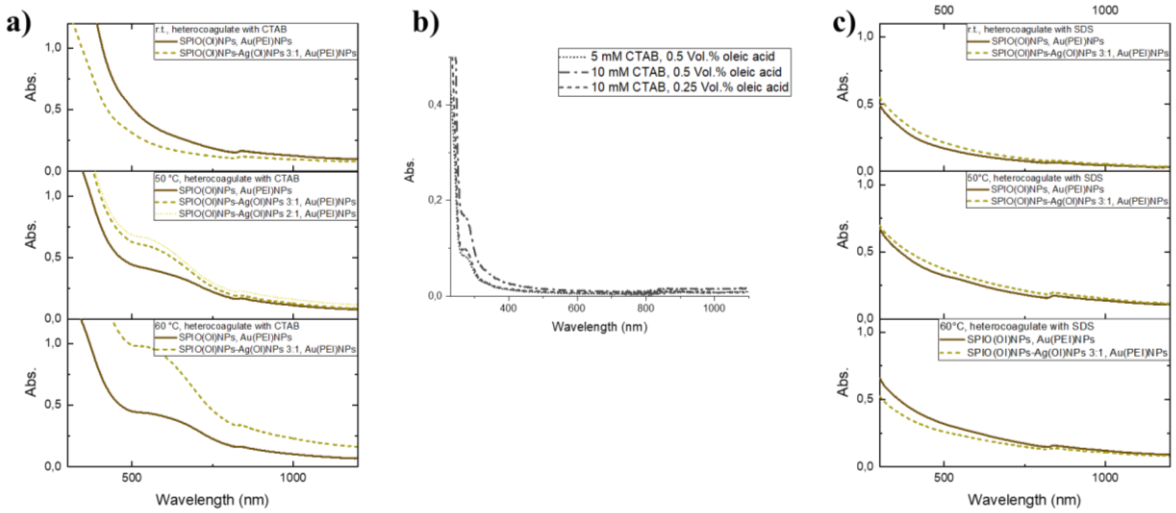

Figure 4.40. UV-Vis absorption of oil-in-water dispersions, being the heterocoagulates initially formed at r.t., 50 °C or 60 °C, with partial substitution of SPIO(Ol)NPs by Ag(Ol)NPs: a) heterocoagulate dispersions stabilized with CTAB; b) oleic acid with CTAB dispersed in water; c) heterocoagulate dispersions stabilized by SDS. (Adapted from *ChemNanoMat* 2022, *e202200353*)

DLS plots of the heterocoagulate dispersions in water suggested the presence of larger nanostructures entities than the individual nanoparticles (**Figure 4.41**, **Table 4.4**). Generally, hydrodynamic sizes of about 200 nm were obtained, larger than those from the dispersions in oleic acid. This enlargement of size occurs especially when the heterocoagulates were initially formed by heating above 50 °C. The hydrodynamic sizes of a given heterocoagulate, formed under the same conditions, were also larger for SDS-stabilized dispersions than for the dispersions stabilized by CTAB. No significant effect on the nanostructures size resulted by the incorporation of Ag(Ol)NPs.

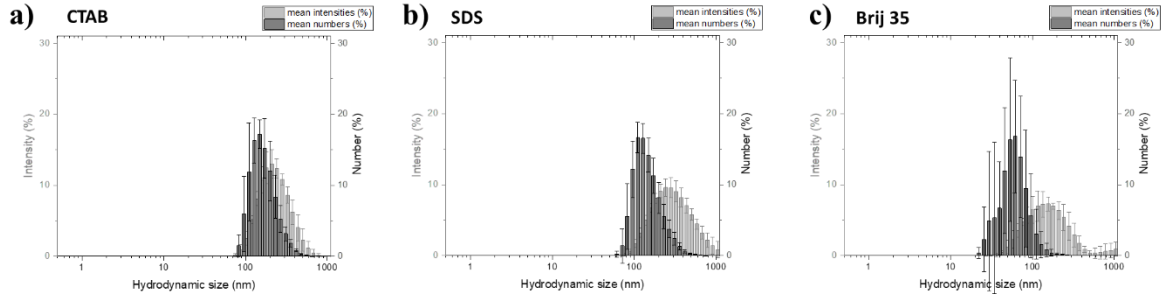

Figure 4.41. DLS plots according to the intensity % and number % of the heterocoagulate dispersions formed under initial heating from SPIO(Ol)NPs and Au(PEI)NPs, and stabilized in water by different auxiliary surfactants: a) CTAB, b) SDS, c) Brij 35. (Adapted from *ChemNanoMat* 2022, *e202200353*)

Although similar features were observed from UV-Vis absorption and DLS, the Zeta potential values, related to the electrostatic stabilization, differed considerably for each auxiliary surfactant (**Figure 4.42**, **Table 4.4**). Thus, a positive Zeta potential was observed for nanostructures stabilized by CTAB while negative Zeta potentials were observed when the nanostructures were stabilized by SDS or Brij 35. This confirms the location of the surfactant head groups and the carboxylate groups of oleic acid at an oil-water interface (**Scheme 4.4**).

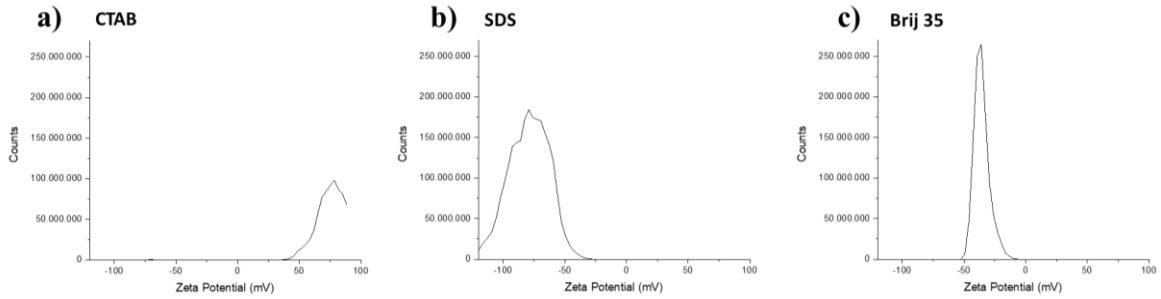

Figure 4.42. Zeta potential plots of the heterocoagulate dispersions formed under initial heating from SPIO(Ol)NPs and Au(PEI)NPs, and stabilized in water by different auxiliary surfactants: a) CTAB, b) SDS, c) Brij 35. (Adapted from *ChemNanoMat* 2022, *e202200353*)

Table. 4.4. Average values in DLS and ζ of the heterocoagulate dispersions in oleic acid or in water (stabilized by CTAB or by SDS), formed at different temperatures, from SPIO(Ol)NPs and Au(PEI)NPs, and being SPIO(Ol)NPs partly substituted by Ag(Ol)NPs. (Adapted from *ChemNanoMat* 2022, *e202200353*)

		oleic acid dispersion		oil-water dispersion, CTAB-stabilized		oil-water dispersion, SDS-stabilized	
		d_h, DLS /nm	ζ /mV	d_h, DLS /nm	ζ /mV	d_h, DLS /nm	ζ /mV
r.t.	SPIO(Ol)NPs + Au(PEI)NPs	232 ± 153	-	197 ± 70	+61 ± 6	227 ± 95	-40 ± 15
	SPIO(Ol)NPs-Ag(Ol)NPs 3:1 + Au(PEI)NPs	377 ±156	-	196 ± 73	+61 ± 7	224 ± 82	-59 ± 10
50 °C	SPIO(Ol)NPs + Au(PEI)NPs	91 ± 52	-	238 ± 90	+78 ± 8	348 ± 194	-78 ± 7
	SPIO(Ol)NPs-Ag(Ol)NPs 3:1 + Au(PEI)NPs	121 ± 41	-	203 ± 103	+58 ± 10	370 ±221	-70 ± 13
60 °C	SPIO(Ol)NPs + Au(PEI)NPs	186 ± 75	-	227 ± 129	+66 ± 11	266 ±108	-44 ± 15
	SPIO(Ol)NPs-Ag(Ol)NPs 3:1 + Au(PEI)NPs	142 ± 59	-	238 ± 147	+68 ± 9	310 ±131	-65 ± 9

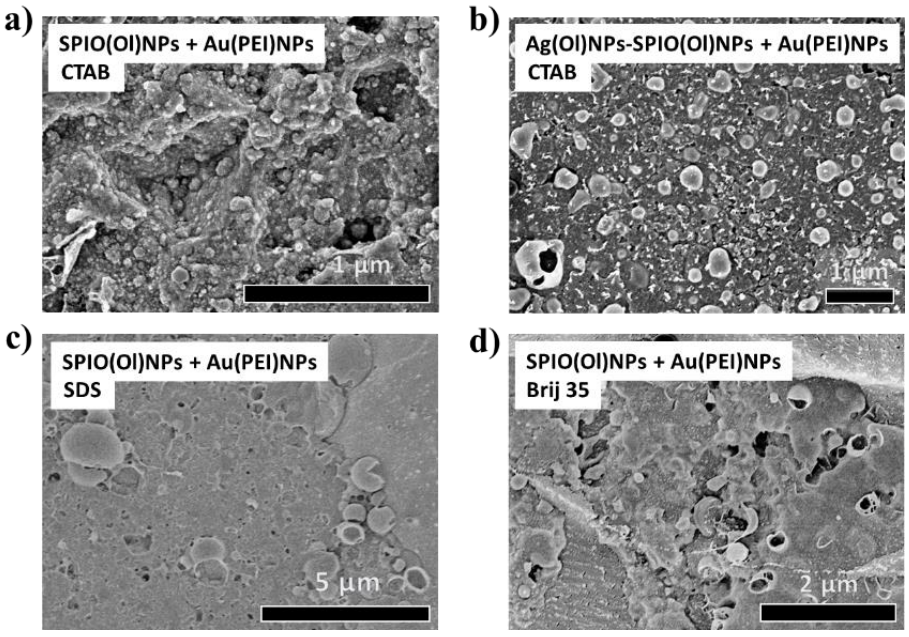

Figure 4.43. Cryo-SEM micrographs of the oil-in-water heterocoagulate dispersions formed under initial heating from SPIO(Ol)NPs and Au(PEI)NPs and stabilized in water by different auxiliary surfactants: a) formed at 50°C, stabilized by CTAB; b) formed at 50°C with SPIO(Ol)NPs-Ag(Ol)NPs 3:1, stabilized by CTAB; c) formed at 60°C, stabilized by SDS; d) formed at 60°C, stabilized by Brij 35. (Adapted from *ChemNanoMat* 2022, *e202200353*)

Visualization of these oil-in-water dispersions without solvent evaporation could be provided by cryo-SEM (**Figure 4.43**). The respective micrographs could support the DLS results regarding the presence of 200 nm sized droplets. Additionally, the contrast in the droplets interface indicates that the nanoparticles should be incorporated within. Note that the contrast can also depend on the concentration of heterocoagulate and oleic acid in the dispersion.

Oil-in-water heterocoagulate dispersions after solvent evaporation

TEM micrographs were indicating the presence of nanoparticle composites after evaporation of the solvents (**Figures 4.44, 4.45, 4.46, 4.47**). Therefore, it is supported that there should be agglomerated nanoparticle structures within oil-in-water droplets (**Scheme 4.4**). In these nanostructures, Au(PEI)NP domains of higher contrast are engulfed by a matrix of oleyl-capped nanoparticles, which should contribute to their stabilization. Especially when the heterocoagulates were formed from the initial AOT dispersion under heating, better-defined and compartmentalized nanostructures can be observed (**Figure 4.44**). Similar SPIO(Ol)NP-Au(PEI)NP conglomerates had been previously obtained from Pickering emulsions stabilized by a Pluronic derivative, [151] if then this current approach improved the structural organization. The sizes of these conglomerates are in most cases of similar dimensions than those observed by DLS and cryo-SEM before solvent evaporation (**Figures 4.41, 4.43**). Thus, the possibility of encapsulation of aqueous nanoparticle domains inside an oil-swollen matrix shell of oil-dispersible nanoparticles, stabilized in water media, is suggested in similarity to layer-by-layer assemblies. [134,135,166] Noteworthy, TEM micrographs from aqueous heterocoagulate dispersions in high concentration could not show defined nanostructures,

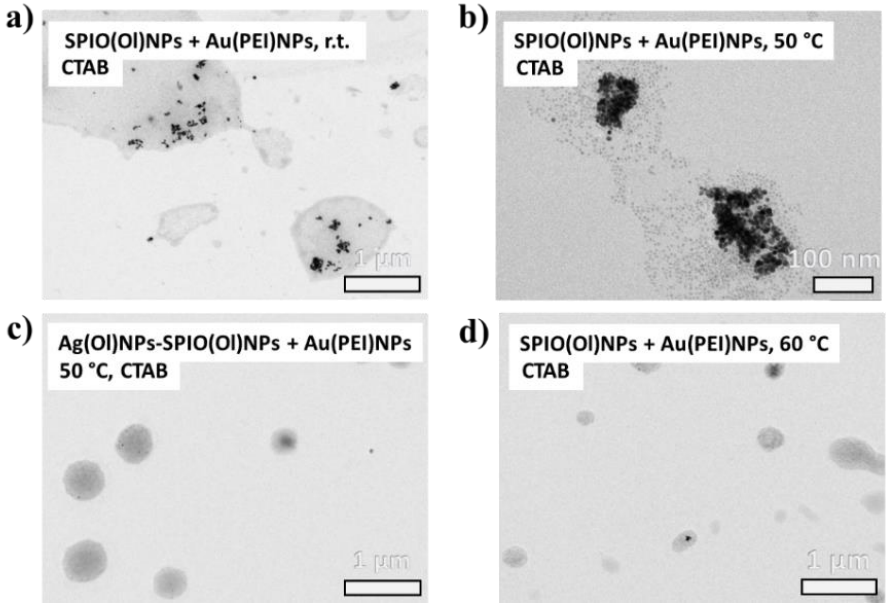

Figure 4.44. TEM micrographs of heterocoagulate dispersions formed from SPIO(Ol)NPs and Au(PEI)NPs and stabilized in water by CTAB, initially formed at different temperatures: a) r.t., b) 50 °C, c) 50 °C with SPIO(Ol)NPs-Ag(Ol)NPs in 3:1 ratio, d) 60 °C. (Adapted from *ChemNanoMat* 2022, *e202200353*)

even though cryo-SEM and DLS were suggesting the presence of oil-in-water droplets of around 200 nm. This could be attributed to coalescence-related phenomena resulting in further agglomeration of the nanostructures, which also proves the soft character of these assemblies. It is also possible that many of these organized structures are not preserved after solvent evaporation.

Additionally, the partial substitution of SPIO(Ol)NPs by Ag(Ol)NPs in the heterocoagulates formed under initial heating, resulted in further better defined nanostructures (**Figures 4.44, 4.45**). Despite of the differences in the UV-Vis absorption profiles (**Figures 4.38-a, 4.39-a**), no significant improvement in the nanostructured organization was appreciated when the heterocoagulate was initially formed at either 50 °C or 60 °C.

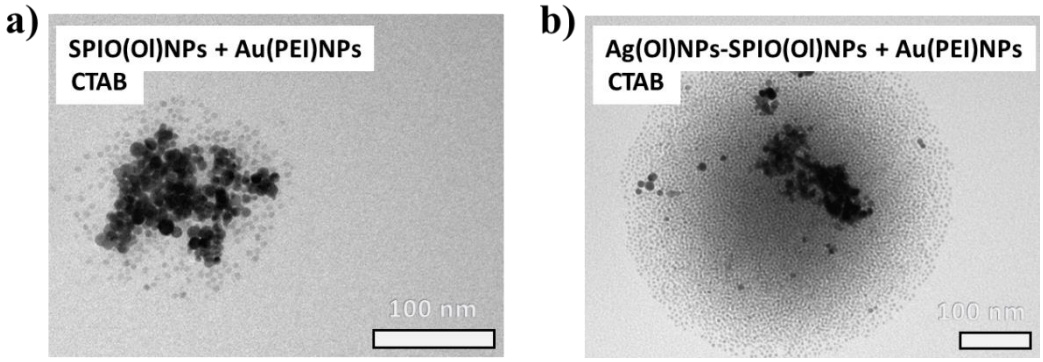

Figure 4.45. TEM micrographs of heterocoagulate dispersions initially formed at 50 °C, from SPIO(Ol)NPs or SPIONs-Ag(Ol)NPs in 3:1 ratio and Au(PEI)NPs, stabilized in water by CTAB as auxiliary surfactant: a) only SPIO(Ol)NPs and Au(PEI)NPs; b) SPIO(Ol)NPs-Ag(Ol)NPs 3:1. (Adapted from *ChemNanoMat* 2022, *e202200353*)

The formation of compartmentalized nanostructures was also possible by the mediation of other surfactants and polymer derivatives (**Figure 4.46**). However, many other irregular structures were also present. Similar interlayering patterns were additionally observed on the nanostructures with Brij 35 or with a thermo-responsive copolymer based on poly(*N,N*-diethylacrylamide) (PDEAA) and poly(2-oleoylethyl methacrylate) (OEMA), previously used in this group [209]. Thus, to get defined nanostructures, suitable auxiliary stabilizers should have an optimal packing of their molecular structures or provide enough steric stabilization. More research is needed regarding conditions such as the proportion between the different types of nanoparticles, the concentration in oleic acid and auxiliary surfactant, and the oil-to-water ratio, which can be different for every type of auxiliary stabilizer.

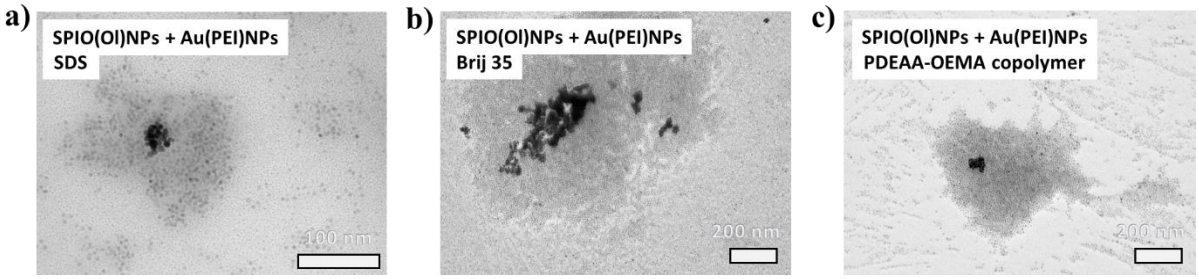

Figure 4.46. TEM micrographs of heterocoagulate dispersions initially formed under heating, from SPIO(Ol)NPs and Au(PEI)NPs, stabilized in water by different auxiliary surfactants: a) 60 °C initial temperature, with SDS as auxiliary surfactant; b) 50 °C, with CTAB; c) 50 °C with thermo-responsive copolymer.

The visualization of older heterocogulate dispersions after several weeks, in the oleic acid or in the water phase, offered additional information about their stability (**Figure 4.47**). Compartmentalized oil-in-water nanostructures were still formed in the aqueous dispersion after one month, if then the Au(PEI)NP domains tend to appear slightly at the external part of the oil matrix (**Figure 4.47-a**). On a different approach, when the heterocoagulate dispersion in oleic acid is transferred to water after one month, the resulting nanostructures show separated Au(PEI)NPs surrounded by the oleyl-capped nanoparticles (**Figure 4.47-b**). Although the resulting nanostructures from an older oleic acid dispersion are not compartmentalized anymore, a better distribution of embedded Au(PEI)NPs in these nanostructures might be afforded. The Zeta Potential values were supressed for the aqueous dispersions after 1 moth, and similar for the phase-transfer of the oleic acid dispersions after one moth. Thus, these hybrid nanostructures can be stable after several weeks, if then significant changes in morphology and surface charges would also occur. Further investigation should be required for a better understanding about these stabilization effects.

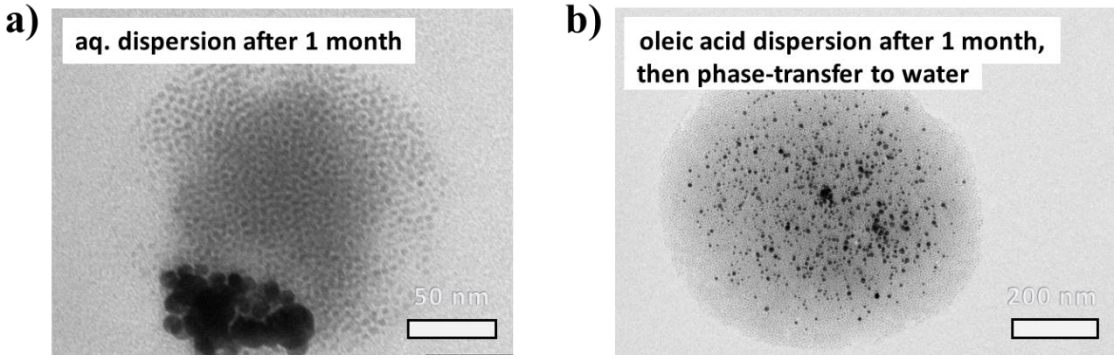

Figure 4.47. TEM micrographs of oil-in-water nanostructures from older heterocoagulate dispersions, containing SPIO(Ol)NPs and Au(PEI)NPs, and stabilized in water by CTAB: a) from diluted aqueous heterocoagulate dispersion after one month; b) from oleic acid dispersion after one moth, then phase-transferred to water.

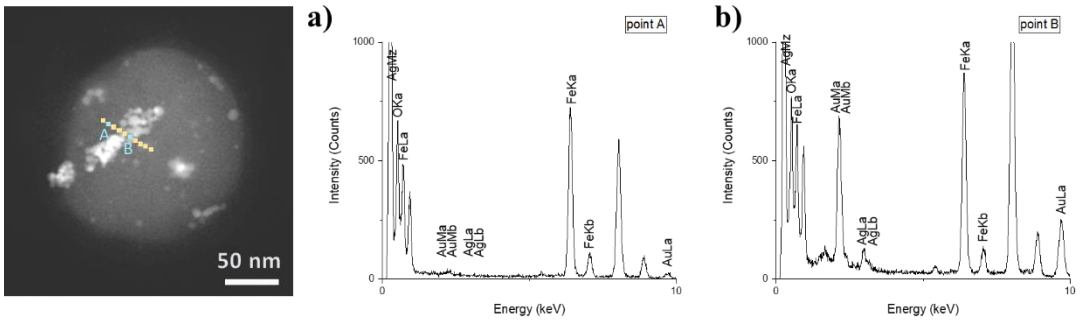

Figure 4.48. HRTEM-STEM micrograph of an heterocoagulate dispersion formed at 60 °C from SPIO(Ol)NPs and Au(PEI)NPs, with SPIO(Ol)NPs partially substituted by Ag(Ol)NPs (SPIONs-Ag(Ol)NPs 3:1 ratio), including EDX spectra corresponding to the marked points. (Adapted from *ChemNanoMat* 2022, *e202200353*)

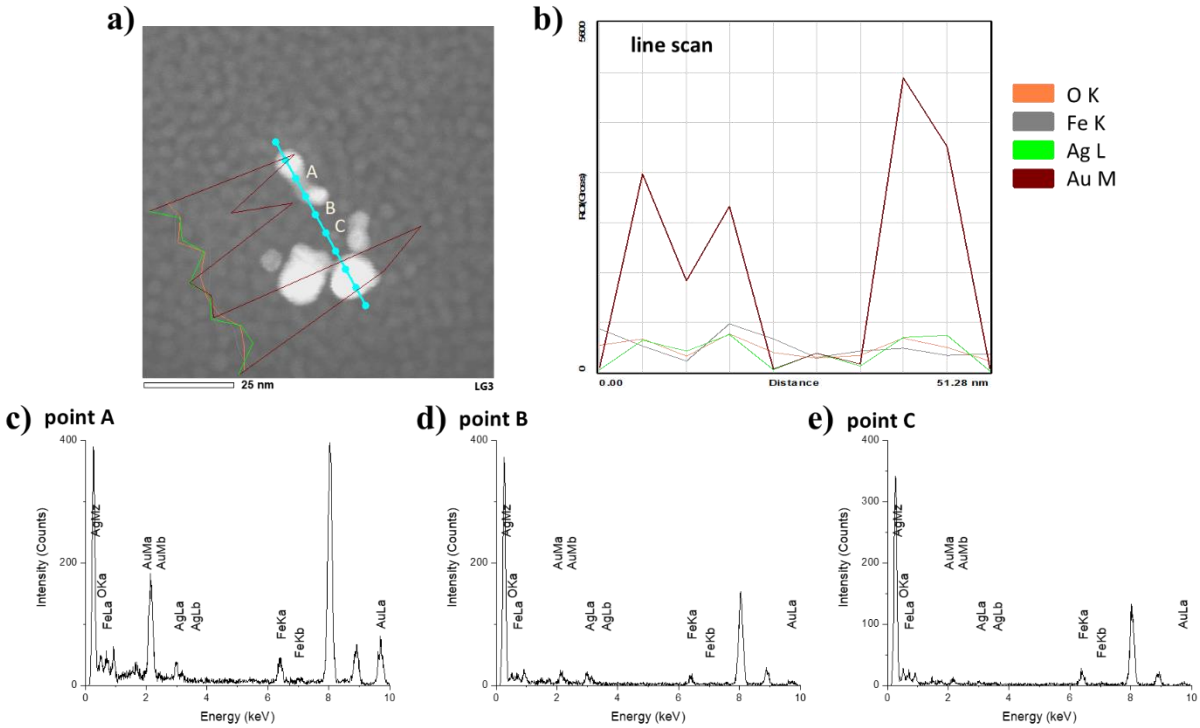

Figure 4.49. a) HRTEM-STEM micrograph of an heterocoagulate dispersion formed at 60 °C from SPIO(Ol)NPs and Au(PEI)NPs, with SPIO(Ol)NPs partially substituted by Ag(Ol)NPs (SPIONs-Ag(Ol)NPs 3:1 ratio); b) element counts along the EDX line-scan; c,d,e) EDX spectra corresponding to the marked points. (Adapted from *ChemNanoMat* 2022, *e202200353*)

HRTEM was used with STEM mode and EDX over heterocoagulate samples containing Au(PEI)NPs and partially substituted SPIO(Ol)NPs by Ag(Ol)NPs, in a 3:1 ratio, respectively (**Figures 4.48, 4.49**). The corresponding EDX spectra over scanning points or areas on the STEM micrographs confirmed the presence of inner Au(PEI)NP compartments. By performing a line scan (**Figure 4.49-a,b**), the vast majority of oleyl-capped nanoparticles in the surrounding matrix were SPIO(Ol)NPs, while the Ag(Ol)NPs are shown to be closely around to the gold domains. Similar assembled nanostructures have been obtained by other approaches, [150,210,211] if then this current strategy affords the incorporation of nanoparticle of contrary solvent dispersibilities and surface functionalization. Thus, these compartmentalized

nanostructures with more than two types of nanoparticles consist of inner, water-dispersible nanoparticle domains inside oil-in-water dispersions, as a new approach to from layer-by-layer encapsulating nanostructures. [134,166]

Magnetic responsiveness and light microscopy of oil-in-water heterocoagulate dispersions

By placing an external neodymium magnet close to an aqueous dispersion of the magnetic heterocoagulate, a concentration of magnetic nanostructures is observed after certain time. Visualization of the dispersions in close proximity to the magnet by light microscopy confirmed the presence of droplets moving towards the direction on the magnet (**Figure 4.50**, external supplementary video). It was remarkable the changeable appearance of these entities when the position of the external magnet was moved, and consequently their orientation towards the magnet. Similar optical effects were also observed on Janus emulsions containing gold nanoparticles. [212] On the other hand, the apparent visualization of these nanostructures in the μm range could be attributed to the largest agglomerates at the sample surface, or to an optically amplifying effect, caused either by reflecting effects of the nanostructures in the oil droplets, by the deposition on a glass slide with a concave cavity or by changes of the refractive index. In any case, the preservation of the magnetic responsiveness of the initial heterocoagulates could be demonstrated. This suggests the possibility of using these systems for magnetic targeting and delivery of encapsulated compounds. [166]

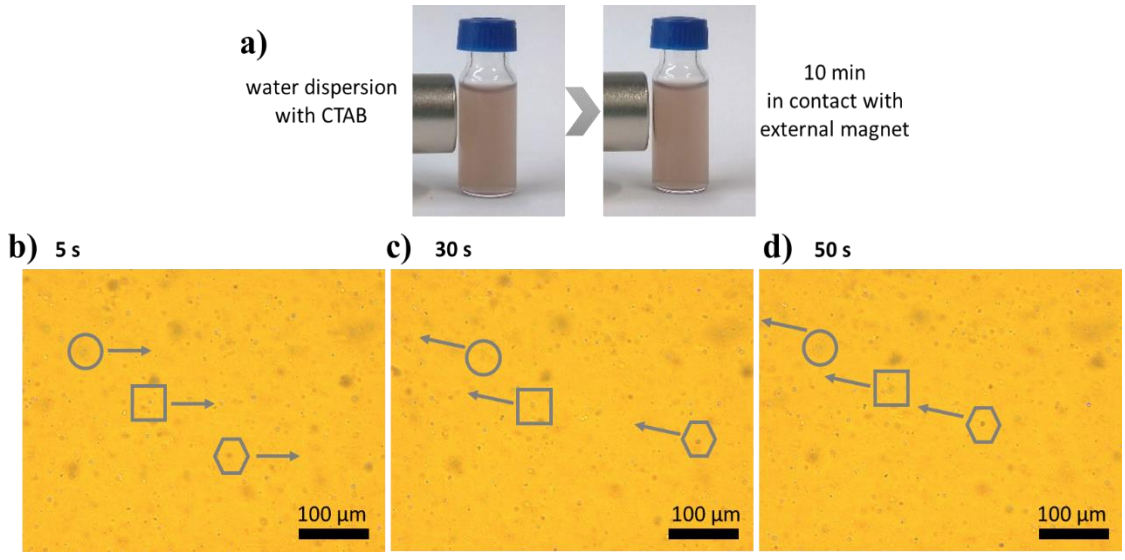

Figure 4.50. a) Photographs of the heterocoagulate dispersions formed at 50 °C from SPIO(Ol)NPs and Au(PEI)NPs and stabilized in water by CTAB, showing the concentration of magnetic particles in the proximity of an external neodymium magnet; b, c, d) light micrographs of the heterocoagulate dispersion showing the movement of droplet-entities towards the magnet at 5, 30 and 50 s of the video, whose position is switched after 25 s. (Adapted from *ChemNanoMat* 2022, *e202200353*)

Conclusions about the magnetic-responsive, compartmentalized nanostructures

In this investigation, it was demonstrated how templated assembly from surfactant dispersions, followed by a step-wise phase-transfer procedures, can incorporate nanoparticles of different composition and solvent dispersibility in hybrid nanostructures (**Scheme 4.4**). The magnetic responsiveness of SPIO(Ol)NPs was necessary to separate the resulting heterocoagulate from the AOT biphasic mixture, with gel formation at higher AOT content.
Interestingly, it was found that only long-chained carboxylic acids can disperse both PEI-stabilized nanoparticles, dispersible in water, as well as oleyl-capped nanoparticles, dispersible in oil solvents. This should be relevant to disperse the resulting heterocoagulate, containing the different types of nanoparticles. Thanks to the protocol of Wu et al. [208], it was possible to transfer the heterocoagulate dispersion from oleic acid to water, assisted by an auxiliary surfactant in water/ethanol mixture (**Scheme 4.5**).

According to the UV-Vis absorption profiles, different trends in the absorption profiles were observed when the heterocoagulates were formed at different temperatures and by partly substituting the SPIO(Ol)NPs by Ag(Ol)NPs (**Figures 4.38, 4.39, 4.40**). Zeta Potential characterization indicated that the auxiliary surfactant should provide electrostatic stabilization at the oil-water interface, having the oleic acid a secondary role (**Figure 4.42**, **Table 4.4**). Cryo-SEM confirmed the formation of oil-in-water droplets in the aqueous dispersion (**Figure 4.43**). Visualization with TEM showed the formation of compartmentalized nanostructures, in which Au(PEI)NP domains were embedded by a matrix/shell of oleyl-capped nanoparticles, being the overall associations as oil-in-water dispersions (**Figures 4.44, 4.45, 4.46**). By initial heating of the AOT dispersion resulting in the magnetic heterocoagulate, the resulting nanostructures were better defined (**Figure 4.44**), if then their soft-character also involved differences for different concentrations, auxiliary surfactants and nanoparticle combinations (**Figures 4.45, 4.46**), in which the number of particles per assembled nanostructure vary significantly. HRTEM and EDX showed that the partial substitution of SPIO(Ol)NPs by Ag(Ol)NPs induces the formation of a silver film around the Au(PEI)NP compartments (**Figures 4.48, 4.49**). The magnetic responsiveness is preserved on the aqueous dispersions (**Figure 4.50**), if then an immediate response is not obvious as that observed from the initial coagulate.

Advantages about these assembled nanostructures include the incorporation of more than two types of nanoparticle components, of very small sizes and of different solvent dispersibilities according to their surface functionalization. Besides the extensive research concerning core-shell nanoparticles, [139,142,148] the presented nanostructures could offer better perspectives of biodistribution and posterior clearance, [213,214] once released the

individual nanoparticles of sizes below 10 nm. The magnetic responsiveness would be also of interest for targeted delivery. Polyethyleneimine-based domains are also promising for the delivery of bioactive substances and genetic material. [215] Additionally, the incorporation of Ag(Ol)NPs would also offer anti-bacterial properties. [107] For this purpose, further research would be needed concerning the use of other auxiliary stabilizing agents, such as biocompatible emulsifiers and stimuli-responsive polymers. [165,209,216] The encapsulating possibilities, as oil-in-water emulsion-like dispersions, are based on the incorporation of water-dispersible nanoparticles in oleic acid and oil- dispersible nanoparticles, dispersed in a continuous water phase. This analogy to layer-by-layer encapsulation [134,166] could also be complementary to other self-organized liquid dispersions like vesicles and microcapsules. [217–219] Other possibilities include separation processes, sensing and bioimaging applications.[150,210,211] Further research is needed to develop these compartmentalized assemblies towards sophisticated, functional nanostructures.

5. Conclusions and perspectives

Different combinations of oil-dispersible and water dispersible nanoparticles could be incorporated in AOT microemulsions. The properties of the microemulsions could be modulated by diverse nanoparticle effects, based on the interactions with the surfactant film. Thus, oleyl-capped nanoparticles would increase the flexibility of the surfactant film and enhance droplet interactions. On the contrary, polylethyleneimine-stabilized nanoparticles would be destabilized by interactions with the AOT head groups, forming controlled agglomerations and hindering droplet interactions by decreasing the flexibility of the AOT film. The combinations of both types of nanoparticles led to a synergistic effect attributed to an increased active surface, resulting in enhanced droplet interactions and smaller droplet sizes.

From biphasic systems at low surfactant content containing oleyl-capped nanoparticles and PEI-stabilized nanoparticles, solvent evaporation of the upper L_2 phase over a surface resulted in nanoparticle assemblies of filament networks. This templated assembly should be based on a controlled nanoparticle clustering and a microemulsion droplet elongation. Some characteristic properties of these arrangements include the formation of transparent films of large extension and certain crystalline ordering, in which a packed matrix is constituted with the remaining AOT. The resulting films can be formed over different surfaces by drop-casting or spin-coating. It is also possible to form similar filament networks with different solvents at different equilibration times, and with different combinations of nanoparticles by keeping equivalent surface functionalization. An optimal time of phase equilibration depends on the solvents in the mixture. Different aqueous contents can also modulate the length of the filaments and the density of cross-points. Some modification methods based on the sintering of nanoparticles were tested by placing the resulting nanostructured films at higher temperatures. Although very high temperatures can destroy the nanoparticle arrangements, the use of Ag(Ol)NPs at moderately high temperature resulted in new morphologies of fused nanostructures, which should result of higher coating stability.

From biphasic systems at higher AOT content with oleyl-capped superparamagnetic nanoparticles and PEI-stabilized nanoparticles, a magnetic-responsive heterocoagulate was formed after phase separation. The initial heating of the dispersion mixture and the sequential phase-transfer procedures of the magnetic heterocoagulate resulted in functional compartmentalized nanostructures in which the magnetic responsiveness is preserved. These oil-in-water assembled nanostructures consisted of Au(PEI)NP domains embedded by a matrix of oil-dispersible nanoparticles, stabilized by an auxiliary surfactant in a continuous water phase. Therefore, layer-by-layer encapsulation and the incorporation of other oleyl-capped nanoparticles of different compositions was possible to arrange in one-entity nanostructure.

Thus, diverse types of assembled nanostructures could be formed by using the same nanoparticle components in quasi-ternary mixtures of AOT colloidal dispersions with oil and water (**Scheme 5.1**). The experimental results of this project were based on fundamental research related to the interfacial assembly of nanoparticles in the well-studied AOT microemulsions. This constitutes a preliminary research which brings out diverse possibilities concerning the templated assembly of nanoparticles in reverse microemulsions. The resulting nanoparticle heterostructures enable the fabrication of assemblies in larger scale, as well as the incorporation of different nanoparticle compositions. A validation of these results would however depend on applied research and the interest of the scientific community at a given period of time. The applicability of these new nanoparticle assemblies should rely on the combination of the individual properties of the nanoparticles and their surface functionalization. Some of the possibilities of optimization and applicability may include other combinations of nanoparticle compositions while keeping equivalent surface functionalization, as well as other solvent combinations for the reverse microemulsions with similar phase properties. Green approaches would also include, for instance, the substitution of PEI coating by chitosan coating, the use of oleic acid as capping ligand discarding oleylamine, and the use of more environmental-friendly solvents, as well as biocompatible surfactants. On one hand, for the surface-assembled filament networks, it would be of interest to obtain transparent, conductive thin films. On the other hand, the aqueous dispersions of magnetic compartmentalized nanostructures could be used in biological systems with biocompatible, stimuli-responsive stabilizers for targeted therapy. To bring forward these findings, further specialised research is required.

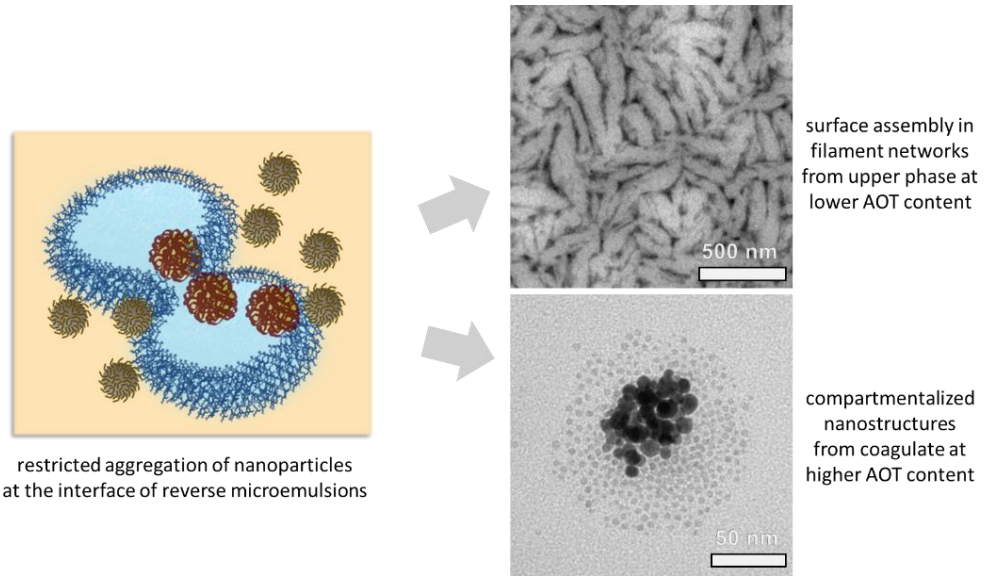

Scheme 5.1. Proposed model about restricted aggregation of nanoparticles in AOT microemulsions that results in the assembly of different hybrid nanostructures.

6. Experimental methods

Materials

All reagents were acquired from commercial sources and used without further purification. Dioctyl sodium sulfosuccinate (AOT), iron (III) acetylacetonate ($Fe(acac)_3$), gold (III) chloride hydrate ($HAuCl_4 \cdot 3H_2O$), hexanoic acid, octanoic acid and oleylamine were obtained from Sigma-Aldrich. Oleic acid was obtained from AppliChem; diphenylether from Alfa Aesar; polyoxyethylene dodecyl ether (Brij 35) and *n*-undecane from Merck; 1,2-hexadecanediol from TCI; *n*-hexane, sodium dodecylsulphate (SDS) and silver nitrate from Roth, and cetyltrimethylammonium bromide (CTAB), *n*-heptane and 1-pentanol from VWR Chemicals. N,N´-dimethylformamide (DMF) and ethanol were solvents used of technical grade. The hyperbranched polyethyleneimine (PEI) with a molar mass of 25,000 g/mol is a commercial product from BASF (Lupasol G100). Water was purified with a Millipore A+ Reference Milli-Q system.

Experimental procedures

The main procedures to describe involve the synthesis and work-up of the used nanoparticles, the formulation of quasi-ternary mixtures in the respective phase diagrams for the investigations of microemulsions, the preparation of thin films of nanoparticle filament networks and the phase transfer of the magnetic heterocoagulate in water to form compartmentalized nanostructures.

Synthesis of SPIO(Ol)NPs

Optimized protocol [182] for microwave-assisted synthesis [113,151]

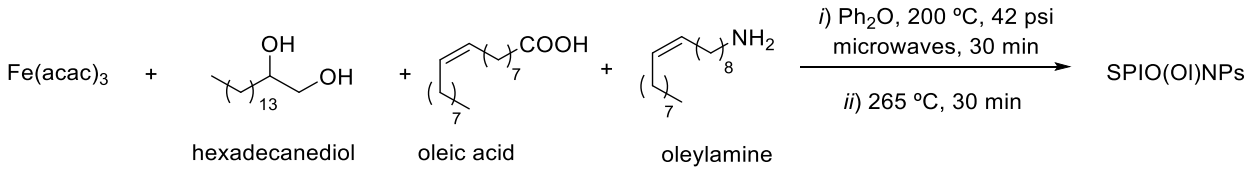

	ρ / ($g \cdot mL^{-1}$)	% purity	MW / ($g \cdot mol^{-1}$)	Eq.	mmol	mass / g	Vol. / mL
$Fe(acac)_3$		97%	353.17	1	0.2	0.0733	
hexadecanediol		98%	258.45	5	1	0.2714	
oleic acid	0.890		282.47	3	0.6		0.2
oleylamine	0.813	70%	267.49	8.5	1.7		0.8
diphenyl ether	1.071		170.21				2 mL

A combined mixture of iron (III) acetyl acetonate (0.0733 g, 0.2 mmol), hexadecanediol (0.2714 g, 1 mmol), oleic acid (0.2 mL, 0.6 mmol) and oleylamine (0.8 mL, 1.7 mmol) in diphenyl ether (2 mL) were heated up to 200 °C inside microwave-assisted Discover SP reactor (CEM) with magnetic stirring at 200 W power during 30 min, and then up to 265 °C for further 30 min. The resulting deep brown dispersion was cooled down to room temperature and precipitated by adding ethanol (5 mL). The supernatant was discarded assisted by magnet, and the solid was redispersed in nonpolar solvent like hexane or heptane (2.5 mL), oleic acid (1.5 mL) and oleylamine (1.5 mL) followed by precipitation-redispersion steps with ethanol (5 mL, then 1.75 mL) and nonpolar solvent (1.5 mL). The final solid was finally dried over vacuum oven at 35 °C for 2 days to afford the SPIO(Ol)NPs (**Figure 6.1**) in about 30 mg as a black solid, which forms dark-brown dispersions in nonpolar solvents.

DLS: 7 ± 1, 289 ± 76 nm; Z-Avg. = 206 nm; PDI = 0.51;
TEM: 4.3 ± 0.5 nm (considering #250 nanoparticle count);
FTIR (**Figure 4.37-b**): $\bar{\upsilon}$ = 3000, 2900 (C-H stretching), 1530 (OC-O$^-$ stretching), 1450 (C-H bending), 1380, 590 (Fe-O) cm^{-1}. [113,206]

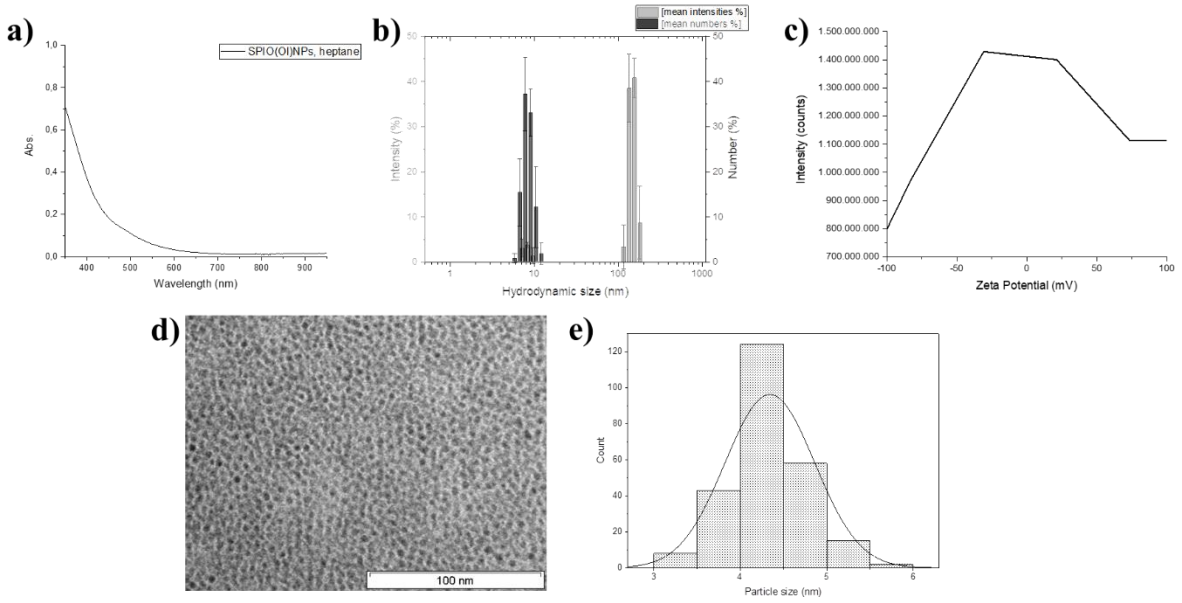

Figure 6.1. Characterization of SPIO(Ol)NPs: a) UV-Vis absorption; b) DLS size distribution; (c) Zeta Potential; d) TEM micrograph, and e) resulting histogram considering #250 nanoparticles.

Synthesis of Au(PEI)NPs

Adapted protocol [157,185] to obtain smaller sizes

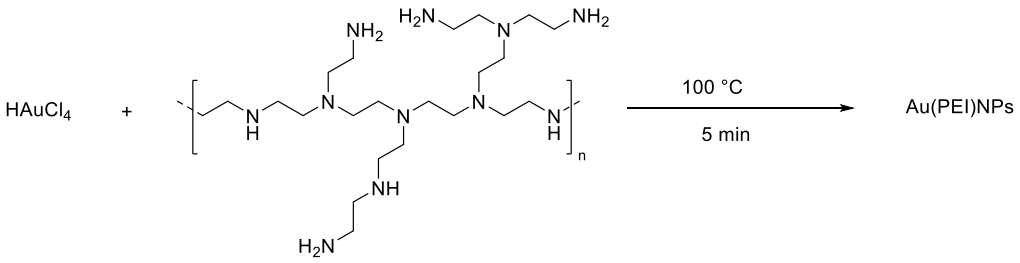

hyperbranched PEI, MW_n=25000 g/mol

	% purity	MW / (g·mol^{-1})	Eq. (Vol. ratio)	Concentration	mass / mg	Vol. / mL
PEI 25000 (aq.)	96.62 dry wt.%	25000	1	2 wt.%	21	1
$HAuCl_4$ (aq.)		339.79	10	2 mM	0.0733	10

An aqueous solution of hyperbranched PEI (2 wt.%), previously prepared with stirring and stabilization overnight, was mixed to an aqueous solution of gold (III) chloride hydrate (2 mM) in a 1:10 Vol. ratio. The mixture was then kept at 100 °C during 5 min and finally cooled down to room temperature to provide a dark red dispersion of Au(PEI)NPs (**Figure 6.2**).

UV-Vis: λ_{max} = 520 (LSPR), 280 nm;
DLS: 27 ± 16, 131± 60, 4552 ± 862 nm; Z-Avg. = 26.5 nm; PDI = 0.37;
ζ-potential: +43 ± 5 mV;
TEM: 4.9 ± 1.5 nm (considering #350 nanoparticle count);
FTIR (**Figure 4.37-b**): $\bar{\upsilon}$ = 3700 (N-H stretching), 3400 (N-H, HO-H stretching), 3050 (NHC-H), 3000, 2900 (C-H stretching), 1660 (N-H bending), 1580, 1450 (C-H bending), 1350 (N-H bending), 1050 (C-N stretching) cm^{-1}. [207]

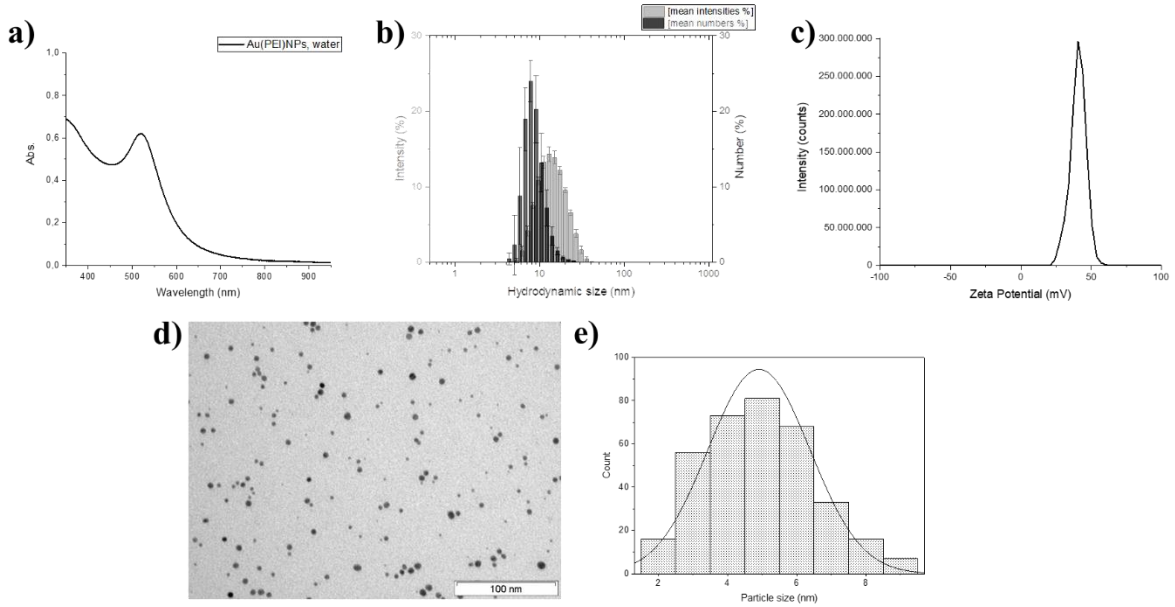

Figure 6.2. Characterization of Au(PEI)NPs: a) UV-Vis absorption; b) DLS size distribution; (c) Zeta Potential; d) TEM micrograph, and e) resulting histogram considering #350 nanoparticles.

Synthesis of Ag(Ol)NPs

Optimized protocol [183,184] with equivalent precursor for microwave-assisted synthesis [114]

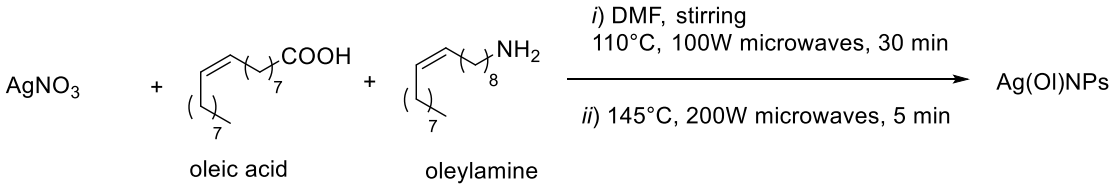

	ρ / (g·mL^{-1})	% purity	MW / (g·mol^{-1})	Eq.	mmol	mass / g	Vol. / mL
$AgNO_3$			169.88	1	0.15	0.0246	
oleic acid	0.890		282.47	8	1.16		0.368
oleylamine	0.813	70%	267.49	8	1.16		0.545
N,N-dimethylformamide							1

Silver nitrate (25 mg, 0.15 mmol) was dissolved in DMF (1 mL) for 25 min at rook tmeperature, before adding an equimolar mixture of oleic acid (0.368 mL, 1.16 mmol) and oleylamine (0.545 mL, 1.16 mmol). The mixture was placed in the microwave-assisted Discover SP reactor (CEM) with stirring, heating up to 110 °C, 100 W power for 30 min, and the resulting clear solution was further set at 147 °C, 200 W power for 5 min. The black mixture was then cooled down to r.t. and flocculated with ethanol (5 mL). After removing the supernatant assisted by centrifugation at approximately 6000 rpm for 15 min, the solid was re-dissolved in heptane

(2 mL), oleic acid (0.5 mL) and oleylamine (0.5 mL) followed by a second precipitation with ethanol (5 mL). Washing and redispersion processes are repeated several times. The final dark solid was finally dried over vacuum oven at 35 °C overnight to afford the Ag(Ol)NPs (**Figure 6.3**) in about 25 mg, which forms dark-yellow dispersions in nonpolar solvents.

UV-Vis: λ_{max} = 423 nm (LSPR);
DLS: 6 ± 2, 42 ± 10 nm; PDI = 0.5;
TEM: 4.5 ± 1.1 nm (considering #300 nanoparticle count);

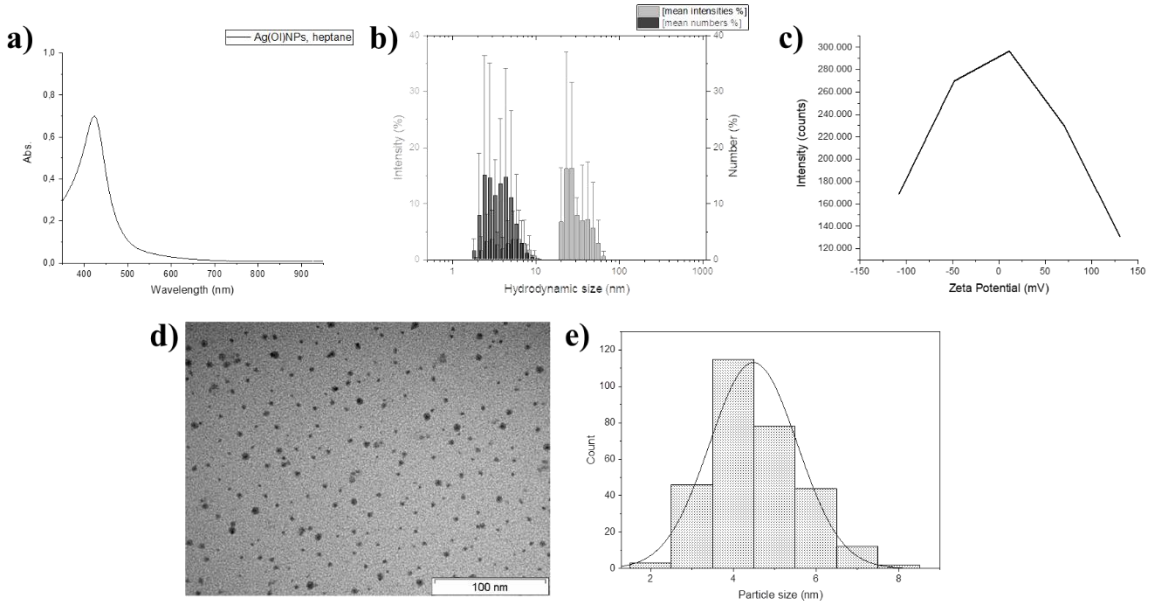

Figure 6.3. Characterization of Ag(Ol)NPs: a) UV-Vis absorption; b) DLS size distribution; (c) Zeta Potential; d) TEM micrograph, and e) resulting histogram considering #300 nanoparticles.

Quasi-Ternary phase diagrams

The extension of the isotropic L_2 phase was determined by visual inspection of titrations consisting on alkane-alcohol/surfactant mixtures in defined oil-to-surfactant mass ratio (ω) with increasing water content. The dry wt.% of AOT was determined by a moisture analyzer MA 30 (Sartorius), so that the inherent water content was considered for the ternary compositions. The oil phase consisted on alkane-alcohol mixtures in defined mass ratio with/without the incorporation of SPIO(Ol)NPs (0.5 wt.% or 1 wt.%) and/or Ag(Ol)NPs (0.5 wt.% alone or in SPIO(Ol)NP-Ag(Ol)NP 1:1, 2:1 or 3:1 ratio). The water phase was also with/without Au(PEI)NPs (0.3 wt.%). All samples were mixed at r.t., using a Vortex vibromixer at 2500 rpm. The phase diagrams are based on mass ratio (*m.r.*) for each component in the quasi-ternary mixture.

Preparation of thin films of heterostructured nanoparticle filament networks from phase-separated AOT microemulsions

Phase separation occurs above the water incorporation capacity of AOT reverse microemulsions at ω = 95:5. After enough equilibration time (usually overnight for heptane-pentanol as oil solvents and several days for hexane-pentanol as oil solvents), the upper L_2 phase is seen optically clear while the excess of water appears as a bottom phase. With the incorporation of Au(PEI)NPs (0.3 wt.% in water) and SPIO(Ol)NPs and/or Ag(Ol)NPs (0.5 total wt.% in oil, SPIO(Ol)NPs/ Ag(Ol)NPs 1:0, 1:1 or 0:1 weight ratio), drop-casting of this microemulsion phase over a given surface and solvent evaporation on a given surface forms a transparent film. Possible surfaces for the coating include glass slides, silicon wafers and electron microscopy grids. Similar thickness is observed by AFM when the nanostructured films were formed either by drop-casting or by spin-coating (400 rpm, 90 s), if then the resulting patterns differ significantly.

Preparation of magnetic layer-by-layer nanoparticle heterostructures from heterocoagulation in AOT dispersions

Phase separation at higher surfactant contents results in the formation of an upper dispersion phase and a lower phase of characteristic viscous gel-like state. When the Au(PEI)NPs (0.3 wt.% in water) and SPIO(Ol)NPs with/without Ag(Ol)NPs (0.5 total wt.% in oil, SPIO(Ol)NPs/ Ag(Ol)NPs 1:0, 4:1 or 3:1 weight ratio) are incorporated in the initial dispersion of about ω = 40:60, a formation of a magnetic-responsive heterocoagulate is observed by phase separation after one day or longer equilibration time (several days ar recommended), at r.t. or with initial heating. This nanoparticle heterocoagulate can be washed with organic solvents, alternating first nonpolar and then polar solvents, assisted by an external neodymium magnet. The remaining solid can be then redispersed in long-chained carboxylic acids solvents (under shaking for several h) to provide after an optically-clear oil dispersion. To transfer the nanostructures in water media, an adapted procedure to disperse hydrophobic nanocrystals in water developed by Wu et al. was applied. [208] This involves the transfer of the oil dispersion to an aqueous solution of an auxiliary surfactant (0.05 M) in ethanol-water of 1:1 to 2:1 Vol. ratio. For CTAB, the optimal Vol. ratio of oleic acid to water-ethanol dispersions was 1:10 to 2:15, for ethanol water 1:1 or 2:1, respectively. The mixture was then washed again by centrifugation, if then a milder sedimentation is also possible by steady conditions overnight. The subsequent redispersion in water provides an optically-clear dispersion of magnetic-responsive nanostructures in water. Additional washing was not used, as it can provide redispersion problems. Initial heating of the nanoparticle dispersions at 50 °C previous to the heterocoagulate formation provided better definer core-shell-like nanostructures of Au(PEI)NP domains embedded by a matrix-shell of oleyl-caped nanoparticles.

Instrumentation for characterization

Characterization methods can be instrumental measurements related to microemulsions properties, visualization by microscopy techniques or other instrumental techniques for elucidating properties and surface functionalization of nanoparticles.

Characterization of microemulsion properties

Conductometric titrations were performed with a LF2000 microprocessor conductometer (WTW) to evaluate percolation phenomena in the isotropic phase at 25 °C. For the LTA 1 and LTG1/23 (WTW) conductance electrode, and alternate current is applied, so that the fluctuations in the voltage are registered and transformed in a digitalized signal by the mediation of a voltammeter. Simultaneously, turbidity was recorded with an ASD12-N (optek-Danulat) light absorption sensor, containing a light source with a wavelength in the NIR, whose measurements of light absorption are digitalized also by the connection with a voltammeter. Temperature can be also controlled at the same time with a Haake B3 thermostat, measured with TFK 530 (WTW) thermopars, based on temperature-dependent resistance. All the electrodes are connected to a computer mediated by respective voltammeters. Titration measurements, automated with a Dosimat 665 (Metrohm), were repeated at least 3 times for each composition to provide average values, and error bars for the conductivity measurements are incorporated.

Differential Scanning Calorimetric (DSC) measurements, to characterize the type of water in the microemulsions, were carried out with a micro DCS 7 evo (Setaram) analyzer at a temperature range between -35 and +80 °C. *N*-undecane was used in the reference vessel. The heating and cooling rates were fixed to 0.3 K/min. After cooling, the sample was kept at -35 °C for 100 min, before starting the heating program. The DSC curves were obtained from the average values of repeated measurements for each composition.

Characterization of nanoparticle and nanostructure properties

UV-Vis absorption and transmittance spectra were recorded with a UV-2600 spectrophotometer (Shimadzu) in the wavelength range between 300 and 1300 nm. For a better visualization of the absorption contribution of only some type of nanoparticles, adequate reference samples should be made, that is, with the same components in the dispersions except for the nanoparticles signal to record. Transmittance curves can be also provided relative to the nanoparticle absorption by removing the substrate signal.

The hydrodynamic sizes in intensity and number plots were determined by dynamic light scattering (DLS), and Zeta potential values were obtained from electrophoretic mobility, being both recorded on a Zetasizer Nano ZS 3600 (Malvern). For the standard operating procedures, the refractive indexes were provided using a DMA 4500 (Anton Paar) refractometer.

Fourier Transform IR spectra of dried samples were recorded at 25 °C on an IR spectrometer Spectrum Two (Perkin Elmer) in the wavenumber range between 4000 and 460 cm^{-1}.

Small-Angle X-ray Scattering (SAXS) was performed in a flow through capillary with a Kratky-type SAXSess instrument (Anton Paar) during 60 min -360 steps of 10 s- at 21 ± 1 °C. The short sample-to-detector distance of 0.309 m is appropriate for investigation of dispersions with low scattering intensities. The measured intensity was converted to absolute scale,[220] with 0.154 nm of radiation wavelength. Samples analyzed with SAXS were used as prepared. The deconvolution of the SAXS curves -slit length desmearing- was performed with the SAXS-Quant software. Curve fitting was conducted with software SASfit for determination of size parameters of the particles. [194]

X-ray Photoelectron Spectroscopy (XPS) was measured on the dried thin films from the respective nanoparticle and microemulsion dispersions over silicon wafers as substrates. To remove the protective film on the substrates, a cleaning procedure under sonication in isopropanol and then water was used, rinsing afterwards with nitrogen. The samples were placed in an exicator at 4 mbar for 24 h. The XPS spectra were recorder with an AXIS Ultra DLD photoelectron spectrometer (Kratos Analytical) using monochromatized aluminum Kα radiation. For avoiding charging effects on the surfaces, an electron flood gun for charge neutralization was used. Survey spectra were recorded with a step size of 1 eV, a pass energy of 80 eV with 3 sweeps and a dwell time of 500 ms, detail-spectra were recorded with a step size of 0.1 eV, a pass energy of 20 eV with 5 or 10 sweeps and a dwell time of 500 ms.

Microscopy techniques

Light microscopy of the final water dispersions was performed on a Leica DMLB microscope equipped with the Leica DFC 295 live camera. For optical light microscopy, the samples can be visualized with an additional polarizing filter. Samples were usually visualized on planar glass slides. For visualization of the nanostructures resulted from the magnetic heterocoagulate, samples were placed on glass slides with circular concave cavity (76 x 26 mm), covered by a micro cover glass (20 × 20 mm).

Scanning electron microscopy (SEM) was performed with a Hitachi S-4800 microscope to visualize nanostructured patterns over a surface after solvent evaporation. Additionally, the

morphology of the liquid-in-liquid dispersions was investigated by cryo-scanning electron microscopy (cryo-SEM), of cross-sections from freeze-dried samples. For this, the samples (without solvent evaporation) were immersed into nitrogen slush at atmospheric pressure, freeze-fractured at -180 °C, etched for 60 s at -98 °C, and sputtered with platinum in the GATAN Alto 2500 cryo preparation chamber, then transferred into the SEM microscope.

Size and shape of the resulting nanostructures were determined by transmission electron microscopy (TEM), recorded with a JEM-1011 (JEOL) microscope at an acceleration voltage of 80 kV. For a more-detailed characterization, HRTEM images and EDX spectra were recorded with a JEM-2200 FS (JEOL) microscope at an acceleration voltage of 200 kV.

To measure the thickness of the nanostructured films, Atomic force microscopy (AFM) was performed using a MultiMode 8 (Bruker) microscope in the air using tapping mode.

Research data processing

The characterization data were generally taken using the software provided by default for each commercial instrument: UV-Vis spectra with Shimadzu-UV-Probe; DLS and Zeta Potential with ZetaSizer-software; micro-DSC with Setaram-Calisto, as Data-Acquisition and Processing modes; light microscopy with Leica-LAS-V4.1.0; electron micrographs with additional analysis and related characterization with Olympus-iTEM; AFM Data with Gwyddion®. Raw experimental data was usually processed using Microsoft Office and text documents. The resulting data was mainly plotted using Origin®.

7. References

[1] J. Koetz, S. Kosmella, *Polyelectrolytes and Nanoparticles*, Springer Berlin Heidelberg, Berlin, Heidelberg, **2007**.
[2] T. F. Tadros, *Applied Surfactants*, Wiley, **2005**.
[3] T. F. Tadros, *Interfacial Phenomena and Colloid Stability*, DE GRUYTER, **2015**.
[4] S. K. Ghosh, T. Pal, *Chem. Rev.* **2007**, *107*, 4797.
[5] S. J. Amina, B. Guo, *Int. J. Nanomedicine* **2020**, *15*, 9823.
[6] I. Danielsson, B. Lindman, *Colloids and Surfaces* **1981**, *3*, 391.
[7] T. P. Hoar, J. H. Schulman, *Nature* **1943**, *152*, 102.
[8] M. Gradzielski, M. Duvail, P. M. de Molina, M. Simon, Y. Talmon, T. Zemb, *Chem. Rev.* **2021**, *121*, 5671.
[9] D. J. McClements, *Soft Matter* **2012**, *8*, 1719.
[10] A. M. Bago Rodriguez, B. P. Binks, T. Sekine, *Langmuir* **2019**, *35*, 6693.
[11] Y. Yang, Z. Fang, X. Chen, W. Zhang, Y. Xie, Y. Chen, Z. Liu, W. Yuan, *Front. Pharmacol.* **2017**, *8*, DOI 10.3389/fphar.2017.00287.
[12] Y. Chevalier, M.-A. Bolzinger, *Colloids Surfaces A Physicochem. Eng. Asp.* **2013**, *439*, 23.
[13] K. Larson-Smith, D. C. Pozzo, *Langmuir* **2012**, *28*, 11725.
[14] B. P. Binks, *Curr. Opin. Colloid Interface Sci.* **2002**, *7*, 21.
[15] A. D. Dinsmore, M. F. Hsu, M. G. Nikolaides, M. Marquez, A. R. Bausch, D. A. Weitz, *Science (80-.).* **2002**, *298*, 1006.
[16] R. Zana, *Dynamics of Surfactant Self-Assemblies*, CRC Press, Boca Raton, **2005**.
[17] Y. Chevalier, T. Zemb, *Reports Prog. Phys.* **1990**, *53*, 279.
[18] N. Dib, C. M. O. Lépori, N. M. Correa, J. J. Silber, R. D. Falcone, L. García Río, *Polymers (Basel).* **2021**, *13*, 1378.
[19] B. K. Paul, S. P. Moulik, *J. Dispers. Sci. Technol.* **1997**, *18*, 301.
[20] D. J. Mitchell, B. W. Ninham, *J. Chem. Soc. Faraday Trans. 2* **1981**, *77*, 601.
[21] J. Sjöblom, R. Lindberg, S. E. Friberg, *Adv. Colloid Interface Sci.* **1996**, *65*, 125.
[22] W. C. Griffin, *J. Soc. Cosmet. Chem.* **1949**, *1*, 311.
[23] J.-L. Salager, R. Antón, J. Bullón, A. Forgiarini, R. Marquez, *Cosmetics* **2020**, *7*, 57.
[24] C. Stubenrauch, *Microemulsions: Background, New Concepts, Applications, Perspectives*, John Wiley & Sons, Ltd, Chichester, UK, **2009**.
[25] L. E. Scriven, *Nature* **1976**, *263*, 123.
[26] P. MacCarthy, *J. Chem. Educ.* **1983**, *60*, 922.
[27] T. K. De, A. Maitra, *Adv. Colloid Interface Sci.* **1995**, *59*, 95.
[28] J. Eastoe, B. H. Robinson, D. C. Steytler, D. Thorn-Leeson, *Adv. Colloid Interface Sci.* **1991**, *36*, 1.
[29] N. M. Correa, J. J. Silber, R. E. Riter, N. E. Levinger, *Chem. Rev.* **2012**, *112*, 4569.
[30] C. Mathew, P. K. Patanjali, A. Nabi, A. Maitra, *Colloids and Surfaces* **1988**, *30*, 253.
[31] A. M. Howe, C. Toprakcioglu, J. C. Dore, B. H. Robinson, *J. Chem. Soc. Faraday Trans. 1 Phys. Chem. Condens. Phases* **1986**, *82*, 2411.
[32] J. Eastoe, B. H. Robinson, D. C. Steytler, *J. Chem. Soc. Faraday Trans.* **1990**, *86*, 511.
[33] E. Acosta, E. Szekeres, D. A. Sabatini, J. H. Harwell, *Langmuir* **2003**, *19*, 186.
[34] M. J. Hou, D. O. Shah, *Langmuir* **1987**, *3*, 1086.
[35] H.-F. Eicke, W. Meier, H. Hammerich, *Langmuir* **1994**, *10*, 2223.
[36] S. Ray, S. R. Bisal, S. P. Moulik, *J. Chem. Soc., Faraday Trans.* **1993**, *89*, 3277.

[37] S. P. Moulik, K. Mukherjee, *Proceedings-indian Natl. Sci. Acad. A* **1996**, *62 A*, 215.
[38] P. A. Winsor, *Trans. Faraday Soc.* **1948**, *44*, 376.
[39] R. Zana, in *Dyn. Surfactant Self-Assemblies* (Ed.: R. Zana), CRC Press, **2005**, pp. 1–35.
[40] C. La Mesa, L. Coppola, G. A. Ranieri, M. Terenzi, G. Chidichimo, *Langmuir* **1992**, *8*, 2616.
[41] E. . Franses, T. . Hart, *J. Colloid Interface Sci.* **1983**, *94*, 1.
[42] S. G. Frank, G. Zografi, *J. Colloid Interface Sci.* **1969**, *29*, 27.
[43] S. Bisal, P. K. Bhattacharya, S. P. Moulik, *J. Phys. Chem.* **1990**, *94*, 350.
[44] K. Kon-No, A. Kitahara, *J. Colloid Interface Sci.* **1971**, *37*, 469.
[45] B. Tamamushi, N. Watanabe, *Colloid Polym. Sci.* **1980**, *258*, 174.
[46] P. Ekwall, L. Mandell, K. Fontell, *J. Colloid Interface Sci.* **1970**, *33*, 215.
[47] J. Lang, A. Jada, A. Malliaris, *J. Phys. Chem.* **1988**, *92*, 1946.
[48] M. Moha-Ouchane, J. Peyrelasse, C. Boned, *Phys. Rev. A* **1987**, *35*, 3027.
[49] J. Eastoe, B. H. Robinson, R. K. Heenan, *Langmuir* **1993**, *9*, 2820.
[50] J. Eastoe, G. Fragneto, B. H. Robinson, T. F. Towey, R. K. Heenan, F. J. Leng, *J. Chem. Soc. Faraday Trans.* **1992**, *88*, 461.
[51] P. L. Luisi, M. Giomini, M. P. Pileni, B. H. Robinson, *Biochim. Biophys. Acta - Rev. Biomembr.* **1988**, *947*, 209.
[52] C. M. Dunn, B. H. Robinson, F. J. Leng, *Spectrochim. Acta Part A Mol. Spectrosc.* **1990**, *46*, 1017.
[53] J. Eastoe, W. K. Young, B. H. Robinson, D. C. Steytler, *J. Chem. Soc. Faraday Trans.* **1990**, *86*, 2883.
[54] M. . Hou, M. Kim, D. O. Shah, *J. Colloid Interface Sci.* **1988**, *123*, 398.
[55] C. Boned, J. Peyrelasse, M. Moha-Ouchane, *J. Phys. Chem.* **1986**, *90*, 634.
[56] B. K. Paul, S. P. Moulik, Eds. , *Ionic Liquid-Based Surfactant Science*, John Wiley & Sons, Inc, Hoboken, NJ, **2015**.
[57] V. G. Rao, C. Banerjee, S. Ghosh, S. Mandal, J. Kuchlyan, N. Sarkar, *J. Phys. Chem. B* **2013**, *117*, 7472.
[58] V. G. Rao, S. Ghosh, C. Ghatak, S. Mandal, U. Brahmachari, N. Sarkar, *J. Phys. Chem. B* **2012**, *116*, 2850.
[59] C. M. O. Lépori, N. M. Correa, J. J. Silber, R. D. Falcone, M. López-López, M. L. Moyá, *Langmuir* **2020**, *36*, 10785.
[60] S. Ray, S. P. Moulik, *Langmuir* **1994**, *10*, 2511.
[61] L. García Río, J. R. Leis, J. C. Mejuto, M. E. Pena, E. Iglesias, *Langmuir* **1994**, *10*, 1676.
[62] S. Kosmella, J. Koetz, *Curr. Opin. Colloid Interface Sci.* **2012**, *17*, 261.
[63] A. H. Poghosyan, L. H. Arsenyan, A. A. Shahinyan, J. Koetz, *Colloids Surfaces A Physicochem. Eng. Asp.* **2016**, *506*, 402.
[64] A. H. Poghosyan, L. H. Arsenyan, L. A. Antonyan, A. A. Shahinyan, J. Koetz, *Colloids Surfaces A Physicochem. Eng. Asp.* **2015**, *479*, 18.
[65] A. H. Poghosyan, A. A. Shahinyan, J. Koetz, *Colloids Surfaces A Physicochem. Eng. Asp.* **2018**, *546*, 20.
[66] T. Beitz, J. Kötz, S. E. Friber, in *Prog. Colloid Polym. Sci. Struct. Dyn. Prop. Disperse Colloid. Syst.*, Steinkopff Verlag, Darmstadt, **1998**, pp. 100–106.
[67] M. Fechner, J. Koetz, *Langmuir* **2011**, *27*, 5316.
[68] O. Rojas, J. Koetz, S. Kosmella, B. Tiersch, P. Wacker, M. Kramer, *J. Colloid Interface Sci.* **2009**, *333*, 782.
[69] C. Note, J. Ruffin, B. Tiersch, J. Koetz, *J. Dispers. Sci. Technol.* **2007**, *28*, 155.
[70] C. Note, J. Koetz, L. Wattebled, A. Laschewsky, *J. Colloid Interface Sci.* **2007**, *308*, 162.
[71] C. Note, J. Koetz, S. Kosmella, *Colloids Surfaces A Physicochem. Eng. Asp.* **2006**, *288*,

158.
[72] C. Note, J. Koetz, S. Kosmella, *J. Colloid Interface Sci.* **2006**, *302*, 662.
[73] J. Koetz, C. Günther, S. Kosmella, E. Kleinpeter, G. Wolf, in *Prog. Colloid Polym. Sci. Aqueous Polym. — Cosolute Syst.*, Springer Berlin Heidelberg, Berlin, Heidelberg, **2003**, pp. 27–36.
[74] R. D. Bhalke, P. N. Kulkarni, P. N. Kendre, V. V. Pande, M. A. Giri, *Futur. J. Pharm. Sci.* **2020**, *6*, DOI https://doi.org/10.1186/s43094-020-00075-5.
[75] E. Mitsou, E. P. Kalogianni, D. Georgiou, H. Stamatis, A. Xenakis, M. Zoumpanioti, *Langmuir* **2019**, *35*, 150.
[76] T. Shukla, N. Upmanyu, M. Agrawal, S. Saraf, S. Saraf, A. Alexander, *Biomed. Pharmacother.* **2018**, *108*, 1477.
[77] M. D. Chatzidaki, E. Mateos-Diaz, F. Leal-Calderon, A. Xenakis, F. Carrière, *Food Funct.* **2016**, *7*, 2258.
[78] A. K. Sharma, T. Garg, A. K. Goyal, G. Rath, *Artif. Cells, Nanomedicine, Biotechnol.* **2016**, *44*, 1177.
[79] R. Stehle, C. Schulreich, S. Wellert, J. Gäb, M.-M. Blum, K. Kehe, A. Richardt, A. Lapp, T. Hellweg, *J. Colloid Interface Sci.* **2014**, *413*, 127.
[80] E. Mitsou, G. Tavantzis, G. Sotiroudis, D. Ladikos, A. Xenakis, V. Papadimitriou, *Colloids Surfaces A Physicochem. Eng. Asp.* **2016**, *510*, 69.
[81] N. Dib, V. R. Girardi, J. J. Silber, N. M. Correa, R. D. Falcone, *Org. Biomol. Chem.* **2021**, *19*, 4969.
[82] A. Küchler, M. Yoshimoto, S. Luginbühl, F. Mavelli, P. Walde, *Nat. Nanotechnol.* **2016**, *11*, 409.
[83] A. Xenakis, in *Recent Trends Surf. Colloid Sci.*, World Scientific, **2012**, pp. 199–206.
[84] S. Vargas-Ruiz, C. Schulreich, A. Kostevic, B. Tiersch, J. Koetz, S. Kakorin, R. von Klitzing, M. Jung, T. Hellweg, S. Wellert, *J. Colloid Interface Sci.* **2016**, *471*, 118.
[85] R. Kanwar, J. Rathee, M. Tanaji Patil, S. Kumar Mehta, in *Microemulsion - a Chem. Nanoreactor* (Ed.: J.C. Mejuto), IntechOpen, **2018**, pp. 41–57.
[86] A. K. Ganguli, A. Ganguly, S. Vaidya, *Chem. Soc. Rev.* **2010**, *39*, 474.
[87] R. P. Bagwe, K. C. Khilar, *Langmuir* **1997**, *13*, 6432.
[88] M. P. Pileni, *J. Phys. Chem.* **1993**, *97*, 6961.
[89] V. V. Mody, A. Singh, B. Wesley, *Eur. J. Nanomedicine* **2013**, *5*, 11.
[90] J. M. D. Coey, *Magnetism and Magnetic Materials*, Cambridge University Press, Cambridge, **2010**.
[91] N. A. Frey, S. Peng, K. Cheng, S. Sun, *Chem. Soc. Rev.* **2009**, *38*, 2532.
[92] M. Arruebo, R. Fernández-Pacheco, M. R. Ibarra, J. Santamaría, *Nano Today* **2007**, *2*, 22.
[93] L. Wu, A. Mendoza-Garcia, Q. Li, S. Sun, *Chem. Rev.* **2016**, *116*, 10473.
[94] U. Jeong, X. Teng, Y. Wang, H. Yang, Y. Xia, *Adv. Mater.* **2007**, *19*, 33.
[95] Wahajuddin, S. Arora, *Int. J. Nanomedicine* **2012**, *7*, 3445.
[96] L. Blaney, *Lehig Univ. Preserv.* **2007**, *15*, 33.
[97] W. Wu, Q. He, C. Jiang, *Nanoscale Res. Lett.* **2008**, *3*, 397.
[98] N. Zhu, H. Ji, P. Yu, J. Niu, M. Farooq, M. Akram, I. Udego, H. Li, X. Niu, *Nanomaterials* **2018**, *8*, 810.
[99] M.-A. Neouze, U. Schubert, *Monatshefte für Chemie - Chem. Mon.* **2008**, *139*, 183.
[100] S. Bedanta, A. Barman, W. Kleemann, O. Petracic, T. Seki, *J. Nanomater.* **2013**, *2013*, 169.
[101] A. Moores, F. Goettmann, *New J. Chem.* **2006**, *30*, 1121.
[102] M.-C. Daniel, D. Astruc, *Chem. Rev.* **2004**, *104*, 293.

[103] L. M. Liz-Marzán, *Mater. Today* **2004**, *7*, 26.
[104] K. L. Kelly, E. Coronado, L. L. Zhao, G. C. Schatz, *J. Phys. Chem. B* **2003**, *107*, 668.
[105] S. K. Ghosh, S. Nath, S. Kundu, K. Esumi, T. Pal, *J. Phys. Chem. B* **2004**, *108*, 13963.
[106] K. Nejati, M. Dadashpour, T. Gharibi, H. Mellatyar, A. Akbarzadeh, *J. Clust. Sci.* **2022**, *33*, 1.
[107] B. Le Ouay, F. Stellacci, *Nano Today* **2015**, *10*, 339.
[108] S. Horikoshi, N. Serpone, *Microwaves in Nanoparticle Synthesis*, Wiley, **2013**.
[109] N. T. K. Thanh, N. Maclean, S. Mahiddine, *Chem. Rev.* **2014**, *114*, 7610.
[110] V. K. LaMer, R. H. Dinegar, *J. Am. Chem. Soc.* **1950**, *72*, 4847.
[111] M. Baghbanzadeh, L. Carbone, P. D. Cozzoli, C. O. Kappe, *Angew. Chemie Int. Ed.* **2011**, *50*, 11312.
[112] H. Duan, D. Wang, Y. Li, *Chem. Soc. Rev.* **2015**, *44*, 5778.
[113] T. A. Lastovina, A. P. Budnyk, M. A. Soldatov, Y. V. Rusalev, A. A. Guda, A. S. Bogdan, A. V. Soldatov, *Mendeleev Commun.* **2017**, *27*, 487.
[114] V. Abdelsayed, A. Aljarash, M. S. El-Shall, Z. A. Al Othman, A. H. Alghamdi, *Chem. Mater.* **2009**, *21*, 2825.
[115] E. V. Shevchenko, D. V. Talapin, N. A. Kotov, S. O'Brien, C. B. Murray, *Nature* **2006**, *439*, 55.
[116] M. S. Lee, D. W. Yee, M. Ye, R. J. Macfarlane, *J. Am. Chem. Soc.* **2022**, *144*, 3330.
[117] A.-C. Genix, J. Oberdisse, *Soft Matter* **2018**, *14*, 5161.
[118] K. J. Si, Y. Chen, Q. Shi, W. Cheng, *Adv. Sci.* **2018**, *5*, 1700179.
[119] M. A. Boles, M. Engel, D. V. Talapin, *Chem. Rev.* **2016**, *116*, 11220.
[120] D. Luo, C. Yan, T. Wang, *Small* **2015**, *11*, 5984.
[121] J. Gong, G. Li, Z. Tang, *Nano Today* **2012**, *7*, 564.
[122] M. Grzelczak, J. Vermant, E. M. Furst, L. M. Liz-Marzán, *ACS Nano* **2010**, *4*, 3591.
[123] O. D. Velev, *Science (80-.).* **2006**, *312*, 376.
[124] L. Xu, W. Ma, L. Wang, C. Xu, H. Kuang, N. A. Kotov, *Chem. Soc. Rev.* **2013**, *42*, 3114.
[125] Z. Xue, C. Yan, T. Wang, *Adv. Funct. Mater.* **2019**, *29*, 1807658.
[126] Y. A. Diaz Fernandez, T. A. Gschneidtner, C. Wadell, L. H. Fornander, S. Lara Avila, C. Langhammer, F. Westerlund, K. Moth-Poulsen, *Nanoscale* **2014**, *6*, 14605.
[127] Z. Nie, A. Petukhova, E. Kumacheva, *Nat. Nanotechnol.* **2010**, *5*, 15.
[128] D. V. Talapin, J.-S. Lee, M. V. Kovalenko, E. V. Shevchenko, *Chem. Rev.* **2010**, *110*, 389.
[129] A. Böker, J. He, T. Emrick, T. P. Russell, *Soft Matter* **2007**, *3*, 1231.
[130] A. S. Siller-Martínez, K. M. Fuentes, E. T. Adesuji, F. Aceves, V. O. Torres-Guerrero, E. Guardado-Villegas, K. Basilio-Bernabé, M. Ceballos, M. Navarro-Segura, R. D. Rivera-Rangel, J. A. Arizpe-Zapata, M. Videa, M. Sánchez-Domínguez, *Front. Mater.* **2022**, *9*, 910081.
[131] H. Gu, Z. Yang, J. Gao, C. K. Chang, B. Xu, *J. Am. Chem. Soc.* **2005**, *127*, 34.
[132] S. P. Pujari, L. Scheres, A. T. M. Marcelis, H. Zuilhof, *Angew. Chemie Int. Ed.* **2014**, *53*, 6322.
[133] W. Wei, F. Bai, H. Fan, *iScience* **2019**, *11*, 272.
[134] S. K. Ghosh, A. Böker, *Macromol. Chem. Phys.* **2019**, *220*, 1900196.
[135] E. N. Golubina, N. F. Kizim, *Russ. J. Phys. Chem. A* **2021**, *95*, 659.
[136] A. Toor, T. Feng, T. P. Russell, *Eur. Phys. J. E* **2016**, *39*, 57.
[137] A. Fahmi, T. Pietsch, C. Mendoza, N. Cheval, *Mater. Today* **2009**, *12*, 44.
[138] S. Shi, T. P. Russell, *Adv. Mater.* **2018**, *30*, 1800714.
[139] G. R. Elmi, K. Saleem, M. M. F. A. Baig, M. N. Aamir, M. Wang, X. Gao, M. Abbas, M. U. Rehman, *Magnetochemistry* **2022**, *8*, 38.

[140] B. Liu, H. Zhang, Y. Ding, *Chinese Chem. Lett.* **2018**, *29*, 1725.
[141] J. Canet-Ferrer, P. Albella, A. Ribera, J. V. Usagre, S. A. Maier, *Nanoscale Horizons* **2017**, *2*, 205.
[142] S. Sabale, P. Kandesar, V. Jadhav, R. Komorek, R. K. Motkuri, X.-Y. Yu, *Biomater. Sci.* **2017**, *5*, 2212.
[143] N. C. Bigall, W. J. Parak, D. Dorfs, *Nano Today* **2012**, *7*, 282.
[144] L. Xu, M. Sun, W. Ma, H. Kuang, C. Xu, *Mater. Today* **2016**, *19*, 595.
[145] K. D. Gilroy, A. Ruditskiy, H.-C. Peng, D. Qin, Y. Xia, *Chem. Rev.* **2016**, *116*, 10414.
[146] R. Ghosh Chaudhuri, S. Paria, *Chem. Rev.* **2012**, *112*, 2373.
[147] S. V. Salihov, Y. A. Ivanenkov, S. P. Krechetov, M. S. Veselov, N. V. Sviridenkova, A. G. Savchenko, N. L. Klyachko, Y. I. Golovin, N. V. Chufarova, E. K. Beloglazkina, A. G. Majouga, *J. Magn. Magn. Mater.* **2015**, *394*, 173.
[148] L. Zhou, J. Yuan, Y. Wei, *J. Mater. Chem.* **2011**, *21*, 2823.
[149] C. Wu, Z. Lu, Z. Li, Y. Yin, *Small Struct.* **2021**, *2*, 2100005.
[150] L. Hao, Y. Leng, L. Zeng, X. Chen, J. Chen, H. Duan, X. Huang, Y. Xiong, X. Chen, *Adv. Sci.* **2020**, *7*, 1902433.
[151] S. Kosmella, B. Klemke, I. Häusler, J. Koetz, *Colloids Surfaces A Physicochem. Eng. Asp.* **2019**, *570*, 331.
[152] Z. Yang, T. Altantzis, D. Zanaga, S. Bals, G. Van Tendeloo, M. P. Pileni, *J. Am. Chem. Soc.* **2016**, *138*, 3493.
[153] J. A. Gutierrez, J. J. Silber, R. D. Falcone, N. M. Correa, *J. Mol. Liq.* **2021**, *331*, 115709.
[154] S. Vaidya, A. K. Ganguli, in *Compr. Nanosci. Nanotechnol.*, Elsevier, **2019**, pp. 1–12.
[155] M. P. Pileni, *Nat. Mater.* **2003**, *2*, 145.
[156] K. Lemke, C. Prietzel, J. Koetz, *J. Colloid Interface Sci.* **2013**, *394*, 141.
[157] C. Note, S. Kosmella, J. Koetz, *Colloids Surfaces A Physicochem. Eng. Asp.* **2006**, *290*, 150.
[158] K. Lemke, J. Koetz, *J. Nanomater.* **2012**, *2012*, 478153.
[159] J. Baier, J. Koetz, S. Kosmella, B. Tiersch, H. Rehage, *J. Phys. Chem. B* **2007**, *111*, 8612.
[160] J. Koetz, J. Baier, S. Kosmella, *Colloid Polym. Sci.* **2007**, *285*, 1719.
[161] J. Koetz, C. Note, J. Baier, S. Lutter, in *Recent Trends Surf. Colloid Sci.*, World Scientific, **2012**, pp. 243–255.
[162] J. Koetz, S. Reichelt, S. Kosmella, B. Tiersch, *J. Colloid Interface Sci.* **2005**, *284*, 190.
[163] Y. Lin, A. Böker, H. Skaff, D. Cookson, A. D. Dinsmore, T. Emrick, T. P. Russell, *Langmuir* **2005**, *21*, 191.
[164] Y. Lin, *Science (80-.).* **2003**, *299*, 226.
[165] X. Zhang, T. Liang, Q. Ma, *Drug Deliv.* **2021**, *28*, 655.
[166] H. Ai, *Adv. Drug Deliv. Rev.* **2011**, *63*, 772.
[167] E. T. Adesuji, V. O. Torres-Guerrero, J. A. Arizpe-Zapata, M. Videa, M. Sánchez-Domínguez, K. M. Fuentes, *Nanotechnology* **2020**, *31*, 425601.
[168] I. Miccoli, F. Edler, H. Pfnür, C. Tegenkamp, *J. Phys. Condens. Matter* **2015**, *27*, 223201.
[169] G. W. H. Höhne, W. F. Hemminger, H.-J. Flammersheim, *Differential Scanning Calorimetry*, Springer Berlin Heidelberg, Berlin, Heidelberg, **2003**.
[170] H. Hauser, G. Haering, A. Pande, P. L. Luisi, *J. Phys. Chem.* **1989**, *93*, 7869.
[171] J. Thomas, T. Gemming, *Analytical Transmission Electron Microscopy*, Springer, Dordrecht, **2014**.
[172] D. B. Williams, C. B. Carter, *Transmission Electron Microscopy*, Springer US, Boston, MA, **1996**.
[173] J. I. Goldstein, D. E. Newbury, J. R. Michael, N. W. M. Ritchie, J. H. J. Scott, D. C. Joy,

Scanning Electron Microscopy and X-Ray Microanalysis, Springer, New York, **2018**.
[174] Y. Talmon, *J. Mol. Liq.* **2015**, *210*, 2.
[175] D. Johnson, D. L. Oatley-Radcliffe, N. Hilal, in *Membr. Charact.*, Elsevier, **2017**, pp. 115–144.
[176] N. A. Geisse, *Mater. Today* **2009**, *12*, 40.
[177] I. W. Hamley, *Small-Angle Scattering: Theory, Instrumentation, Data, and Applications*, Wiley, **2021**.
[178] T. Li, A. J. Senesi, B. Lee, *Chem. Rev.* **2016**, *116*, 11128.
[179] J. M. Hollander, W. L. Jolly, *Acc. Chem. Res.* **1970**, *3*, 193.
[180] D. Wilson, M. A. Langell, *Appl. Surf. Sci.* **2014**, *303*, 6.
[181] S. Mourdikoudis, L. M. Liz-Marzán, *Chem. Mater.* **2013**, *25*, 1465.
[182] S. Sun, H. Zeng, *J. Am. Chem. Soc.* **2002**, *124*, 8204.
[183] T. Yamamoto, Y. Wada, T. Sakata, H. Mori, M. Goto, S. Hibino, S. Yanagida, *Chem. Lett.* **2004**, *33*, 158.
[184] I. Pastoriza-Santos, L. M. Liz-Marzán, *Adv. Funct. Mater.* **2009**, *19*, 679.
[185] F. Liebig, R. M. Sarhan, C. Prietzel, A. F. Thünemann, M. Bargheer, J. Koetz, *Langmuir* **2018**, *34*, 4584.
[186] M. Guettari, A. E. L. Aferni, T. Tajouri, *J. Mol. Struct.* **2017**, *1149*, 712.
[187] S. K. Mehta, S. Sharma, *J. Colloid Interface Sci.* **2006**, *296*, 690.
[188] R. Tanaka, T. Yokoyama, K. Sameshima, T. Kawase, *Bull. Chem. Soc. Jpn.* **2005**, *78*, 599.
[189] F. Goffredi, V. Turco Liveri, G. Vassallo, *J. Colloid Interface Sci.* **1992**, *151*, 396.
[190] V. R. Girardi, J. J. Silber, N. Mariano Correa, R. Darío Falcone, *Colloids Surfaces A Physicochem. Eng. Asp.* **2014**, *457*, 354.
[191] M. T. Lombardo, L. D. Pozzo, *Langmuir* **2015**, *31*, 1344.
[192] V. S. Raghuwanshi, M. Ochmann, A. Hoell, F. Polzer, K. Rademann, *Langmuir* **2014**, *30*, 6038.
[193] T. Ung, L. M. Liz-Marzán, P. Mulvaney, *J. Phys. Chem. B* **2001**, *105*, 3441.
[194] I. Breßler, J. Kohlbrecher, A. F. Thünemann, *J. Appl. Crystallogr.* **2015**, *48*, 1587.
[195] D. Saha, D. Ray, J. Kohlbrecher, V. K. Aswal, AIP Publishing, **2019**, p. 030033.
[196] D. Saha, D. Ray, J. Kohlbrecher, V. K. Aswal, *ACS Omega* **2018**, *3*, 8260.
[197] L. Giehm, C. L. P. Oliveira, G. Christiansen, J. S. Pedersen, D. E. Otzen, *J. Mol. Biol.* **2010**, *401*, 115.
[198] J. Koetz, J. Bahnemann, G. Lucas, B. Tiersch, S. Kosmella, *Colloids Surfaces A Physicochem. Eng. Asp.* **2004**, *250*, 423.
[199] J. D. Hopwood, S. Mann, *Chem. Mater.* **1997**, *9*, 1819.
[200] R. E. Ridley, E. Alvarado, A. A. Mrse, V. R. Vasquez, O. A. Graeve, *Langmuir* **2020**, *36*, 11274.
[201] E. Rodríguez-León, R. Íñiguez-Palomares, E. Urrutia-Bañuelos, R. Herrera-Urbina, J. Tánori, A. Maldonado, *Nanoscale Res. Lett.* **2015**, *10*, 101.
[202] S. K. Sainis, V. Germain, C. O. Mejean, E. R. Dufresne, *Langmuir* **2008**, *24*, 1160.
[203] S. W. Winslow, J. W. Swan, W. A. Tisdale, *J. Am. Chem. Soc.* **2020**, *142*, 9675.
[204] E. Bergendal, P. Gutfreund, G. A. Pilkington, R. A. Campbell, P. Müller-Buschbaum, S. A. Holt, M. W. Rutland, *Nanoscale* **2021**, *13*, 371.
[205] B. Domènech, A. Plunkett, M. Kampferbeck, M. Blankenburg, B. Bor, D. Giuntini, T. Krekeler, M. Wagstaffe, H. Noei, A. Stierle, M. Ritter, M. Müller, T. Vossmeyer, H. Weller, G. A. Schneider, *Langmuir* **2019**, *35*, 13893.
[206] K. Yang, H. Peng, Y. Wen, N. Li, *Appl. Surf. Sci.* **2010**, *256*, 3093.
[207] T. J. Cho, J. M. Gorham, J. M. Pettibone, J. Liu, J. Tan, V. A. Hackley, *Langmuir* **2020**, *36*,

14058.
[208] L. Wu, J. Yu, L. Chen, D. Yang, S. Zhang, L. Han, M. Ban, L. He, Y. Xu, Q. Zhang, *J. Mater. Chem. C* **2017**, *5*, 3065.
[209] R. R. Raju, F. Liebig, A. Hess, H. Schlaad, J. Koetz, *RSC Adv.* **2019**, *9*, 19271.
[210] E. M. Rodrigues, N. D. Calvert, J. C. Crawford, N. Liu, A. J. Shuhendler, E. Hemmer, *Small* **2022**, *18*, 2107130.
[211] M. Lach, C. Strelow, A. Meyer, A. Mews, T. Beck, *ACS Appl. Mater. Interfaces* **2022**, *14*, 10656.
[212] R. R. Raju, J. Koetz, *Langmuir* **2022**, *38*, 147.
[213] C. Lopez-Chaves, J. Soto-Alvaredo, M. Montes-Bayon, J. Bettmer, J. Llopis, C. Sanchez-Gonzalez, *Nanomedicine Nanotechnology, Biol. Med.* **2018**, *14*, 1.
[214] J. Liu, M. Yu, C. Zhou, J. Zheng, *Mater. Today* **2013**, *16*, 477.
[215] A. Zakeri, M. A. J. Kouhbanani, N. Beheshtkhoo, V. Beigi, S. M. Mousavi, S. A. R. Hashemi, A. Karimi Zade, A. M. Amani, A. Savardashtaki, E. Mirzaei, S. Jahandideh, A. Movahedpour, *Nano Rev. Exp.* **2018**, *9*, 1488497.
[216] U. Doering, D. Grigoriev, K. Tapio, I. Bald, A. Böker, *Soft Matter* **2022**, *18*, 2558.
[217] C. Neumann, L. Bacher, A. Musyanovych, M. Tutus, A. Latnikova, *Chem. – A Eur. J.* **2021**, *27*, 9336.
[218] E. Gumieniczek-Chłopek, J. Odrobińska, T. Strączek, A. Radziszewska, S. Zapotoczny, C. Kapusta, *Materials (Basel).* **2020**, *13*, 1219.
[219] A. Tomitaka, H. Arami, Z. Huang, A. Raymond, E. Rodriguez, Y. Cai, M. Febo, Y. Takemura, M. Nair, *Nanoscale* **2018**, *10*, 184.
[220] D. Orthaber, A. Bergmann, O. Glatter, *J. Appl. Crystallogr.* **2000**, *33*, 218.

8. List of abbreviations and symbols

Abs. absorption intensity (of absorbed light by a medium)

AFM Atomic Force Microscopy

Ag(Ol)NP oleyl-capped silver nanoparticle

AOT Aerosol-OT, bis-(2-ethyl-hexyl) sodium sulfosuccinate

aq. aqueous, water-like

Au(PEI)NP polyethyleinimine-stabilized gold nanoparticle

a_0 area of the head-group of a surfactant

Brij 35 polyoxyethylene (23) lauryl ether

cpp critical packing parameter

CTAB cetyltrimethylammonium bromide

C_i concentration of particles of a certain "*i*" component

C_{max} maximum concentration of precursor monomer during nucleation

C_{min} minimum concentration of precursor monomer to start nucleation

C_{sat} saturation concentration of precursor monomer, not reduced during growth step

DLS Dynamic Light Scattering

DSC Differential Scanning Calorimetry

D distance between two adjacent particles

$d_{surfaces}$ distance between the surfaces of two adjacent, dispersed colloids

d_0 critical size for supressed magnetization, with no magnetic domain

d_c critical size of maximum magnetization, to form magnetic multi-domains

d_h hydrodynamic diameter

EDX Energy-Dispersive X-ray (spectroscopy)

Eq. equivalents

FTIR Fourier-Transform Infra-Red (spectroscopy)

G_i Gibbs free energy (of *i*-contribution)

h Planck constant

HLB hydrophilic-lipophilic balance

HRTEM High-Resolution Transmission Electron Microscopy

H_0 spontaneous curvature of the surfactant film

H_c applied magnetic field for coercivity or supressed magnetization

H_s applied magnetic field for reaching saturation magnetization

IR infrared (electromagnetic radiation)

$I(q)$ small-angle scattering intensity

$I_{cluster}(q)$ small-angle scattering intensity of particle clusters

$I_G(q)$ small-angle scattering intensity according to Guinier model

$I_p(q)$ small-angle scattering intensity of non-interacting particles

I_0 forward X-ray scattering intensity at $q = 0$

LSPR localized surface plasmon resonance

l_c chain length of the tail of a surfactant

L_1 oil-in-water, optically-clear dispersion

L_2 water-in-oil, optically-clear dispersion

m.r. mass ratio for a given component

MW molecular weight

m_i mass content or proportion for a given *i* component

M_r remnant magnetization

M_s saturation magnetization

NIR near-infrared (electromagnetic radiation)

n number of particles as random flight steps in a cluster

N_i number concentration of particles of "*i*" component

org. organic, oil-like

o/w oil-in-water droplet dispersion

PDI polydispersity index

PEI polyethyleneimine

$P(q)$ form factor as contribution of the small-angle scattering intensity

q scattering angle vector

r.t. room temperature

R radius of a spherical particle

R_G radius of gyration of a particle (assuming to be spherical)

r_h hydrodynamic radius

R_{median} median value of the radius of a spherical particle

R_0 spontaneous radius of the surfactant self-organized associate

SAXS Small-Angle X-ray Scattering

SDS sodium dodecyl sulphate

SEM Scanning Electron Microscopy

SPIO(Ol)NP oleyl-capped superparamagnetic iron oxide nanoparticle

STEM Scanning-Transmission Electron Microscopy

S(q) structure factor as contribution of the small-angle scattering intensity

TEM Transmission Electron Microscopy

T% transmittance percentage

T_c crystallization temperature

T_m melting temperature

UV-Vis ultraviolet-visible light (spectroscopy)

Vol. volume

V_0 volume of hydrophobic part of a surfactant

V_i volume content or proportion for a given *i* component

WPII Winsor type II phase-separated dispersion

wt.% weight percent content

w/o water-in-oil droplet dispersion

XPS X-ray Photoelectron Spectroscopy

Z.-Avg. zeta average

ΔH_c crystallization enthalpy

ΔH_m melting enthalpy

ζ Zeta Potential

λ wavelength

ρ resistivity

υ wave frequency

$\bar{\upsilon}$ wavenumber

Φ volume fraction of the dispersed phase in a microemulsion

Ω ohms (resistance)

ω oil-to-surfactant mass ratio

2D two-dimensional

3D three-dimensional

* Appendix / Anhang

List of publications / Publikationsliste

- R. Fortes Martín, C. Prietzel, J. Koetz, Templated Assembly of Gold-Magnetite Nanoparticles at the water/oil Interface of Microemulsions, *J. Coll Int. Sci.* **2021**, *581*, 44-55.
- R. Fortes Martín, A. F. Thünemann, J. M Sctockmann, J. Radnik, J. Koetz, From Nanoparticle Heteroclusters to Filament Networks by Self-Assembly at the Water-Oil Interface of Reverse Microemulsions, *Langmuir* **2021**, *37*, 8876-8885.
- R. Fortes Martín, C. Prietzel, J. Koetz, Nanostructured assembly of magnetic and plasmonic nanoparticles transferred from AOT Winsor phases to oil-in-water functional dispersions, *ChemNanoMat* **2022**, e202200353 (*in press*).
- R. Fortes Martín, J. Koetz, (…) Reverse microemulsions with green solvents, (*in preparation*).
- R. Fortes Martín, J. Koetz, (…) Proving versatility about the surface templated-assembly of nanoparticles from reverse microemulsions to filament networks (*in preparation*).

Contributions in attended Conferences / Konferenzbeiträge

❖ Oral presentations / Vorträge

- R. Fortes Martín, J. Koetz: "Water-in-Oil Microemulsions as Soft-Templates for the Self-Assembly of Nanoparticle Clusters into Filament Networks"; 25. GDCh JungChemikerForum Frühjahrssymposium, Hannover, 03-2022.
- R. Fortes Martín, J. Koetz: "Reverse Microemulsions as versatile Soft-Templates for the Surface Assembly of Nanoparticles into Heterostructured Filament Networks"; ECIS 18th European Student Colloid Conference, Szeged (Hungary), 06-2022.
- R. Fortes Martín, J. Koetz: "Water-in-oil microemulsions as soft-templates for the interfacial assembly of nanoparticles"; 9th Iberian Meeting on Colloids and Interfaces, Santiago de Compostela (Spain), 07-2022.

❖ Poster exhibitions / Poster Ausstellungen

- R. Fortes Martín, J. Koetz: "Potential Self-Assembly of Nanoparticles at the Interface of Microemulsions"; 15th Zsigmondy Colloquium, Dresden, 08-2019.
- R. Fortes Martín, J. Koetz: "Templated Assembly of Gold-Magnetite Nanoparticles at the water/oil Interface of Microemulsions"; 16th Zsigmondy Colloquium, Düsseldorf, 03-2020.
- R. Fortes Martín, J. Koetz: "Reverse microemulsions as a soft-template for nanoparticles assembly"; 51st Conference of the German Colloid Society, Berlin, 09-2022.

Declaration of independence / Eidesstattliche Erklärung

This doctoral Thesis entitled “Water-in-oil microemulsions as soft-templates to mediate nanoparticle interfacial assembly into hybrid nanostructures” is based on the research work conducted between September 2018 and December 2022, under the supervision of Prof. Joachim Koetz as Group Leader of the Colloid Chemistry Group, in the Institute of Chemistry of the University of Potsdam.

I hereby declare that the submitted work was carried out independently, without external help, and all the related sources are properly mentioned and acknowledged with specified references. I also confirm that I did not submit this work to any other University or Institution before.

/

Diese Dissertation „Water-in-oil microemulsions as soft-templates to mediate nanoparticle interfacial assembly into hybrid nanostructures“ basiert auf den Forschungsergebnissen von September 2018 bis Dezember 2022, unter der Betreuung von Prof. Joachim Koetz als Gruppenleiter der Arbeitsgruppe Kolloidchemie, am Institut für Chemie an der Universität Potsdam.

Hiermit erkläre ich, dass ich die vorliegende Arbeit selbstständig und ohne fremde Hilfe angefertigt habe. Ich habe ausschließlich die angegebenen Quellen und Hilfsmittel verwendet. Weiterhin versichere ich, dass ich diese Arbeit nicht an einer anderen Universität oder Institution vorgelegt habe.

Rebeca Fortes Martín

Potsdam-Golm Date/Datum: Signature/Unterschrift: